Validation of an Advanced Shrinkage Porosity Model
for Steel Casting

Richard A. Hardin, Robert Donahue and Christoph Beckermann

Department of Mechanical Engineering

The University of Iowa, Iowa City, 52242

Abstract

The prevention of solidification shrinkage porosity forming during steel casting is one of the foundry industry's most challenging production issues. Here a novel simulation model for predicting shrinkage porosity in steel castings is calibrated and validated using a series of castings experiments. Two sets of casting experiments were designed to produce varying levels of shrinkage piping and centerline, surface, and hot spot shrinkage porosity. In the first set of experiments, straight cylinders, tapered cylinders, and rectangular hot spot blocks were cast. In the second set of experiments, a tree of spherical hot spot castings, an inverted V-shaped castings and two blind riser castings were poured with the riser feeding a cylinder at its mid-height in one case and at its base in the other. Thermocouple data was recorded for each set of experiments. Inverse modeling was performed for each set of temperature data to determine the temperature-dependent thermophysical property data and boundary conditions giving the best agreement between the temperature measurements and predictions. The observed porosity distributions in the experiments were compared to modeling predictions using a currently available commercial porosity model and the novel porosity model. The optimum set of adjustable parameters in the novel porosity model were determined that achieves the best agreement between observed and predicted porosity locations and distributions. The final comparisons between observed and predicted porosity distributions are presented.

1. Introduction

Steel castings are under-utilized due to uncertainties in their performance and lack of expertise in casting mechanical design. Discontinuities in castings, like porosity, play an important role in casting underutilization due to its uncertain and detrimental effects on the structural and fatigue performance of steel castings. The effects of porosity on steel casting stiffness, strength, and fatigue performance have been reviewed [1,2]. If porosity were to be accurately predicted from casting simulation, robust casting rigging and processes can be developed to prevent porosity from forming in the part, or at critical locations in parts. Then as an end goal, if both the local prediction of porosity in casting simulation and the effects of porosity on the part performance were to be realistically modeled, engineers could develop robust casting processes, and designs that are tolerant of the porosity and reliable. If such a framework were to exist, non-destructive evaluation (NDE) requirements could be intelligently specified to assure component performance and reliability.

Porosity forms during steel casting if additional liquid is not provided to compensate for the volumetric contraction occurring during solidification. Foundry engineers design the casting process to provide this additional feed metal during solidification to avoid this shrinkage porosity from forming. This is done by designing castings to solidify directionally, and by providing additional volumes of metal to feed this solidification shrinkage. The volumes providing liquid to the casting, or feeders, must remain sufficiently liquid until after the casting solidifies.

The volumetric contraction driving the porosity formation during solidification is reflected by both the liquid and solid phase densities increasing as the casting cools as shown by the black solid curve in Figure 1for a 1022 steel. In the figure the red-dashed liquid and blue-dashed solid density curves are shown extrapolated into the solidification temperature range. In addition to temperature, the density of the solidifying mixture of liquid and solid steel is also proportionally dependent on
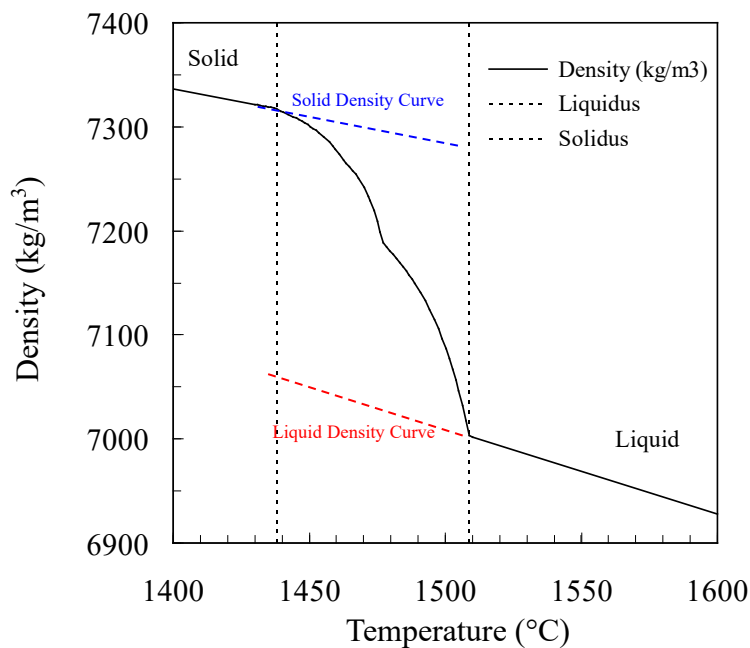

Figure 1. Temperature dependent density curve for a 1022 steel (a) with the pure liquid and solid density curves shown in red and blue dashed lines, respectively. Solidification curve for the same steel.

the amount of liquid and solid present at a given temperature. This is shown by the black density curve in Figure 1 between the liquidus and solidus temperatures. Using the fraction of solid to describe the amount of solid and liquid present at a given temperature, the temperature-solid fraction curve for the steel (as shown in Figure 2) is also needed to determine the density changes and shrinkage behavior of the steel during solidification. The temperature-solid fraction curve (also called solidification curve) in Figure 2 has a kink at around 1477 °C due to a phase transformation. This has a corresponding effect on the density of the solidifying steel density in Figure 1 where the kink at 1477 °C is also seen. To accurately model the shrinkage porosity behavior of a steel, the solidification behavior of the steel must be well understood. Solidification curves will be
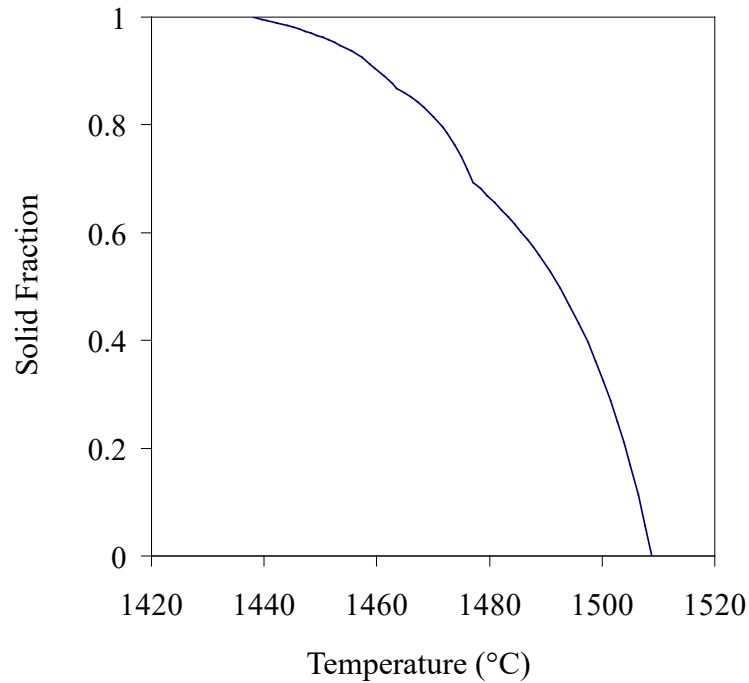
Figure 2. Temperature-solid fraction curve, or solidification curve, needed to know the density curve in Figure 1for the 1022 steel.

determined for the experiments performed in this study to model the porosity formation as accurately as possible.

The advanced shrinkage porosity model applied in this study [3,4] predicts porosity forming from several mechanisms when the feeding flow is cut off. Surface sink porosity shown in Figure 3(a) tends to form on the outside surface of long freezing range castings. For short freezing range castings, the porosity tends to form internally either as larger macroporosity shown in Figure 3(b) or as the microporosity shown Figure 3(c). The model's capabilities to predict these types of porosity are explored in this study by comparing its results to casting experiments designed to
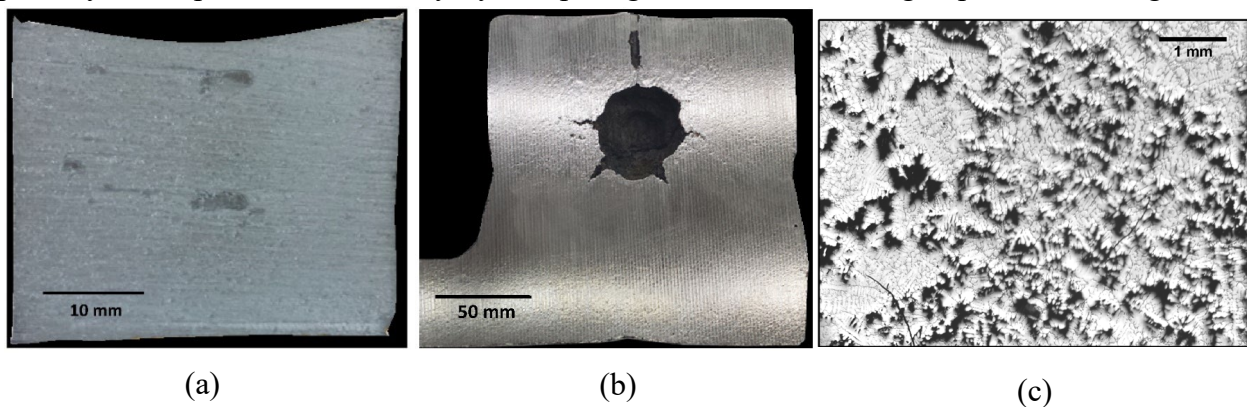

| (a) | (b) | (c) |

Figure 3. Surface sink and porosity defects caused by shrinkage from [3]: (a) external surface sink porosity, and internal macroporosity (b) and microporosity (c).

3

generate the types of porosity shown in Figure 3.

Two heats of porosity experiments were poured in this effort. The experiments were designed to produce varying levels of shrinkage piping and centerline, surface, and hot spot shrinkage porosity. In the first heat of experiments, straight cylinders, tapered cylinders, and rectangular hot spot blocks were cast. In the second heat, a tree of spherical hot spot castings, an inverted V-shaped castings and two blind riser castings were poured with the riser feeding a cylinder at its mid-height in one case and at its base in the other. Thermocouple data was recorded for each set of experiments. Inverse modeling was performed for each set of temperature data to determine the temperature-dependent thermophysical property data and boundary conditions giving the best agreement between the temperature measurements and predictions. Solidification curves for the steel from each heat were determined, as shown for example in Figure 2. Observed porosity distributions in the experiments were compared to modeling predictions from the advanced porosity model and a standard model used commercial software. Recommended parameters in the advanced porosity model were determined that achieves the best agreement between observed and predicted porosity locations and distributions as shown in the results below.

2. Procedures and Methods

2.1 Casting Experiment Procedures

The steel poured in both heats of this study was ASTM A216 Grade WCB steel. It is a cast carbon steel having a combination of good ductility and strength. Its chemical composition is (maximum wt%): C 0.3; Mn 1.0; P 0.035; S 0.035; Si 0.6; Cu 0.3; Ni 0.5; Cr 0.5; Mo 0.2; V 0.03; and the total of Cu, Ni, Cr, Mo, and V cannot exceed 1.0 wt%. At room temperature Grade WCB steel has a yield strength of 248 MPa, 485 MPa tensile strength and 22% elongation as minimum tensile requirements in ASTM A216. This steel was selected as it is a commonly cast steel in the foundry industry with a feeding behavior like many carbon steels.

Seven castings were poured in the first heat of casting experiments: five of which were cylindrical castings, and two were rectangular-shaped hot spot block castings. The five cylindrical castings consisted of three straight cylinders 3.0"in diameter by 20" high. These are cases A1, A2 and A3 as shown in Figure 4. The other two cylindrical casting were tapered, cases B and C as seen in Figure 4. Case B was inversely tapered from a 2.5" diameter top to a 3.5" diameter base. Case C was tapered to provide directional feeding from a 3.5" diameter top to a 2.5" diameter base. The tapered cases were designed to create different porosity profiles with case C having a short shrinkage pipe, and B having the longest shrinkage piping of all the cylindrical cases. As seen in Figure 5, the top of the mold had an overflow, or flow off, cut out of it. This would allow the mold pourer to fill each experiment to the same height, allowing for a slight over filling of each experiment. Also shown in Figure 5, is the opening/port in the mold used to position a thermocouple in case A3. The two hot spot castings poured in the first heat are shown in Figure 6(a), cases D1 and D2. These castings were designed such that there would be no liquid feed metal available to the 2.0" x 2.0" x 4.0" hot spot blocks shortly after filling. As a result, internal macroporosity as seen in Figure 3(b) should form in the center of the block cross section. As shown
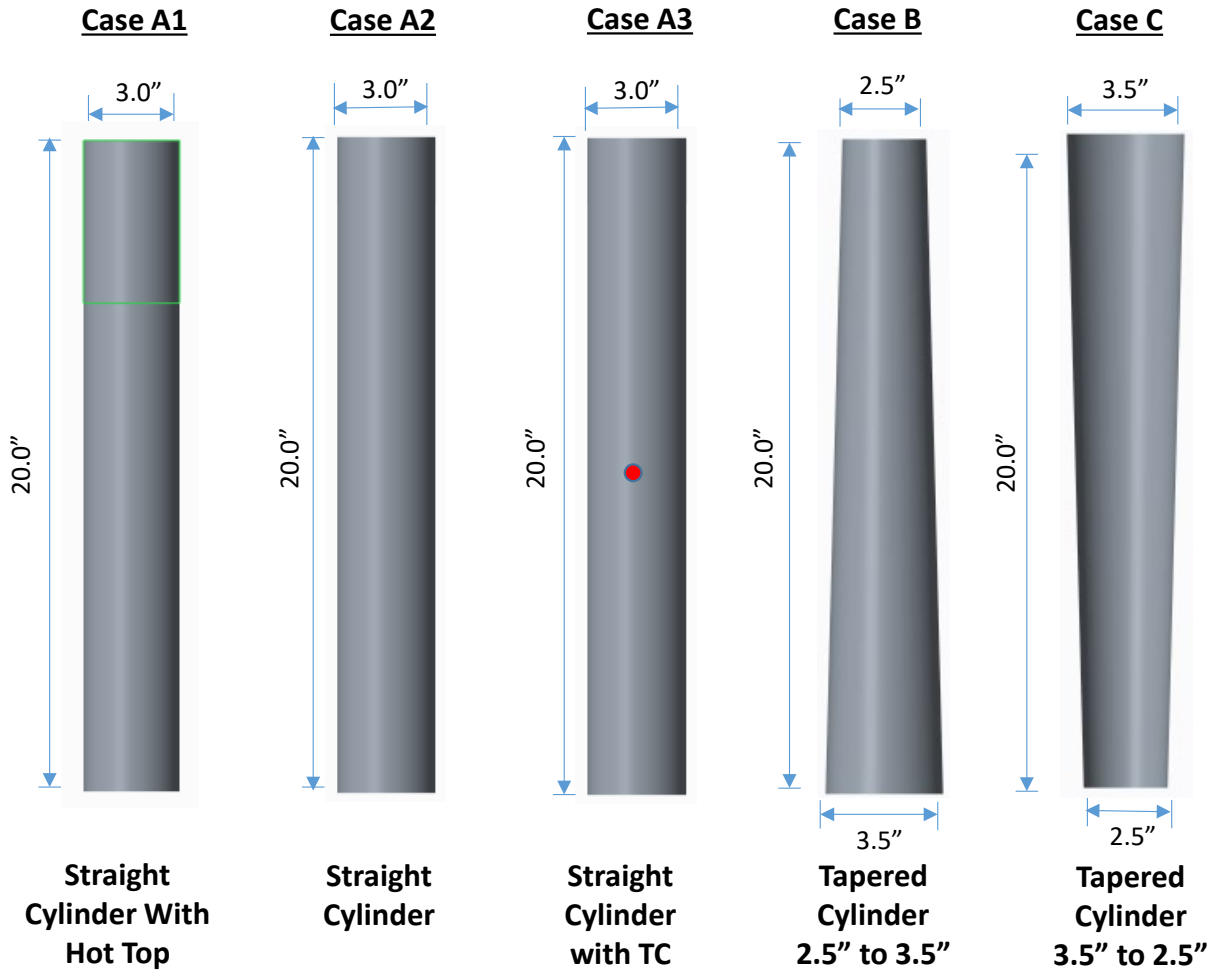
Case A1	Case A2	Case A3	Case B	Case C
3.0"	3.0"	3.0"	2.5"	3.5"
20.0"	20.0"	20.0"	20.0"	20.0"
			3.5"	2.5"
Straight Cylinder With Hot Top	**Straight Cylinder**	**Straight Cylinder with TC**	**Tapered Cylinder 2.5" to 3.5"**	**Tapered Cylinder 3.5" to 2.5"**

Figure 4. Images of the five cylinder-shaped casting experiments performed to generate varying levels and distributions of centerline shrinkage prosity to compare and calibrate the the prorosity model.

in Figure 6(b), a flow off was used in the hot spot castings. Two thermocouples were placed in the hot spot casting case D2.

Temperature measurements from thermocouples placed in cylinder casting A3 and hot spot casting D2 were recorded during solidification for the first heat. The data was used for follow-on work to confirm the accuracy of casting simulations by demonstrating agreement between measured and simulated temperature data. For the temperature measurements in each heat of experiments Type B thermocouple (TC) sensors (70%Pt/30%Rh–94%Pt/6%Rh, by weight) were constructed from wire, ceramic insulators, and quartz tubes for measuring temperatures in steel alloys. The B type TC bead was micro welded before the sensor was assembled using high temperature adhesive. The casting molds were printed with portals/channels for the sensors to be inserted so the TCs could be positioned as accurately as possible. The temperature data measured during cooling was approximately 1530 °C to room temperature. In the Results section of this paper, the measured temperatures are analyzed and plotted to determine temperature versus time
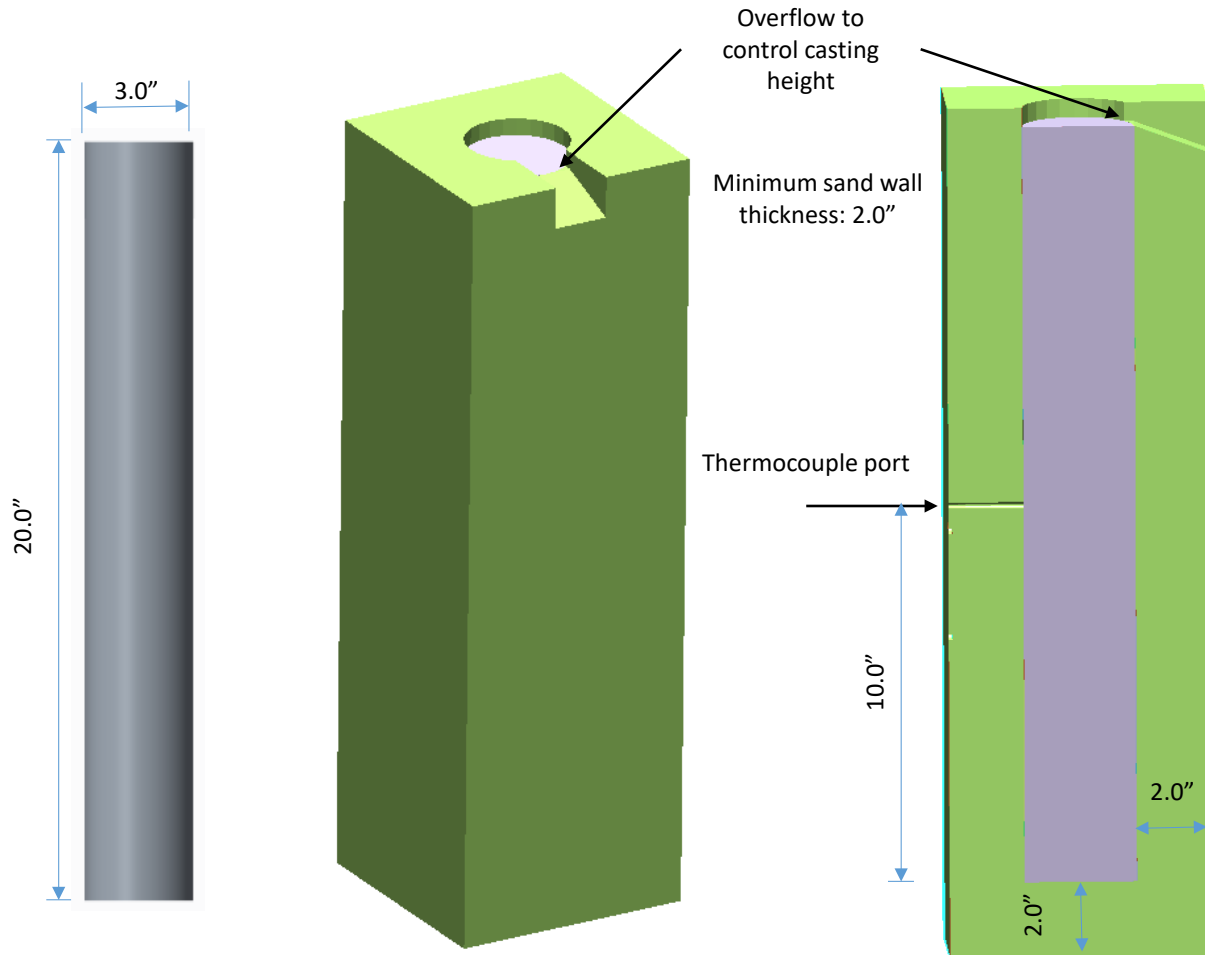
Figure 5. From left to right, cylinder casting poured in porosity experiments at UNI, view of the exterior of the mold used in the experiments showing flow off/overflow, and section of the mold and casting poured in porosity experiments.

cooling history data and cooling rate-temperature plots to determine keys events during solidification such as liquidus and solidus temperatures.

Following the casting experiments and cooling, all castings in heat 1 were cut 3.0 mm off center and machined on one side to the centerline. This section is shown for the cylinder experiments in the far-right image in Figure 5. For the hot spot experiments the section was cut at 3 mm off the mid-width of the blocks along the casting length. The surface of the thicker half was machined was polished and inspected using a red dye penetrant. Images were made of the porosity distributions on the cut, machined and dyed section surfaces. These images will be compared to the simulated porosity distributions in the Results section of this paper.

The second heat of porosity experiments was poured using different casting geometries. The methods used for the thermocouple measurements, and sectioning of the castings to observe the porosity and make images of the results were the same as used in the first heat. Six porosity experiments were poured in the second heat. Four porosity experiment cases that generate porosity through various geometric features of the castings were designed as shown in Figure 7. Two of the
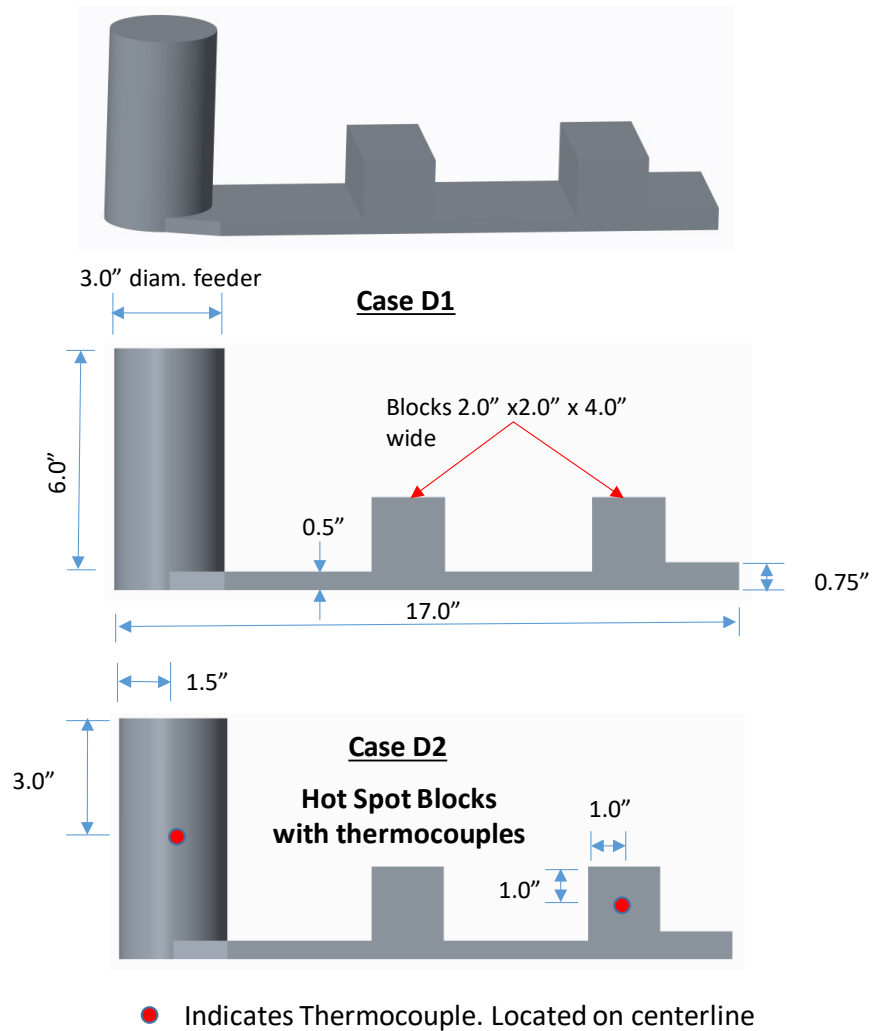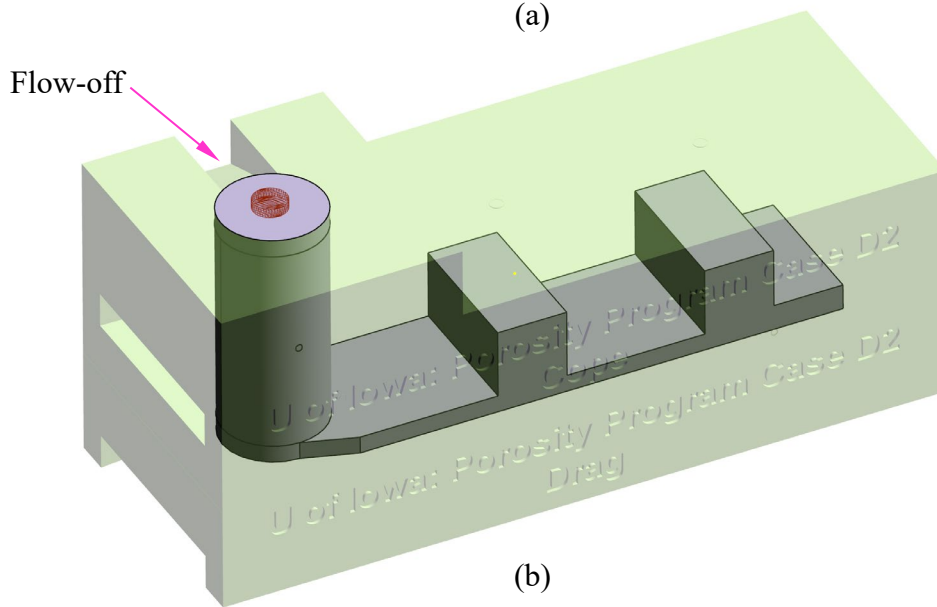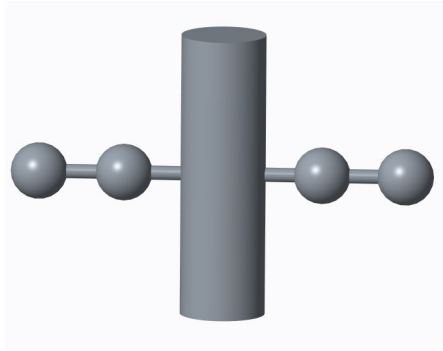
Figure 6. (a) Two rectangular-shaped hot spot block castings D1 and D2 poured in the first heat of experiments with dimensions. Casting simulation model (b) with semi-transparent mold and flow off location indicated.
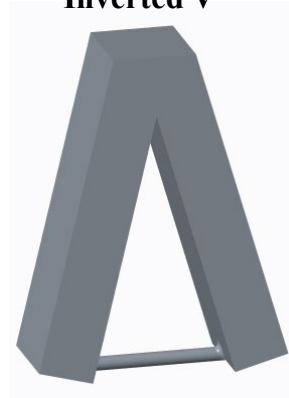
7

Cases A1 and A2:
4 Spheres

Case B:
Inverted V

Case A1: No thermocouple
Case A2: With thermocouple

Total volume: 88.2 in^3
Est. Weight: 25 lbs.
Steel: WCB
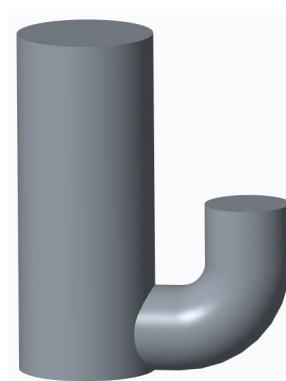
Total volume: 186.6 in^3
Est. Weight: 53 lbs.
Steel: WCB

Cases C1 and C2:
Blind riser, mid-height

Case D:
Blind riser, bottom
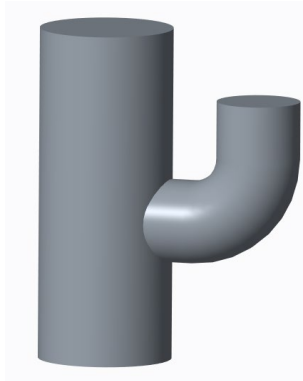
Case C1: No thermocouple
Case C2: With thermocouple

Total volume: 153.5 in^3
Est. Weight: 43.6 lbs.
Steel: WCB

Total volume: 153.5 in^3
Est. Weight: 43.6 lbs.
Steel: WCB

Figure 7. Geometries of the castings poured in the second heat of porosity experiments.

four cases had repeated experiments. In this Figure 7, experiments A1 and A2 had 4 spheres fed from a central downsprue/feeder. Experiment case B in this figure is an inverted V-shape; only one of this case was cast. Experiment cases C1 and C2 were cylindrical castings fed by a blind riser connecting at its mid-height. Then only one experiment for case D was performed, a cylindrical

casting fed by a blind riser connecting at its base. The results from these experiments were used to calibrate and validate the advanced feeding porosity model by considering some different porosity formation mechanisms from the experiments in the first heat. Cases A1 and A2 are similar to the hot spot blocks in the first heat of experiments, but internal macroporosity should form at the center of the spheres. The inverted V-shaped case B should form surface sink porosity at the peak of the V-shape, due to the superheated sand extending the solidification time at the mold-metal interface. Cases C1, C2 and D consider the feeding from blind risers, where the feeder is not connected to atmospheric pressure. Dimensions of the cases poured in the second heat of experiments are given in Figure 8 through Figure 10. Thermocouples were placed in castings A2 and C2 in this set of experiments.
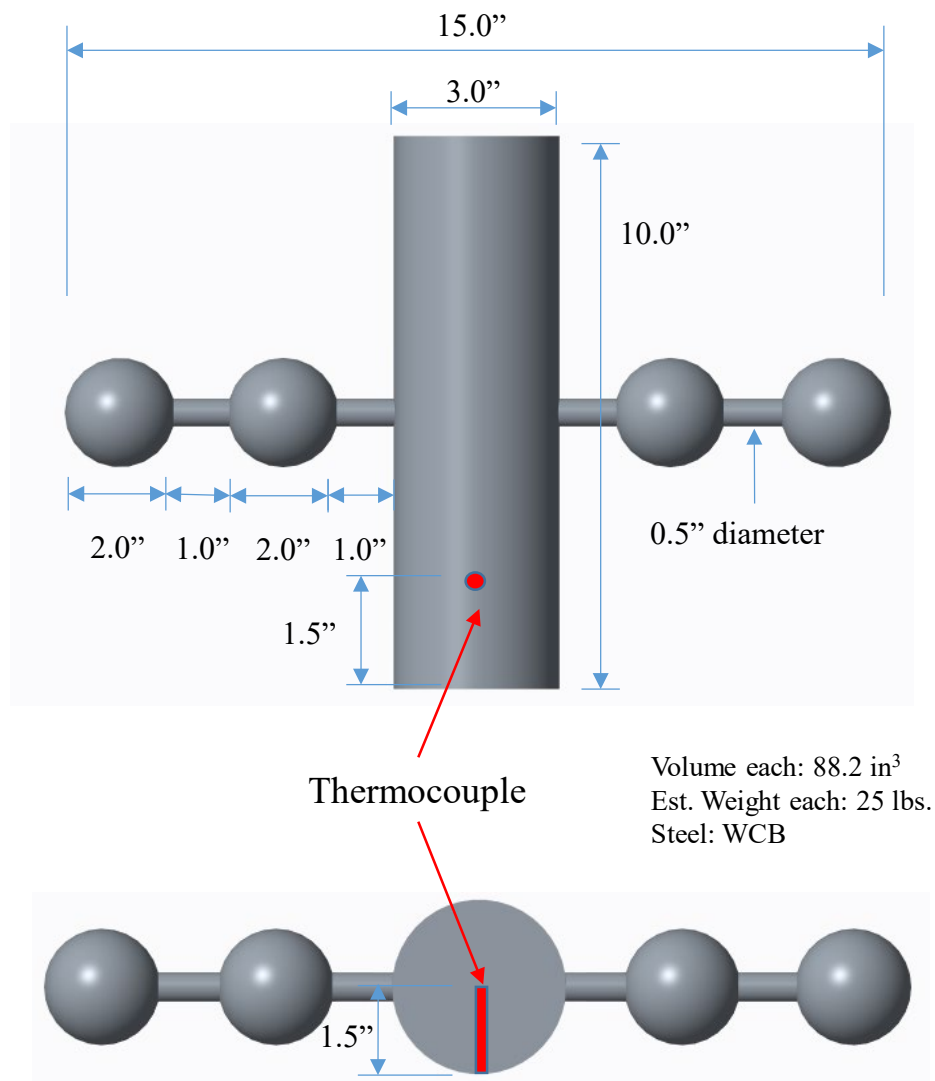
Figure 8. Dimensioned side and top views of porosity experiment case A with a large central sprue/feeder and four spherical castings showing location of thermocouple placement.
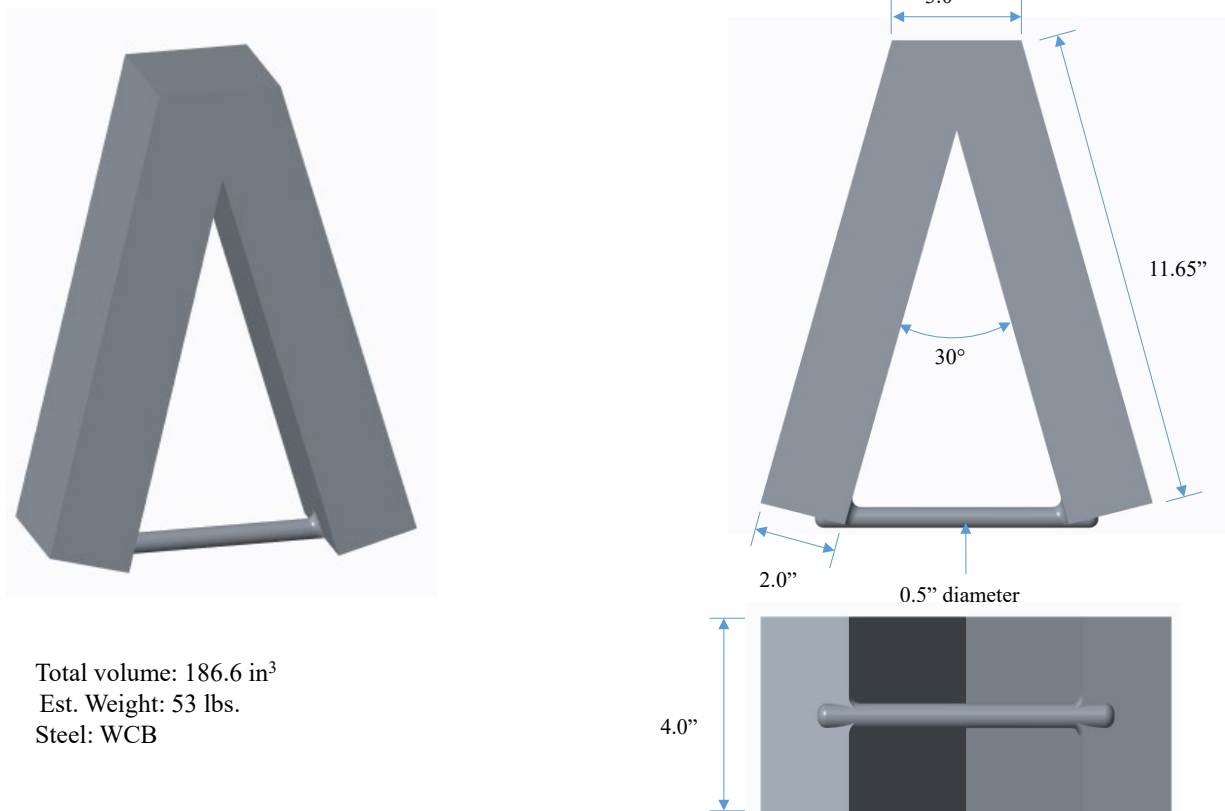
Total volume: 186.6 in^3
Est. Weight: 53 lbs.
Steel: WCB

3.0"

11.65"

30°

2.0"

0.5" diameter

4.0"

Figure 9. Dimensioned side and top views of the second heat experiment case B (the inverted V).

4.0"

2.0"

10.0"

4.25"

2.0"

Case C Thermocouple

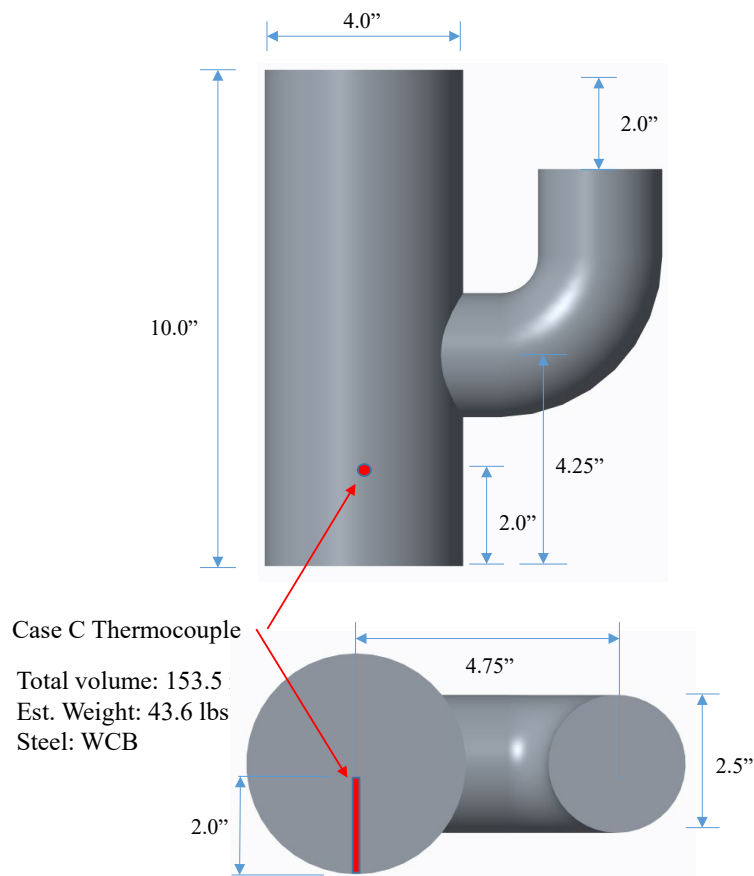Total volume: 153.5
Est. Weight: 43.6 lbs
Steel: WCB

4.75"

2.5"

2.0"

Figure 10. Dimensioned side and top views of porosity experiment case C (the blind riser at mid-height).
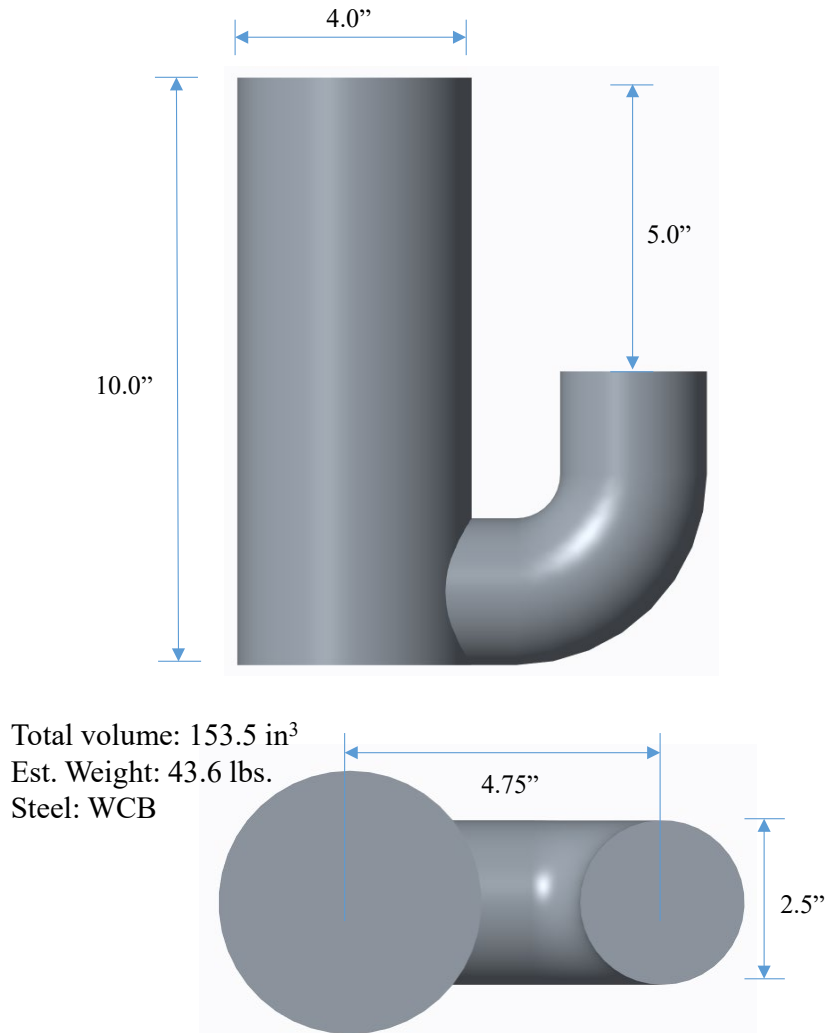
Figure 11. Dimensioned side and top views of porosity experiment case D (the blind riser with bottom contact).

2.2 Casting Simulation Procedures

The casting simulation thermophysical properties were validated by achieving agreement between measured and predicted temperatures from the experiments. In this process, numerous iterative casting simulations performed using *MAGMAsoft*, where the temperature dependent steel properties and solidification modeling parameters in the simulations were modified such that agreement was obtained between measured and predicted temperatures. Baseline properties for the steel were used based on previously developed properties for WCB steel. Initial simulations showed these calculated properties did not produce an acceptable agreement between predicted and measured temperatures recorded during the casting experiments. The temperature dependent steel properties and solidification parameters in the simulations were modified such that progressive agreement was obtained between measured and predicted temperatures. This iterative/comparative process for determining simulation properties is referred to as *inverse modeling*. The inverse modeling process was stopped once no better agreement could be obtained.

The advanced porosity model used here is a unified model for predicting macro-shrinkage porosity, surface sinks and micro-shrinkage porosity [3,4]. It was developed comparing its results to several casting experiments using a high manganese steel and an aluminum alloy. In these comparisons the following model features capabilities were demonstrated: 1) it accurately predicted location, amount and appearance of porosity, 2) porosity nucleates where solid fraction is lowest, 3) feeding flow velocities and pressures are calculated, 4) it accounts for entire shrinkage of alloy (no feeding effectivity needed), and 5) it accounts for dendrite coherency and mass feeding. A description of the model focusing on its important parameters is given below. A detailed reporting of the model including equations solves and other model detail is given elsewhere [3,4].

A schematic diagram of a solidifying casting volume described by the porosity model is shown in Figure 12. Multiple porosity regions of porosity can form simultaneously with boundary conditions at the casting surface and on volumes of porosity indicated in Figure 12(a). The model allows for a control volume in the casting to be composed of three phases: solid (s), liquid (l) and porosity (p). Using g to denote the volume fraction of a given phase, and the phases indicated by subscripts, the volume fractions must satisfy $g_l + g_s + g_p = 1$ as shown schematically in Figure 12(b). Key assumptions in the model are:

- Solid and porosity phases are stationary; they cannot move during solidification.
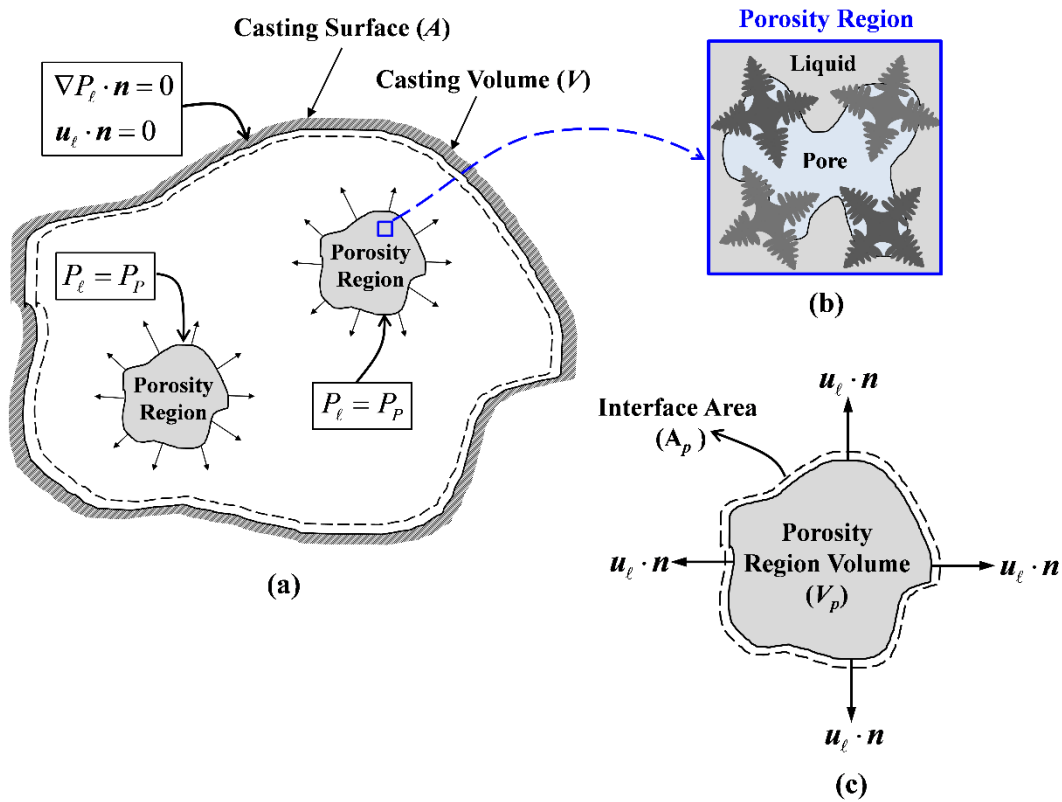

Figure 12. (a) Schematic diagram of solidifying casting volume with regions of porosity, (b) a representative volume from a region where porosity is forming, and (c) diagram of a region where porosity is forming.

- Flow movement only occurs by shrinkage in the system so buoyancy-driven flow during solidification is neglected.

Additional details of model development with describing equations and procedures for porosity prediction are given below. Much of the section below is taken directly from the T&O paper of Khalajzadeh and Beckermann [3].

Continuity and Momentum Equations

The solidifying mushy zone is composed of solid, liquid and porosity phases. For this zone, mass is conserved according to a mixture continuity equation given by

$$\frac{\partial \bar{\rho}}{\partial t} + \nabla \cdot \left(\rho_l \boldsymbol{u}_l \right) = 0 \tag{1}$$

where $\bar{\rho}$ is the metal mixture density defined as $\bar{\rho} = g_s \rho_s + g_l \rho_l$ with ρ_s being the density at solidus temperature, ρ_l is the density at liquidus temperature and $\boldsymbol{u}_l$ is the superficial velocity vector, which is defined as $\boldsymbol{u}_l = g_l \boldsymbol{v}_l$ where $\boldsymbol{v}_l$ is the liquid velocity vector. As mentioned above, the model assumes that the feeding flow in the mushy zone is a creeping flow and follows the assumptions for flows in porous media. For such flows the momentum equation can be modified to the equation know as Darcy's law, which is

$$\nabla P_{l,T} = -\frac{\mu_l \boldsymbol{u}_l}{K} + \rho_l \boldsymbol{g} \tag{2}$$

where $P_{l,T}$ is the total liquid pressure, μ_l is the melt dynamic viscosity, K is the permeability of the solidifying metal and $\boldsymbol{g}$ is the gravity vector. The total liquid pressure ($P_{l,T}$) is defined as the sum of dynamic liquid pressure (P_l) and the hydrostatic pressure (P_h) so that $P_{l,T} = P_l + P_h$. Applying the gradient operator to this equation

$$\nabla P_{l,T} = \nabla P_l + \nabla P_h \tag{3}$$

where the hydrostatic pressure gradient (∇P_h) is given by $\nabla P_h = \rho_l \boldsymbol{g}$. Combining Eq. (2) and (3) the gravity terms cancel and Eq. (2) is simplified to

$$\nabla P_l = -\frac{\mu_l \boldsymbol{u}_l}{K} \tag{4}$$

It is assumed that the permeability of the solidifying metal K is a function of solid fraction (g_s) and can be described by the Kozeny–Carman equation

$$K = K_0 \frac{(1 - g_s)^3}{g_s^2} \tag{5}$$

where K_0 is a constant permeability coefficient in the current study. Minimum and maximum limiting values for K are defined as K_{min} and K_{max}, respectively, to avoid numerical problems. These two parameters are alloy dependent and are determined by parametric study.

A reference liquid pressure is needed to determine a solution for Eq. (4). Here it is assumed that P_l within regions having porosity is equal to the pore pressure, $P_l\big|_{Porosity} = P_p$. The value of pore pressure P_p depends here on location; at the atmosphere-metal interface it is atmospheric pressure, $P_p = P_{atm}$, at the mold-metal interface $P_p = P_{mold}$ and for internal porosity $P_p = 0$.

Assuming that ρ_l is constant during solidification, Eqs. (1) and (4) can be combined to form an equation for determining the pressure P_l throughout the casting during solidification

$$\nabla \cdot \left(-\frac{K}{\mu_l} \nabla P_l \right) = -\frac{1}{\rho_l} \frac{\partial \bar{\rho}}{\partial t} \tag{6}$$

Eq. (6) is a Poisson Equation, an elliptical partial differential equation requiring two boundary conditions to have a valid solution. Here one boundary condition is determined by the condition to solve Eq. (4) that $P_l\big|_{Porosity} = P_p$, and the second is provided by the zero-mass flux condition at the casting walls, which is $(\mathbf{u}_l \cdot \mathbf{n})_{Surface} = (\nabla P_l \cdot \mathbf{n})_{Surface} = 0$. These boundary conditions are shown schematically in Figure 12. Using these boundary conditions, the pressure distribution P_l in casting is determined by solution of Eq. (6). The expanded form of Eq. (6) in 3D Cartesian coordinates is

$$\frac{\partial}{\partial x}\left(\frac{K}{\mu_\ell} \frac{\partial P_\ell}{\partial x} \right) + \frac{\partial}{\partial y}\left(\frac{K}{\mu_\ell} \frac{\partial P_\ell}{\partial y} \right) + \frac{\partial}{\partial z}\left(\frac{K}{\mu_\ell} \frac{\partial P_\ell}{\partial z} \right) = \frac{1}{\rho_\ell} \frac{\partial \bar{\rho}}{\partial t} \tag{7}$$

which is discretized and solved using a finite volume approach.

After P_l is calculated, the total pressure ($P_{l,T}$) is calculated

$$P_{l,T} = P_l + P_h \tag{8}$$

where P_h is the hydrostatic pressure given by $P_h = \rho_l g(z_{max} - z)$ and $(z_{max} - z)$ is the hydrostatic head from a reference height of z_{max}. The velocity distribution in the casting due to the shrinkage driven flow is determined by solving Eq. (4) for $\mathbf{u}_l$

$$\mathbf{u}_l = -\frac{K}{\mu_l} \nabla P_l \tag{9}$$

The velocity components from Eq. (9) are

$$u_\ell = -\frac{K}{\mu_\ell}\left(\frac{\partial P_\ell}{\partial x} \right) \quad ; \quad v_\ell = -\frac{K}{\mu_\ell}\left(\frac{\partial P_\ell}{\partial y} \right) \quad ; \quad w_\ell = -\frac{K}{\mu_\ell}\left(\frac{\partial P_\ell}{\partial z} \right) \tag{10}$$

where u_ℓ, v_ℓ, w_ℓ are the superficial liquid velocity component in x, y, z directions. The nucleation and growth of porosity based on the calculated pressure follows next.

Pore Nucleation

The calculated pressure field is used to predict the nucleation of a pore in the liquid metal. Pore nucleation is assumed to occur heterogeneously at pre-existing nucleation sites in the mushy zone. Pores can only nucleate if the energy needed to overcome the capillary pressure is provided. Since gas porosity is not considered in this work, this nucleation energy is provided by large pressure drops due to flow resistance in the solidifying mush in the absence of any dissolved gas in the casting. Considering this nucleation mechanism, the pore nucleation criterion is given by the inequality form of Young-Laplace equation

$$P_p - P_{l,T} \geq P_\sigma \tag{11}$$

where, $P_{l,T}$ is the total liquid pressure which is defined as $P_{l,T} = P_l + \rho_l g(z_{\max} - z)$; P_P is the pore pressure, and P_σ is the capillary pressure due to surface tension. According to experimental observations [5], surface sink and shrinkage porosity tend to nucleate first in the areas with low solid fractions, as in the case of a hot spot in Figure 3(b). Therefore, during solidification pores nucleate preferentially in regions with more liquid. As a result, the model presented here assumes that the capillary pressure in the solidifying metal P_σ is a linear function of the solid-fraction g_s

$$P_\sigma = P_{\sigma,0} \times g_s \tag{12}$$

where $P_{\sigma,0}$ is a constant coefficient which is an alloy dependent parameter. Using Eq. (12) in Eq. (11) the nucleation criterion is more easily met if the solid fraction is low. Furthermore, it is also assumed that after nucleation, due to the small surface curvature at the pore-liquid interfaces, P_σ in the porosity region become negligibly small. Therefore, it is assumed that $P_\sigma = 0$ in regions with porosity.

As mentioned above, surface sinks and internal porosity start forming or nucleate in locations where the solid fraction is the lowest. On the surface of a casting, it is possible that this lowest solid fraction occurs simultaneously at multiple locations. Among those locations, surface sinks form only where the metallostatic head pressure is relatively low. For internal porosity, there can also be multiple locations or computational cells where the solid fraction is uniformly low. An example would be a large internal region at the center of a casting section that is still fully liquid. Again, within such a region of uniform low solid fraction, porosity is found to nucleate only at the location where the metallostatic head pressure is the lowest. Based on these observations, the nucleation criterion (Eq. 11) is applied using a parameter Π that incorporates the effects of both solid fraction and metallostatic head pressure to determine which cells will form porosity. The parameter Π is

$$\Pi = P_{\ell,T} - \left(P_p - P_\sigma\right) \tag{13}$$

with nucleation taking place at those locations in the casting where the Π parameter is lowest (see below for additional detail). To make the porosity calculations independent of rounding errors and the time-step used in the numerical simulations, porosity is nucleated in all computational cells where the Π value falls within a small dimensionless interval ε_{nuc} according to

15

$$\left| \frac{\Pi - \Pi_{min}}{\Pi_{max} - \Pi_{min}} \right| < \varepsilon_{nuc} \qquad (13)$$

where Π_{min} is the minimum and Π_{max} is the maximum Π value in the region of the casting, respectively. A suitable value for ε_{nuc} that gives good agreement between observed and calculated porosity nucleation patterns is determined by parametric study. Physically, ε_{nuc} controls the size of a region where porosity nucleates. Once porosity nucleates in a computational cell, it becomes an "active" cell.

Surface Coherency and Porosity Location

The model does not distinguish between surface sinks and internal porosity. Both are treated as shrinkage porosity. Observations [5] indicate that the two types of porosity do not evolve simultaneously, but in a two-stage process. First surface sinks develop, and then internal porosity forms. The transition between the two stages is assumed to occur when the solid fraction everywhere on the casting surface exceeds a certain critical value, $g_{s,sur}$. When the solid fraction at the surface is below this critical value as shown in Figure 13, the equiaxed solid dendrites and the melt can both move to accommodate the volume deficit due to solidification shrinkage and surface sink porosity forms. Once the solid fraction everywhere on the surface is above $g_{s,sur}$, the dendrites form a coherent and rigid solid network that prevents any further displacement of the surface. Then, the solidification shrinkage must be accommodated by internal porosity. Theoretically, the melt between the rigid dendrites at the casting surface could still move, but such
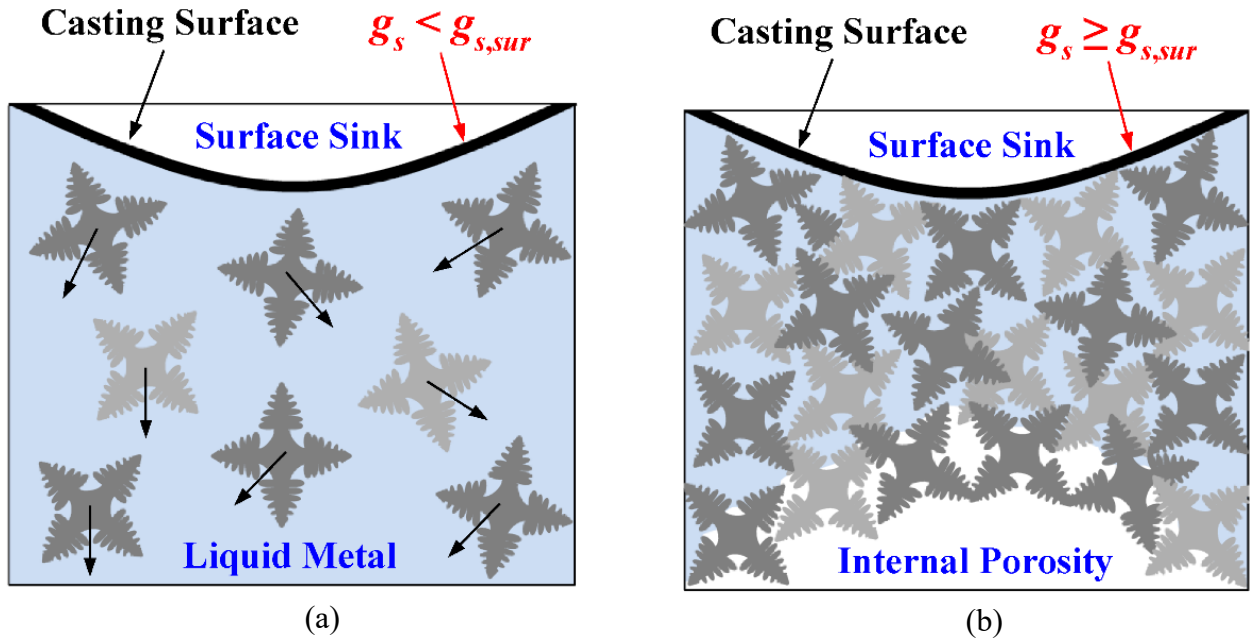
Figure 13. Schematic diagram of surface sink and internal porosity formation: (a) for the dendrites and the melt can move and a surface sink forms; (b) once dendrites form a coherent and rigid network; the surface stops moving and internal porosity forms inside of the casting.

16

movement would be resisted by relatively high capillary forces.

Porosity is nucleated only if there are no active computational cells already present in the computational domain. An active cell is defined as a cell where porosity is currently growing (see also below). As long as there is a possibility of surface sinks forming, i.e., if there are surface cells where $g_s < g_{s,sur}$, the nucleation calculations are performed only for surface cells and internal cells are ignored. As soon as $g_s > g_{s,sur}$ everywhere on the surface of a calculation region of the casting, internal computational cells where the Π parameter satisfies Eq. (13) are activated.

Pore Growth

As shown in Figure 2(a), multiple regions of porosity can nucleate and grow in a casting. Each region is a grouping of connected computational cells having $g_p > 0$ in the model (as discussed below). The volume of a given region of the casting with porosity forming is V_p. Once nucleated, the growth of porosity within a region of the casting is calculated from the pore growth rate ($d\overline{g}_p/dt$), which is determined applying the mass conservation law at the interface of pore-liquid interface. In Figure 2(c) a region with porosity having volume of V_p and the interface area of A_p is shown. The mass conservation law for the region with porosity is given by

$$\int_{V_P}\left(\frac{\partial\overline{\rho}}{\partial t}\right)dV + \int_{A_P}(\rho_\ell \boldsymbol{u}_\ell)\cdot\boldsymbol{n}\,dA = 0 \tag{14}$$

where $\overline{\rho}$ is the alloy mixture density, $\boldsymbol{u}_\ell$ is the superficial velocity vector and $\boldsymbol{n}$ is the normal vector to the interface. Two approaches are commonly used to define $\overline{\rho}$ during solidification. In one approach, a two-phase mixture of solid and liquid ($\overline{\rho}^{SL}$) is used. In the other a three-phase mixture of solid, liquid, and porosity ($\overline{\rho}$) is used. The two-phase mixture density, $\overline{\rho}^{SL}$, is defined as $\overline{\rho}^{SL} = \rho_s g_s^{SL} + \rho_\ell g_\ell^{SL}$ where $g_s^{SL} + g_\ell^{SL} = 1$. The three-phase mixture density, $\overline{\rho}$, is defined by $\overline{\rho} = \rho_s g_s + \rho_\ell g_\ell + \rho_p g_p$ where $g_\ell + g_s + g_p = 1$. Combining these two approaches, and assuming $g_s^{SL} = g_s$ and $\rho_p << \rho_s, \rho_\ell$, the following equation is derived for $\overline{\rho}$ as a function of $\overline{\rho}^{SL}$, ρ_ℓ, and g_p

$$\overline{\rho} = \overline{\rho}^{SL} - \rho_\ell g_p \tag{15}$$

By replacing $\overline{\rho}$ in Eq. (14) with Eq. (15) and defining that the average pore fraction in a region of the casting is $\overline{g}_p = \left(\int_{V_P} g_p dV\right)\Big/V_P$, the average porosity growth rate for a porosity region ($d\overline{g}_p/dt$) can be calculated using

$$\frac{d\overline{g}_p}{dt} = \frac{1}{\rho_\ell V_p}\int_{V_P}\left(\frac{\partial\overline{\rho}^{SL}}{\partial t}\right)dV + \frac{1}{V_p}\int_{A_P}\boldsymbol{u}_\ell\cdot\boldsymbol{n}\,dA \tag{16}$$

The average porosity growth rate ($d\overline{g}_p / dt$) for a region of the casting with porosity is

calculated by integrating Eq. (16) over the volume and surface area of the calculation region. This is done numerically to calculate the average porosity growth ($\Delta \bar{g}_p$) for each region using

$$\Delta \bar{g}_p = \frac{1}{\rho_\ell V_p} \sum_{i=1}^{N_P} \left(\Delta \bar{\rho}_i^{SL} \times \Delta V_i \right) + \frac{\Delta t}{V_p} \sum_{i=1}^{N_{P-L}} \left(\boldsymbol{u}_{\ell,i} \cdot \boldsymbol{n}_i \Delta A_i \right) \tag{17}$$

where V_p is the volume of the porosity region, N_P is the number of porosity cells inside the region, ΔV_i volume of individual cells, Δt is the computational time-step, and N_{P-L} is the number of porosity cells at the porosity-liquid interface. Note that $\boldsymbol{u}_{\ell,i}$ and $\boldsymbol{n}_i$ are vectors and the calculations are performed considering all directions.

In order to predict the local porosity distribution in pore forming regions additional assumptions must be made. The main assumption made is that the solidification shrinkage volume is distributed evenly over all active computational cells where porosity is currently growing for each numerical time interval in the calculations. Applying this assumption, the corresponding shrink volume is determined for a given region using

$$\Delta V_{Shrink} = \Delta \bar{g}_p \times V_p \tag{18}$$

If ΔV_{Shrink} is distributed uniformly across all active cells in a porosity region then the change in porosity fraction in all active cells is

$$\Delta g_p = \Delta V_{Shrink} / V_{Active} \tag{19}$$

where V_{Active} is the volume of active cells. The pore-fraction for all active cells are updated by accumulating the change in porosity from growth using

$$g_p^{new} = g_p^{old} + \Delta \bar{g}_p \tag{20}$$

The pore volume fraction in each active computational cell is initially zero and can be allowed to increase until the cell becomes empty of liquid, which implies that $g_s + g_p = 1$. However, this condition might result in the local pore fraction never reaching unity ($g_p = 1$). A pore fraction of unity corresponds to a surface sink or large internal hole that is free of solid, both of which are readily possible. For the pore volume fraction to reach unity, the previously grown solid at that location must have been moved or pushed away by the growing porosity. This is a process frequently referred to as "mass feeding". Mass feeding can only occur if the solid fraction is below a so-called coherency solid fraction $g_{s,coh}$, i.e., when $g_s < g_{s,coh}$. Above this coherency solid fraction, the dendrites form a rigid solid network that cannot move. The coherency solid fraction

might be expected to take the same value as the previously introduced critical value $g_{s,sur}$ at which surface sinks stop forming. With these considerations, the maximum pore volume fraction $g_{p,\max}$ is given by

$$g_{p,\max} = \begin{cases} 1 & \text{for} \quad g_s < g_{s,coh} \\ 1 - g_s & \text{for} \quad g_s \geq g_{s,coh} \end{cases} \tag{21}$$

Here the two critical solid fractions $g_{s,sur}$ and $g_{s,coh}$ are retained as separate parameters to allow for additional flexibility in tuning the model.

Applying Eq. (21), a computational cell that reaches the maximum pore fraction becomes inactive. Once there are no longer active cells present in the porosity forming region, and if solidification is not yet complete, new cells must be activated to accommodate the additional solidification shrinkage. Such activation is accomplished using the same Π parameter introduced in the earlier subsection, but only for those computational cells that neighbor a cell with porosity already present. The latter condition ensures that porosity grows by spreading in layers around regions with preexisting porosity, rather than by nucleating in other regions of the casting where no porosity is present. In other words, spreading of existing porosity is assumed to be easier than nucleating new porosity. Hence, cells that neighbor a cell where $g_p \neq 0$ are activated when their Π parameter falls within the interval

$$\left| \frac{\Pi - \Pi_{\min}}{\Pi_{\max} - \Pi_{\min}} \right| < \varepsilon_{layer} \tag{22}$$

The small dimensionless number ε_{layer} is a model parameter that controls the rate of spreading of porosity regions. For model tuning flexibility, ε_{layer} is allowed to take a value different from ε_{nuc}, and its value was determined using a parametric study as well.

The porosity algorithm described above is applied to regions of porosity throughout the casting. These regions must be identified and tracked throughout the solidification process. A search algorithm is used to identify all porosity regions in the casting. In the image processing literature, the algorithm used is termed the "connected-component labeling" algorithm. This approach also finds applications in other technologies such as computer graphics, CAD modeling software and mapmaking [6], and it is used to identify subsets of connected regions in an image having any dimension [6]. For example, a 2D image might be an x-ray, and a 3D image might be a computed tomography scan of a volume. In this applying this method to porosity modeling, the porosity field is converted to a binary field first using a thresholding function

$$Binary\ Value = \begin{cases} 0 & g_p = 0 \\ 1 & g_p > 0 \end{cases} \tag{23}$$

If a cell has no porosity ($Binary\ Value = 0$) the cell is termed a background cell. While cells

with porosity (*Binary Value*=1) are foreground cells and the connected regions in the foreground are determined and grouped. By the search algorithm as applied from reference [6], the porosity regions are identified throughout the entire casting. Then the liquid pressure in the porosity regions are forced to the values of pore pressure P_p discussed earlier ($P_p = P_{atm}$ at the atmosphere-metal interface, $P_p = P_{mold}$ at the mold-metal interface and $P_p = 0$ for internal porosity). Then feeding flow equations (7) and (9) are solved to obtain the pressure and velocity distributions in the casting, respectively. Finally for each region of porosity, Eq. (17) is calculated to determine the average pore growth ($\Delta \bar{g}_p$) and the porosity formed in the region from Eq. (19), and the updated porosity is determined from Eq. (20).

3.   Results

3.1 Temperature Measurements and Simulation Results

Results for the First Heat of Porosity Experiments

Iterative simulations were performed for the cylinder casting instrumented with a thermocouple (TC) from the first set porosity experiments. The goal of the simulations was to adjust temperature dependent properties and boundary conditions in the castings simulation to obtain agreement between the temperature measurements and the simulations. By adjusting these properties and conditions, the best possible agreement was obtained between temperature measurements and simulations as described below in more detail. Simulations began by using some previously developed WCB steel temperature dependent properties. The measured and simulated cooling history data are shown in Figure 14 for a short time scale to 500 seconds in Figure 14(a) and to 2000 seconds in Figure 14(b). The simulation temperature-time curve (or cooling curve) is consistently hotter than the measured curve. Additional insight into the solidification of the steel is obtained by plotting the cooling rate-temperature data for the measurements and simulations. These curves are plotted in Figure 3 for the simulation result using the previously developed WCB steel temperature dependent properties (black symbols) and for the measurements (using magenta symbols). The minimum value inflection points at the higher temperatures in Figure 15 are the liquidus temperatures, and the maximum value inflection points at the lower temperatures are the solidus temperatures. The vertical lines in Figure 15 are the measured liquidus and solidus temperatures determined from the figure.

After approximately fifty simulations where the solid fraction-temperature curve (also termed solidification curve) and other parameters (such as latent heat, and temperature dependent thermal conductivity and specific heat) were adjusted iteratively, the best agreement was obtained between the measurements and simulations. The solid fraction-temperature curve determined to give the best agreement between measurements and simulations is shown in Figure 16. Comparisons between the measured and best-agreement simulating cooling curves and cooling rate-temperature curves are shown in Figure 17 and Figure 18, respectively. Comparing Figure 17 with Figure 14(a), a dramatic improvement in agreement between the measured and simulated cooling curves was achieved. Similarly, comparing Figure 18 with Figure 15, a dramatic improvement in agreement between the measured and simulated cooling rate-temperature curves was obtained. As mentioned in the introduction, the temperature dependent density curve, which is determined from the solidification curve and the temperature dependent density curves for the pure solid and liquid phases, is very important in predicting the shrinkage porosity of the steel. The density curve determined from the iterative simulations is shown in Figure 19(a) for the full temperature range, and in Figure 19(b) for the solidification temperature range (1412 to 1499 ºC). The property dataset determined from this work was used in the parametric studies continued to determine the porosity model parameters that give the best agreement between predicted porosity and the observed porosity for the first set of casting experiments.
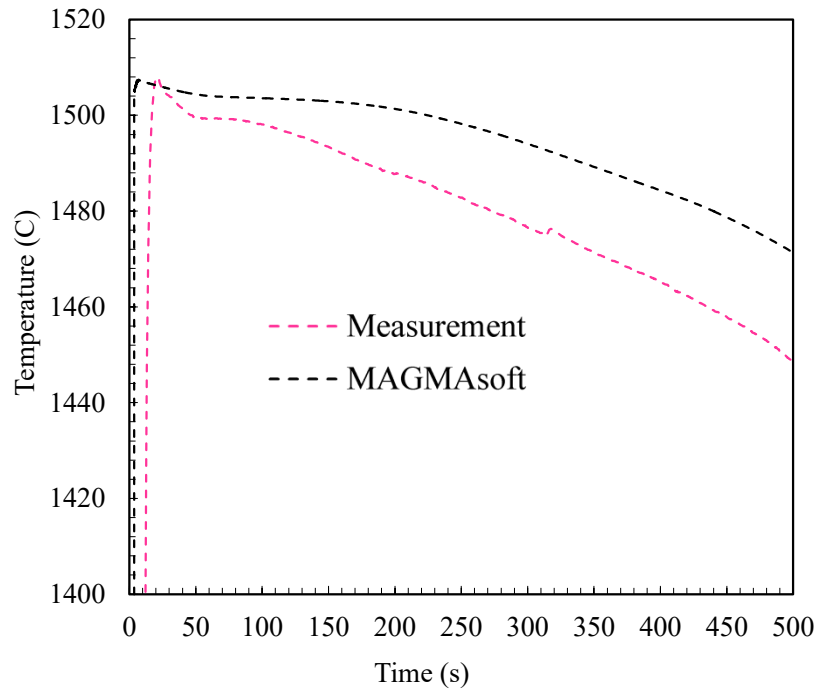
(a)
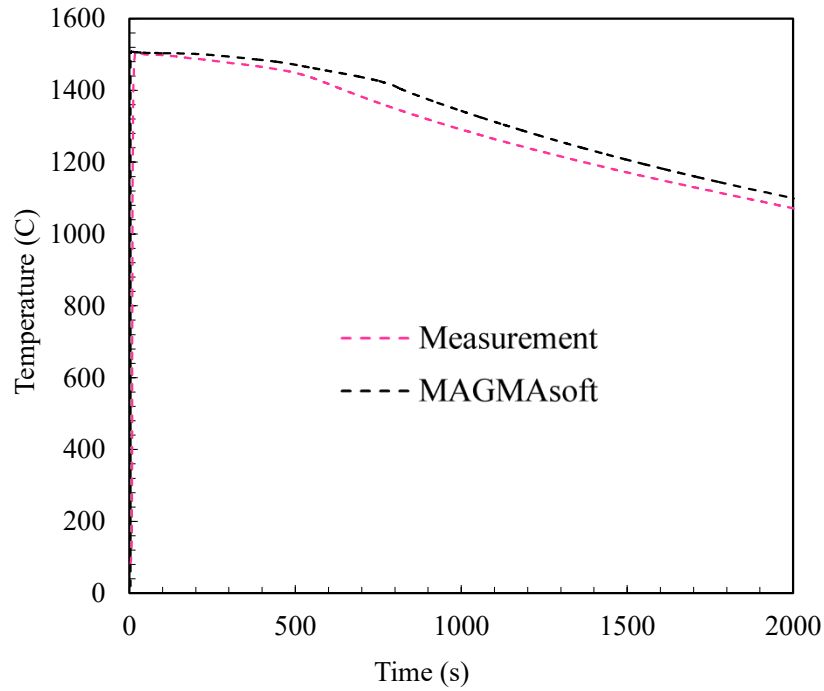
(b)

Figure 14. Temperature versus time cooling curves comparing the measured data and the simulations results using the software's database properties for WCB steel on a time scale to 500 seconds in (a), and to 2000 seconds in (b).
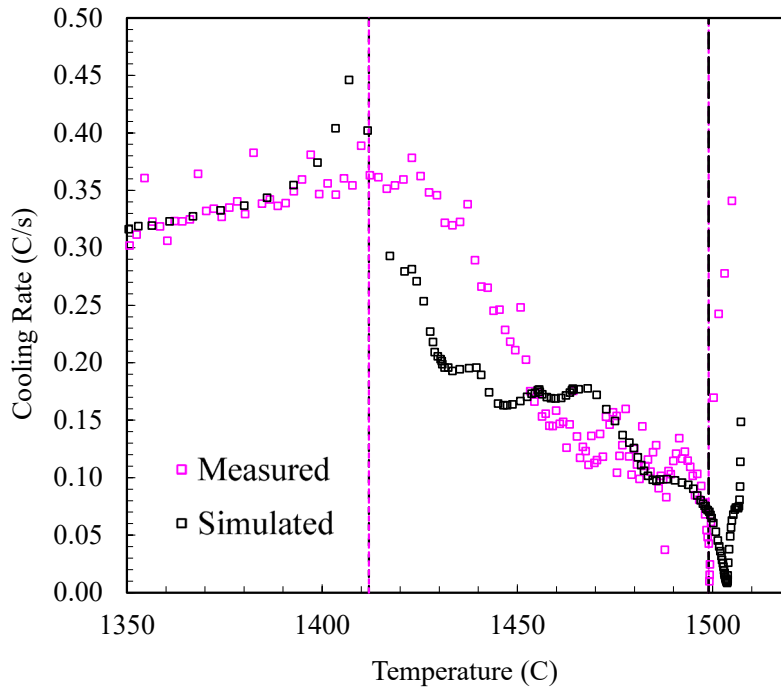
Figure 15. Cooling rate-temperature curves for the measurement (magenta symbols) and starting simulation case (black symbols)
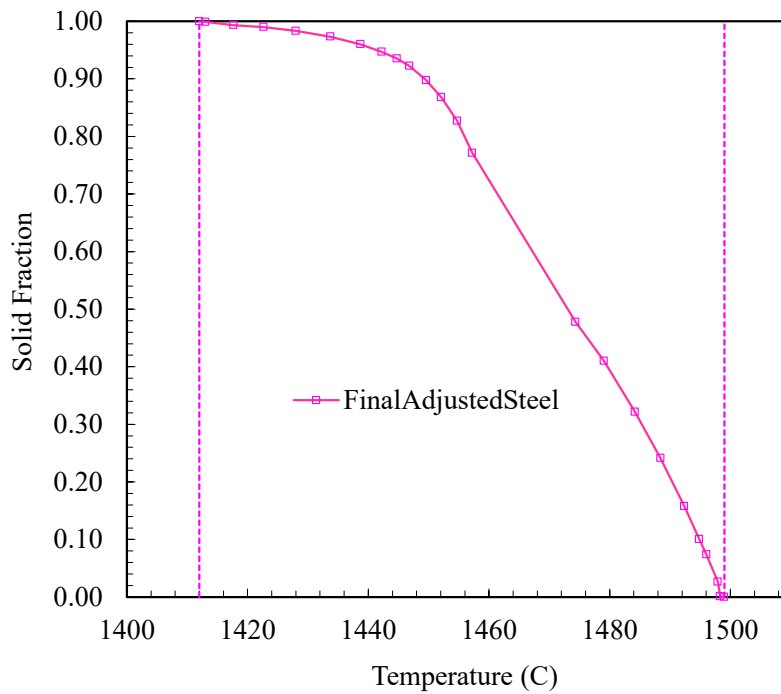
Figure 16. Solid fraction-temperature curve (also termed solidification curve) determined to give the best agreement between measurements and simulations.
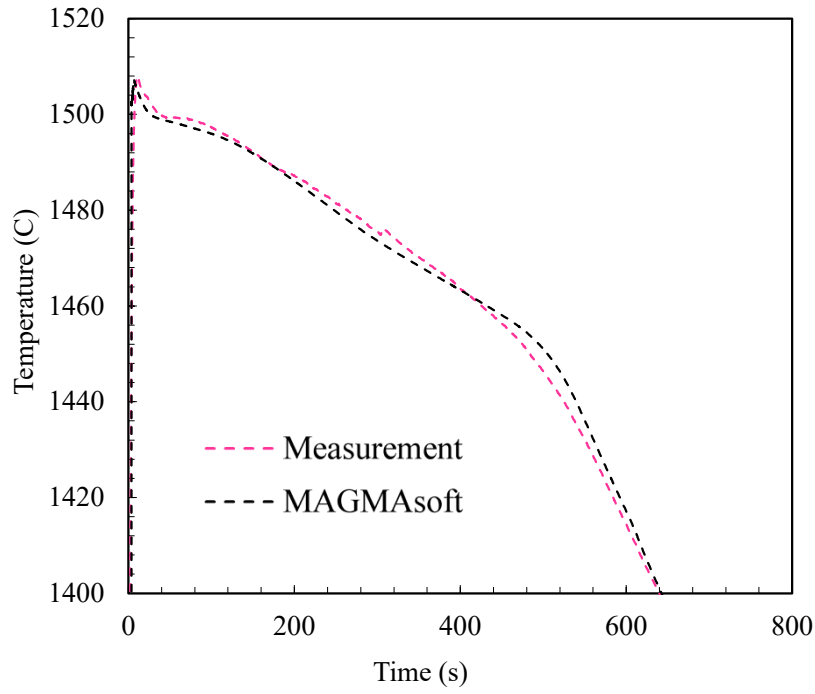
Figure 17. Comparison between the measured and best-agreement simulating cooling curves.
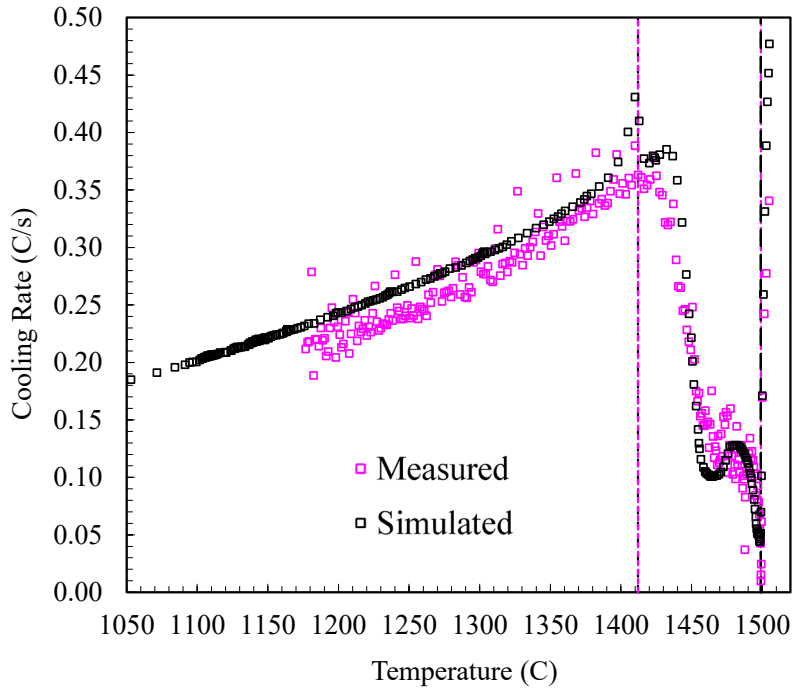
Figure 18. Comparison between the measured and best-agreement simulating cooling rate-temperature curves.

24
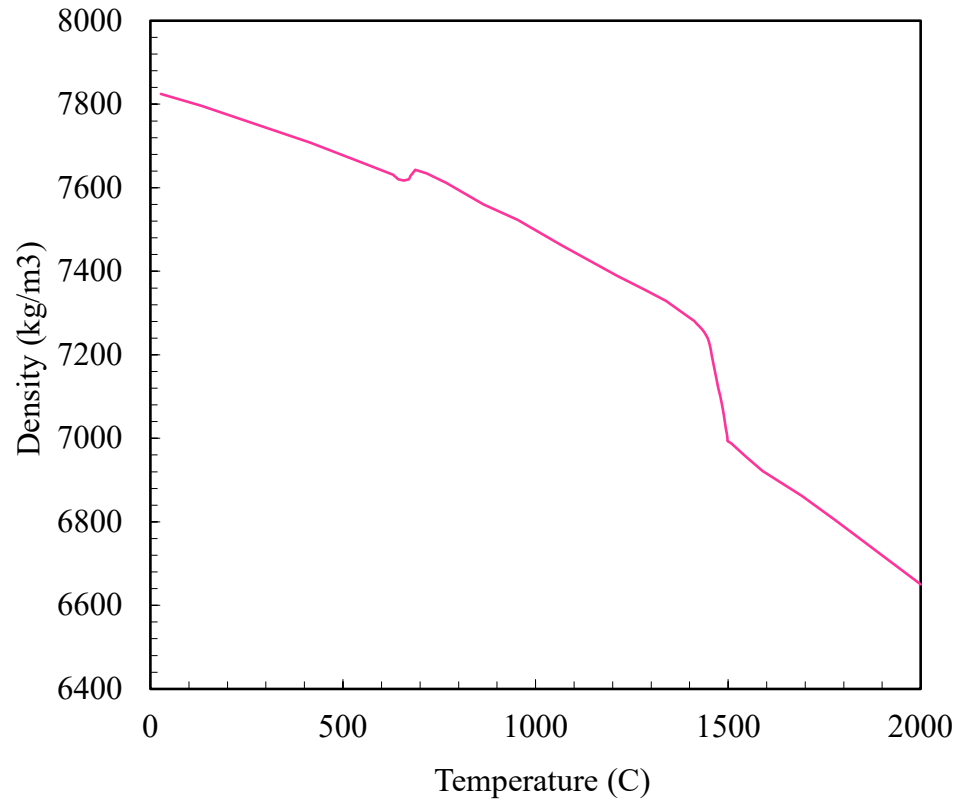
(a)
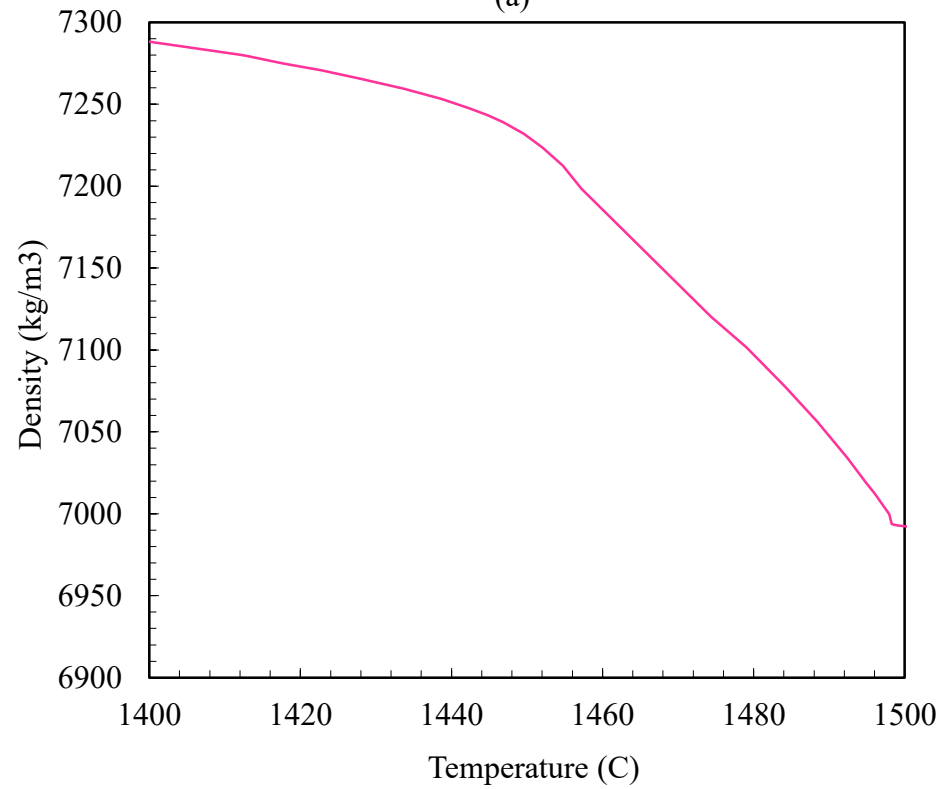
(b)

Figure 19. Temperature dependent density curves obtained for the best-agreement simulation property data for the full temperature range (a) and for the solidification

Results for the Second Heat of Porosity Experiments

Thermocouple (TC) data from one of the six porosity experiments poured during October was analyzed during November. The TC data analyzed was from the experiment case C2. This was a cylindrical casting fed by a blind riser connecting at its mid-height. The analysis performed was inverse modeling; iteratively modifying model parameters and properties until the best match was achieved between measured and predicted temperatures from the experiments. Approximately 40 iterative simulations were performed until the final match between the measured and simulated TC data was determined. The best property data (such as temperature dependent density curve in the solidification range) and final match in the measured and simulated TC agreement should give the best possible porosity prediction compared to the experiments.

In Figure 1 temperature history results the starting simulation case is compared to the measured temperatures. The simulation case uses the WCB steel alloy properties from the MAGMAsoft database. Three curves are shown in Figure 1 near the liquidus temperature (a), throughout the solidification range (b), and for a larger temperature range to around 400 ˚C below solidus temperature. From the curves in Figure 1, the response time for the TC is seen to be around 20 seconds. The simulations predict slower cooling than the measurements indicate. In addition to matching the temperature history (temperature versus time) for the experiment, the measured and simulated cooling rates versus temperature are also compared and matched as closely as possible in the inverse modeling process. These results are shown in Figure 2 for the starting simulation case using the WCB alloy data from the MAGMAsoft property database. In Figure 2(a) the point where the cooling rates initially go to 0 is the liquidus temperature. The simulated liquidus temperature is lower than the measurement, and it will be adjusted. The simulated cooling rates below 1485 ˚C are lower than the measurements. Adjusting the temperature-solid fraction curve (also referred to as the solidification curve) which prescribes the solidification behavior of the steel, should improve the cooling rate agreement. In Figure 2 curves are shown are near the liquidus temperature in (a), throughout the solidification range in (b), and for a larger temperature range to around 400 ˚C below solidus temperature in (c). In Figure 2, vertical lines are at the measured liquidus and solidus temperatures.

As mentioned above, after over 40 iterative inverse modeling simulations, the best obtained properties and modeling conditions were determined. The temperature history comparisons between simulations and measurements are shown in Figure 3. The cooling rate versus temperature data for the simulations and measurements are shown in Figure 4. Using these "best" properties and modeling conditions (i.e. pouring temperature, and temperature dependent boundary conditions between steel and mold), the comparisons between measurement and simulation are excellent based on prior experience using inverse modeling. The solidification data found to give the best agreement between TC measurements and simulations is shown in Figure 5. In Figure 6 the temperature-solid fraction curve determined from matching thermocouple data and temperature dependent density curve derived from solid fraction curve. This temperature dependent density curve is important for accurate prediction of the porosity formation.
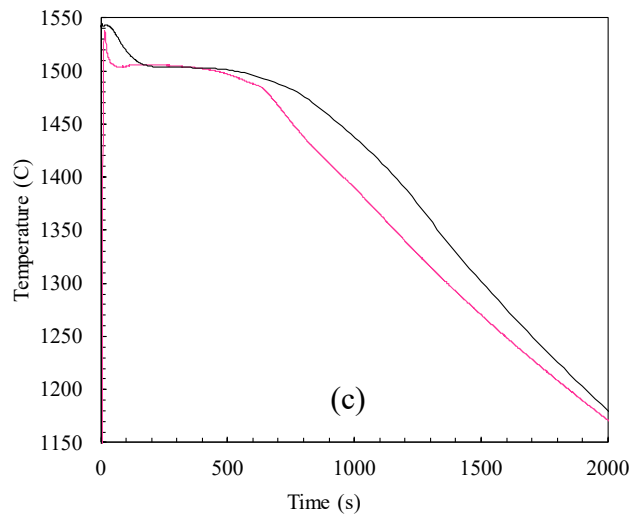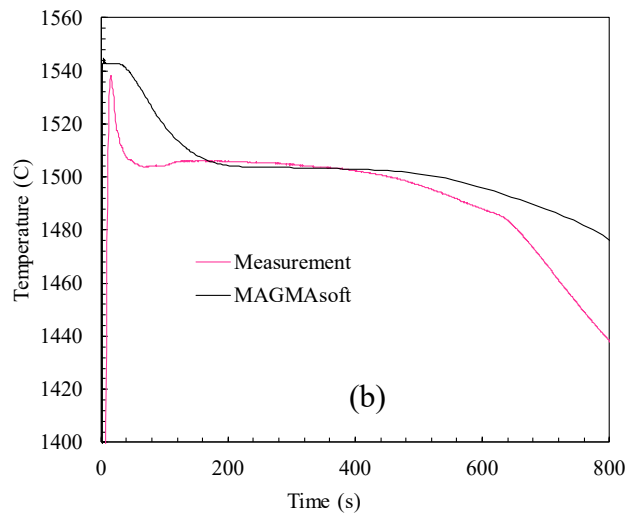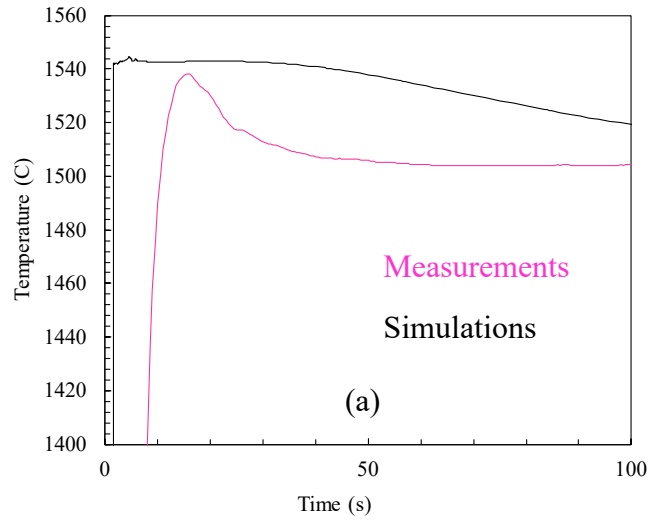
Figure 20. Measured and simulated temperature history curves for the second heat of experiments. Curves are near the liquidus temperature (a), throughout the solidification range (b), and for a temperature range to around 400 ˚C below solidus temperature. Simulations use initial unoptimized WCB data.
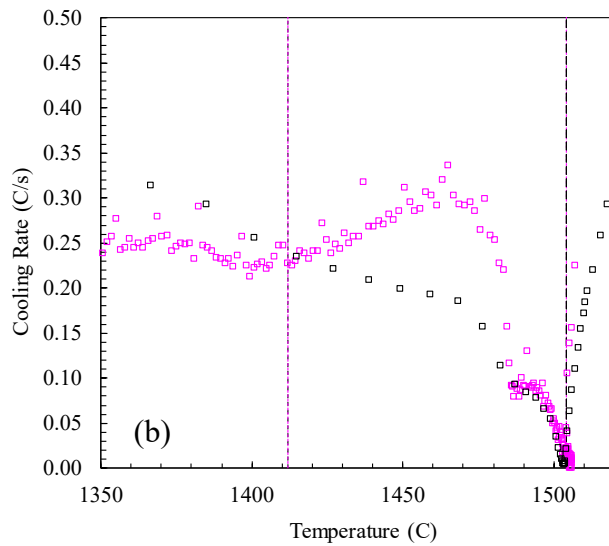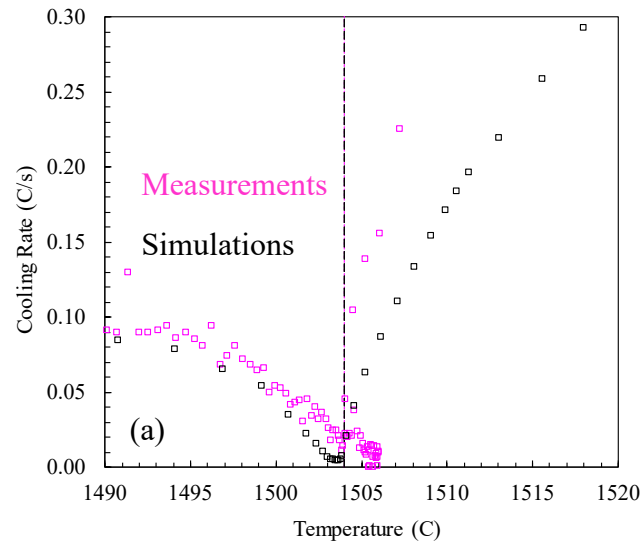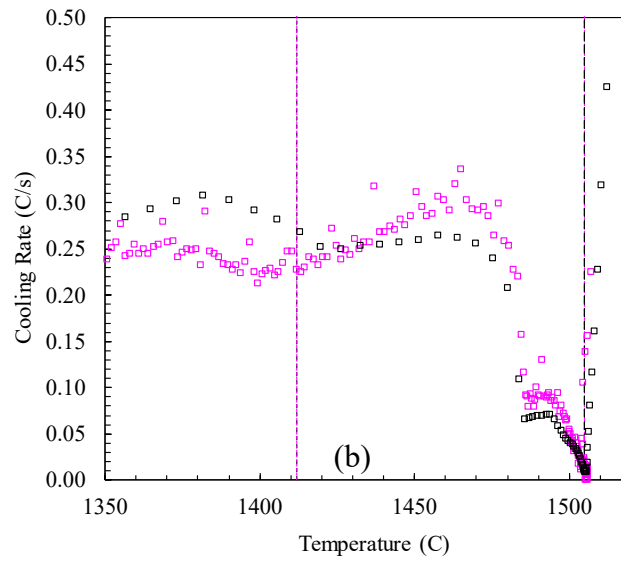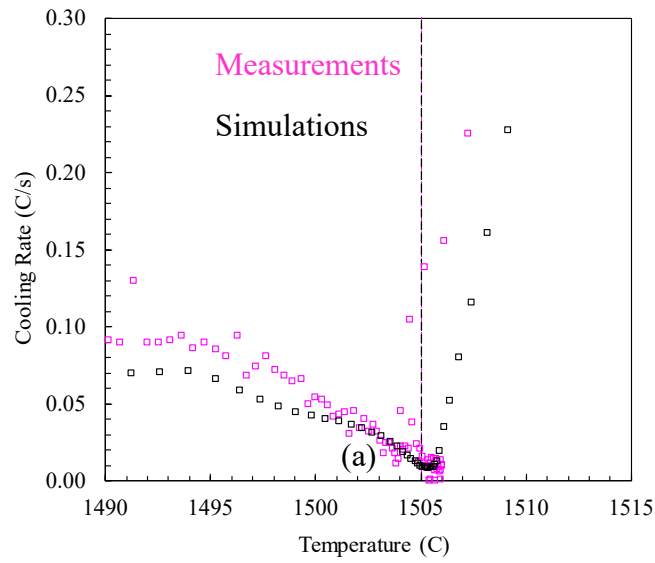
27
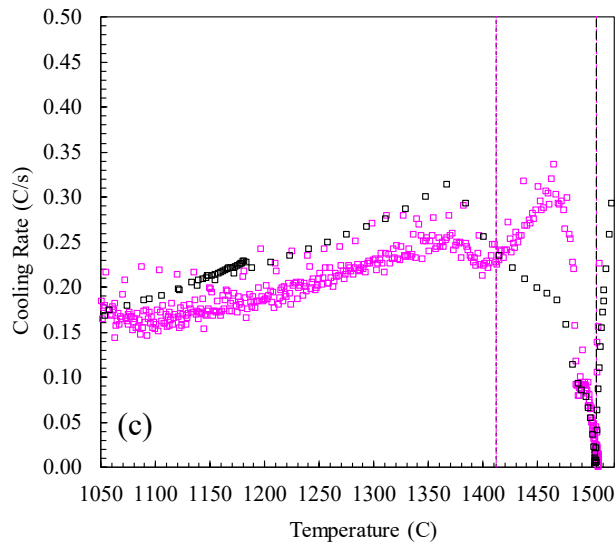
Figure 21. Measured and simulated cooling rates versus temperature for the second heat. Curves are shown are near the liquidus temperature (a), throughout the solidification range (b), and for a larger temperature range to around 400 ˚C below solidus temperature. Simulations use initial unoptimized WCB data. Vertical lines are at the measured liquidus and solidus temperatures.
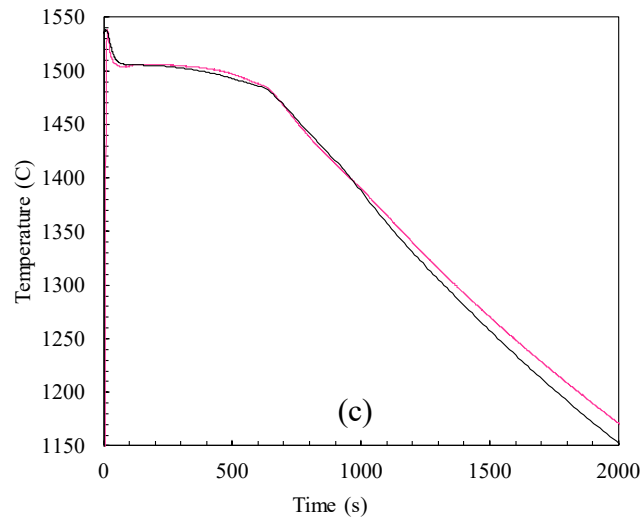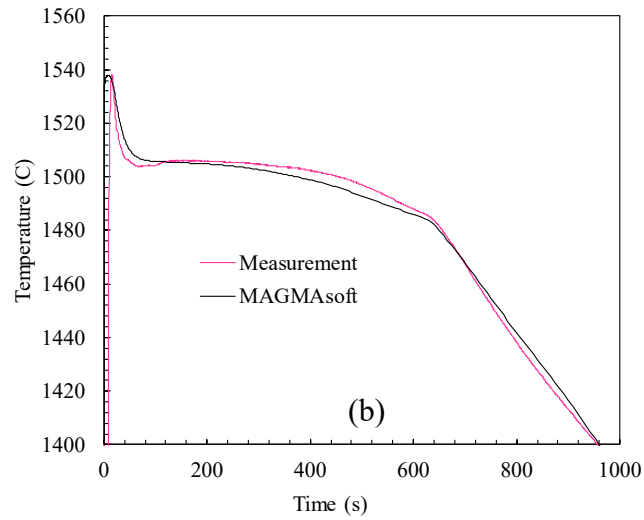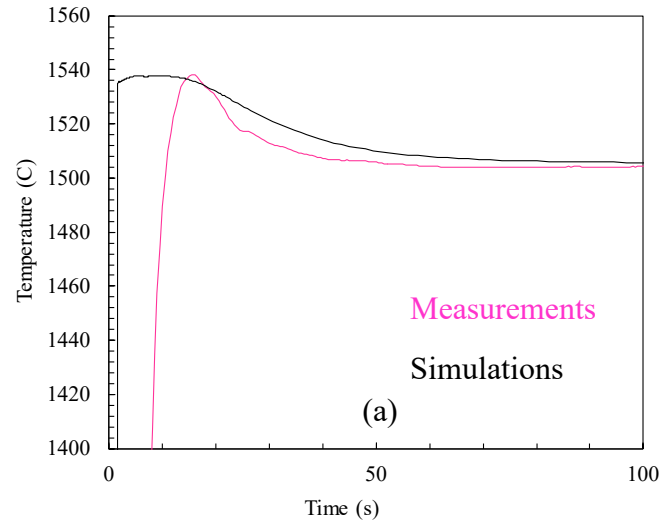
Figure 22. Measured and simulated temperature history curves for the second porosity experiment case using a blind riser. Curves are shown near the liquidus temperature (a), throughout the solidification range (b), and for a larger temperature range to around 400 ˚C below solidus temperature. Simulations use properties that were found to give the best match measured and predicted temperatures.

29
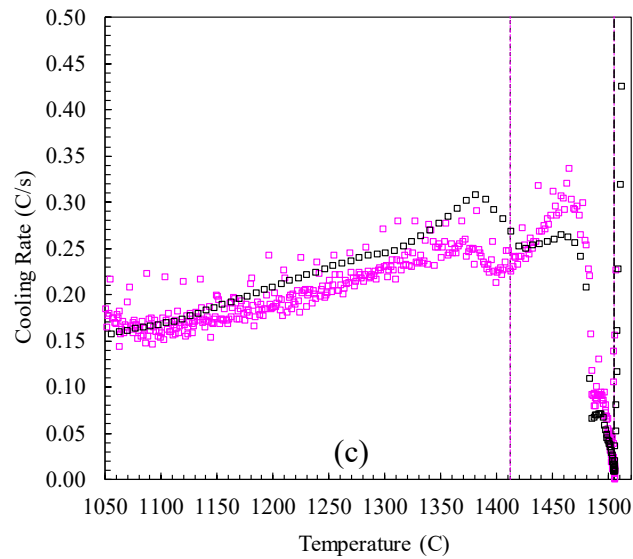
Figure 23. Measured and simulated cooling rates versus temperature for the second heat. Curves are shown are near the liquidus temperature (a), throughout the solidification range (b), and for a larger temperature range to around 400 °C below solidus temperature. Simulations use best properties that match measured and predicted temperatures. Vertical lines are at the measured liquidus and solidus temperatures.

30

Figure 24. Solidification data found to give the best agreement between TC measurements and simulations.
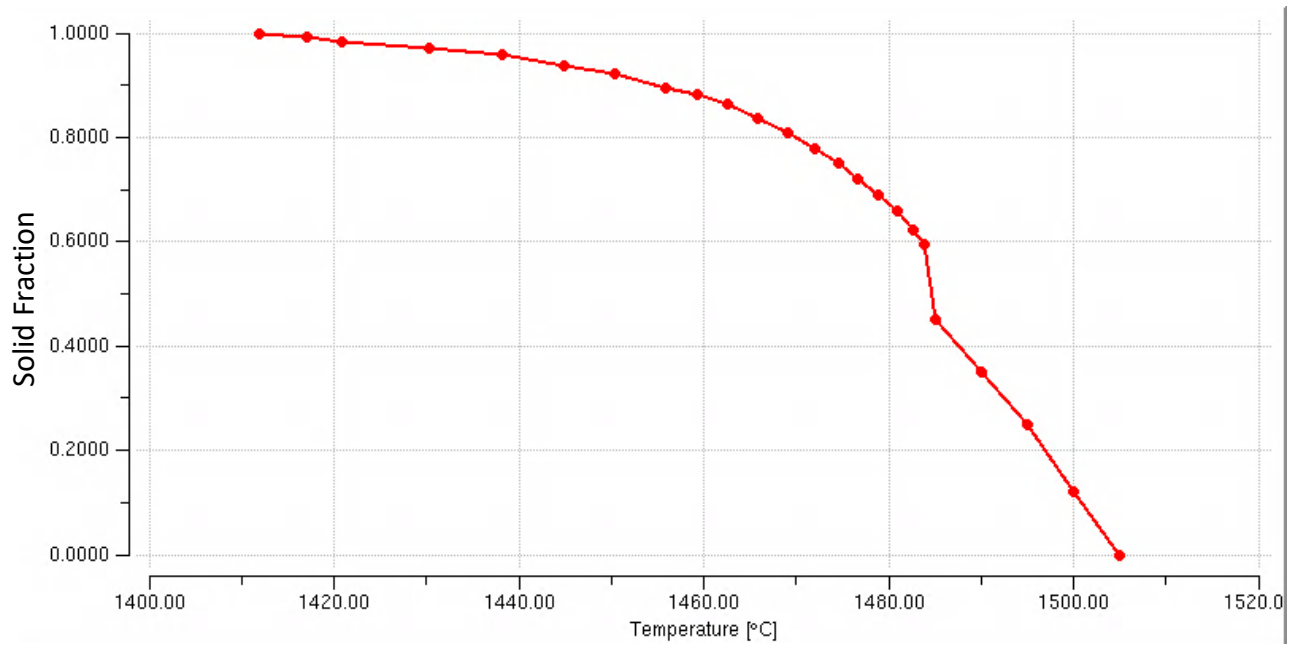
(a)
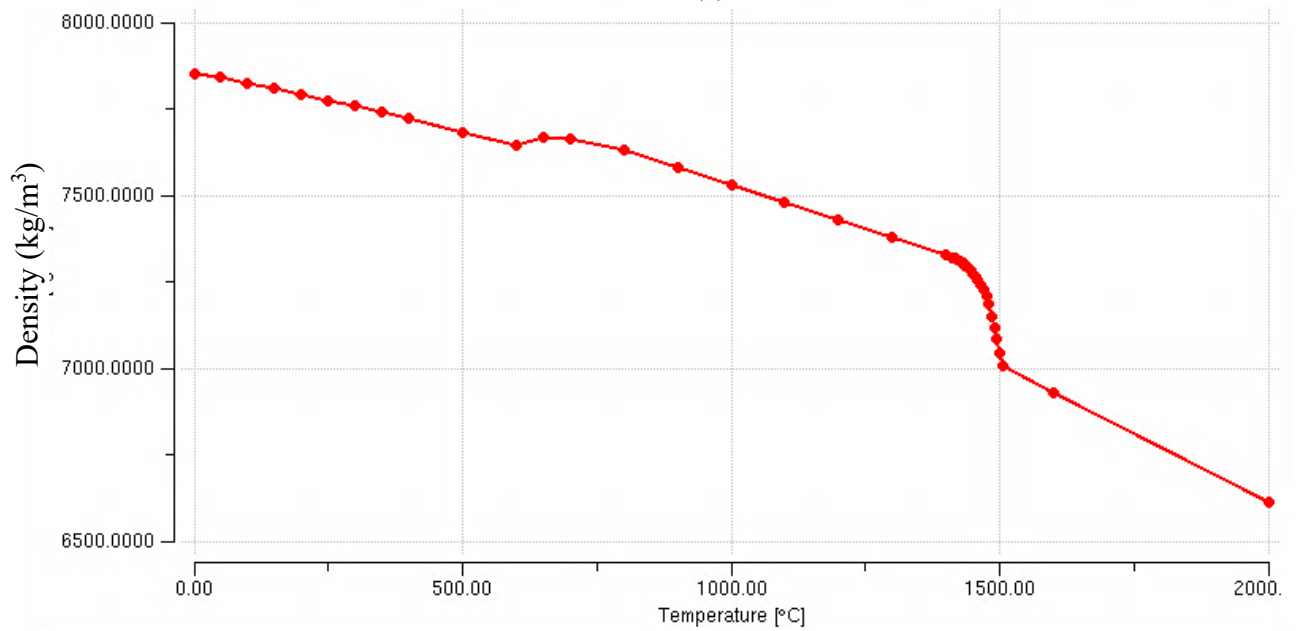
(b)

Figure 25. (a) Temperature-solid fraction curve (as referred to as the solidification curve) determined from matching thermocouple data from second set of porosity experiments, and (b) temperature dependent density curve derived from solid fraction curve.

3.2 Porosity Experiment Results

Results for the First Heat of Porosity Experiments

Seven castings were poured in the first heat of casting experiments: five of which were cylindrical castings, and two were rectangular-shaped hot spot block castings. In Figure 26, Figure 27 and Figure 28 the detailed pouring data for the heat 1 experiments are given for the straight cylinders, inverse-tapered and taper cylinders, and the hot spot block castings, respectively. The pouring data were determined from videos taken from two cameras. The pouring data are the pouring time, pouring stream angle and pouring stream diameter. The figures also indicate the inlet stream location entering the top of the castings relative to the ladle position and the overflow. The simulations were performed using filling, and this pouring data, to model the experiments as accurately as possible. The casting pour order for the experiments was A1, A2, A3, B, C, D1 and D2.

The results of the porosity distributions on the sections of the experiments are given in Figure 29, Figure 30, Figure 31 and Figure 32 for the straight cylinders, inverse-tapered and taper cylinders, and the two hot spot block castings, respectively. Cross sections of three straight cylinder experiments are shown in Figure 29 (labeled A1, A2 and A3), where the porosity shrinkage piping is clear and similarly distributed along the casting length in each case. The location of the overflow is shown in the small image in the upper right at the top of the mold. In the porosity sections images the overflow location is indicated by the green block. Note the solid shell at the top of the casting surface and the thickness of the shell at the top of each casting. This solid shell forms early in the solidification process before the long centerline shrinkage piping forms. However, before the solid shell forms, a surface ink forms that appears as the sucked-in concave top surface of the shell. The centerline shrinkage porosity forms after the top surface sink and shell and it extends downward into the casting extending over about 3/4th of the upper length of the casting. The bottom quarter of the casting length appears sound and free of macroporosity. The bottom end of the castings cools fastest due to the "end-effect" of the mold surrounding the bottom end of the casting.

The porosity observed on the cross sections of the inverse-tapered and tapered cylinders from the heat 1 porosity experiments are shown in Figure 30. The location of the overflow is indicated by the green block. Again, there is a solid shell and surface sink at the top of the casting surface and the centerline shrinkage porosity extends downward into the casting. The vertical extent of the shrinkage porosity is much longer for the inverted-taper case B than the much shorter length of porosity in the tapered case C. The taper case has a much shorter length of porosity than the straight cylinders as well. The inverted-taper case has a shrinkage pipe length that appears slightly longer than the straight cylinder "A" cases. These results will be compared to the simulated porosity distributions later.

In Figure 31 the porosity observed on the cross sections of the hot spot block casting D1 from the heat 1 porosity experiments is shown. Several sections were made on each side of the mid-width plane, at the centerline and 0.08", 0.25" and 0.331" offset from the centerline. The cylindrical feeder porosity distribution looks very similar to the cylinder castings. There is a slight surface sink, solid shell and shrinkage pipe a little longer than half the feeder height in the feeder.

Looking at the porosity in the hot spot blocks, the porosity is located at the center of the blocks. The block at the end of the plate has a much larger porosity amount than the block closer to the feeder. The sections from the centerline also show that the extent of the porosity in the block nearest the end of the plate is longer in the width direction as well. The height dimension of the porosity block at the end of the plate is larger than its length. The casting in Figure 32 was poured short and was not compared to the simulations. The porosity distribution on its mid-width section is included here to completely report on the experiment results.

Case A1
Pour time: 9.0s
Pour angle: 76°
Stream diam.: 0.8"

Case A2
Pour time: 10.0 s
Pour angle: 77°
Stream diam.: 0.8"

Case A3
Pour time: 6.5 s
Pour angle: 65°
Stream diam.: 0.7"

Straight Cylinder with Hot Top

Straight Cylinder

Straight Cylinder with TC

Pour stream location
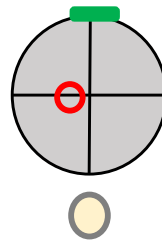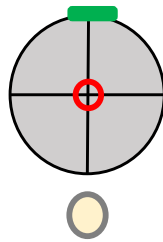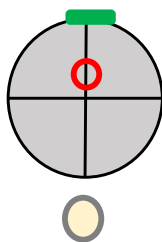
▬ Overflow location
O Inlet position
◯ Ladle position

Figure 26. Pouring data for the straight cylinder castings from heat 1 experiments.

Case B
Pour time: 8.0 s
Pour angle: 65°
Stream diam.: 0.7"

Case C
Pour time: 7.0 s
Pour angle: 63°
Stream diam.: 0.8"

Inverse Tapered
Cylinder
2.5" to 3.5"

Tapered
Cylinder
3.5" to 2.5"
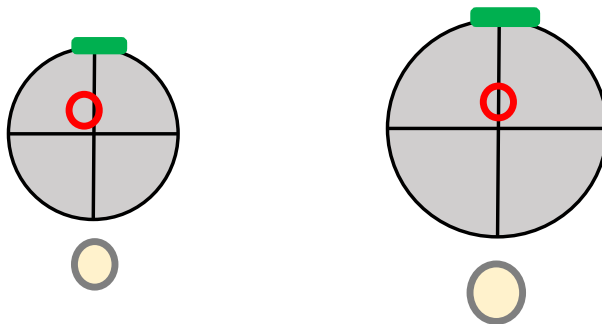
━━ Overflow location
◯ Inlet position
◯ Ladle position

Figure 27. Pouring data for the inverse-tapered and tapered cylinder castings from heat 1 experiments.

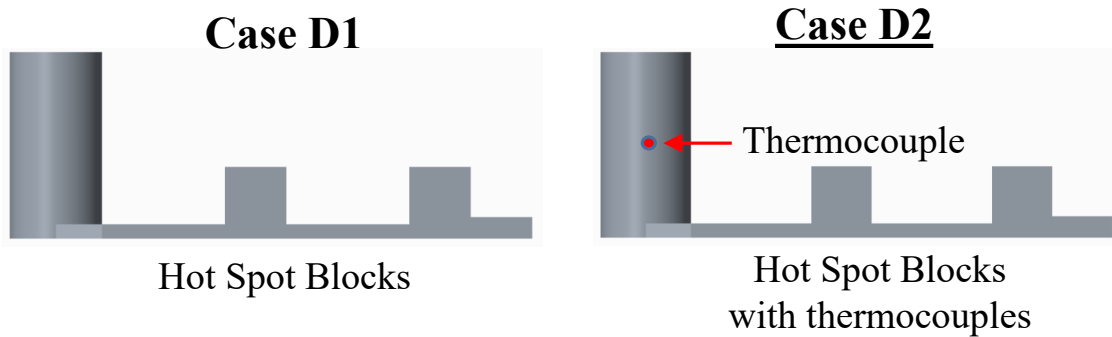**Case D1**

Pour time: 7.0 s
Pour angle: 67°
Stream diam.: 0.7"

Case D2

Pour time: 11 s
Pour angle: 67°
Stream diam.: 0.6"

Case D1

Hot Spot Blocks

Case D2

Thermocouple

Hot Spot Blocks
with thermocouples

Overflow location
Inlet position
Ladle position

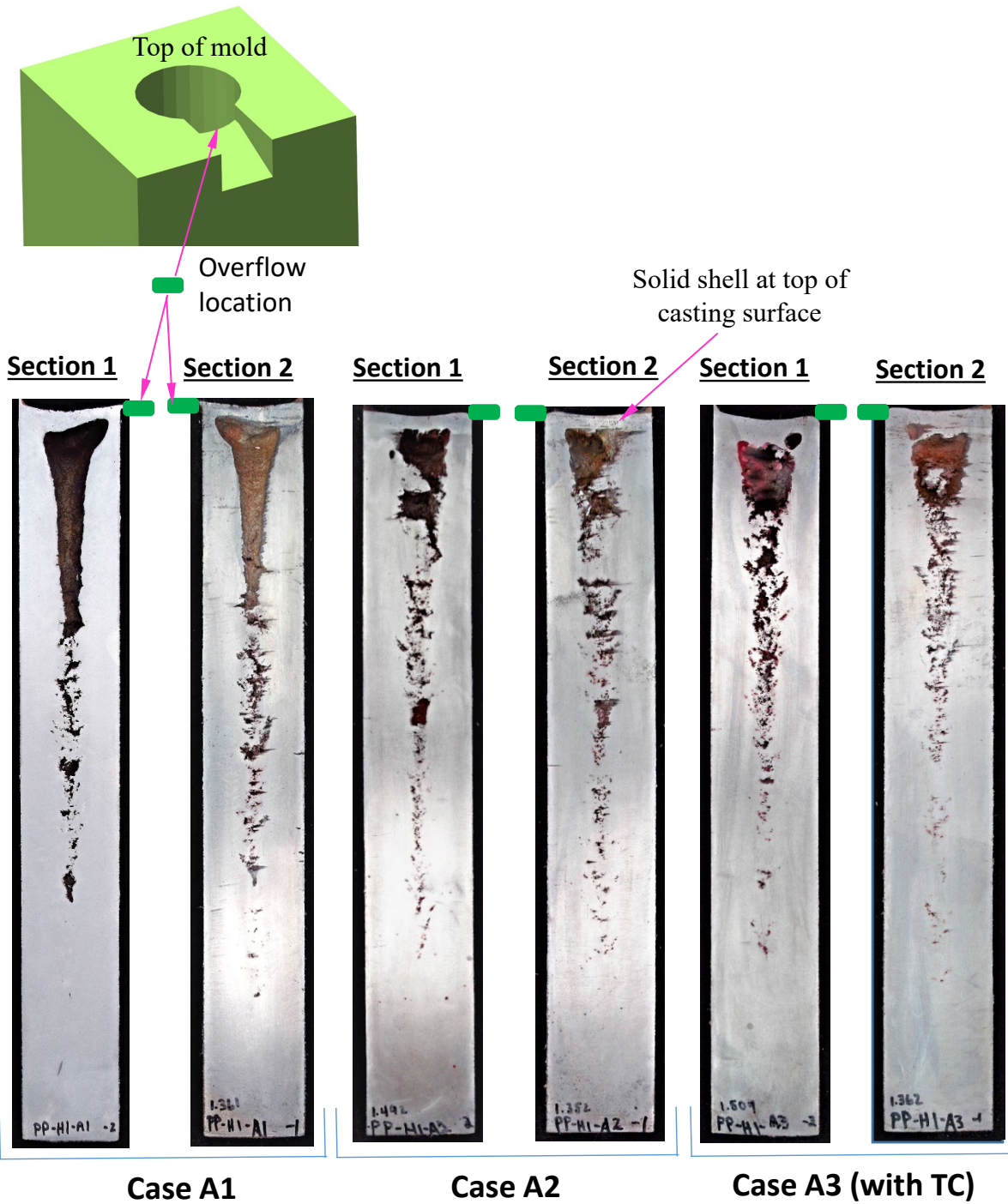Figure 28. Pouring data for the hot spot block castings experiments from heat 1.

Figure 29. Porosity observed on the cross sections of the straight cylinders from the heat 1 porosity experiments. Location of the overflow shown. Note the solid shell at the top of the casting surface and the centerline shrinkage porosity extending downward into the casting.
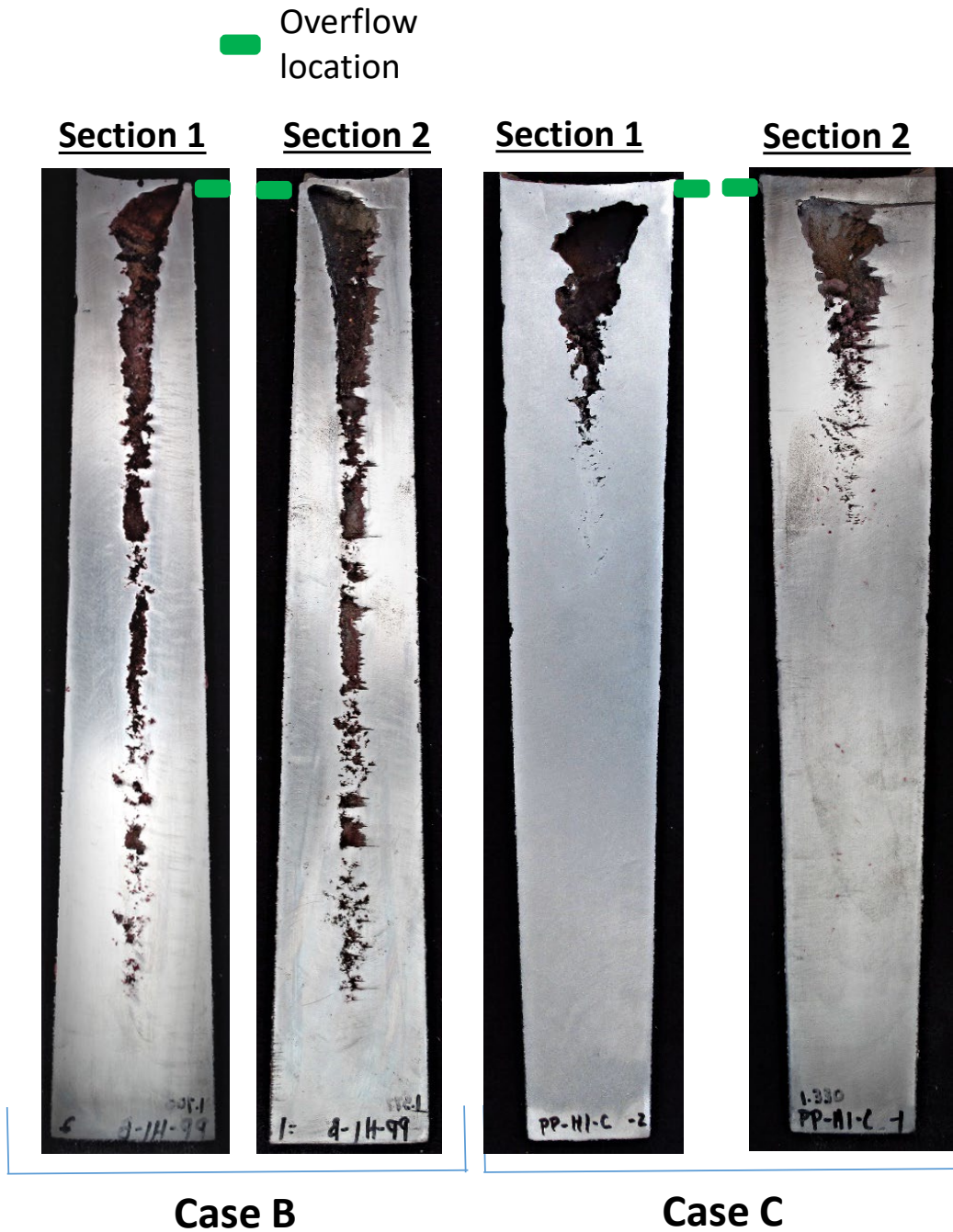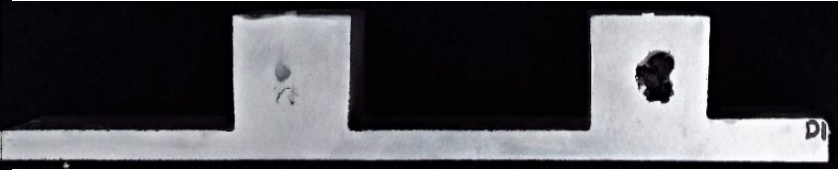
Figure 30. Porosity observed on the cross sections of the inverse-tapered and tapered cylinders from the heat 1 porosity experiments. Location of the overflow shown by green block. Again, there is a shell at the top of the casting surface and the centerline shrinkage porosity extending downward into the casting that is longer for the case B and much shorter for case C.
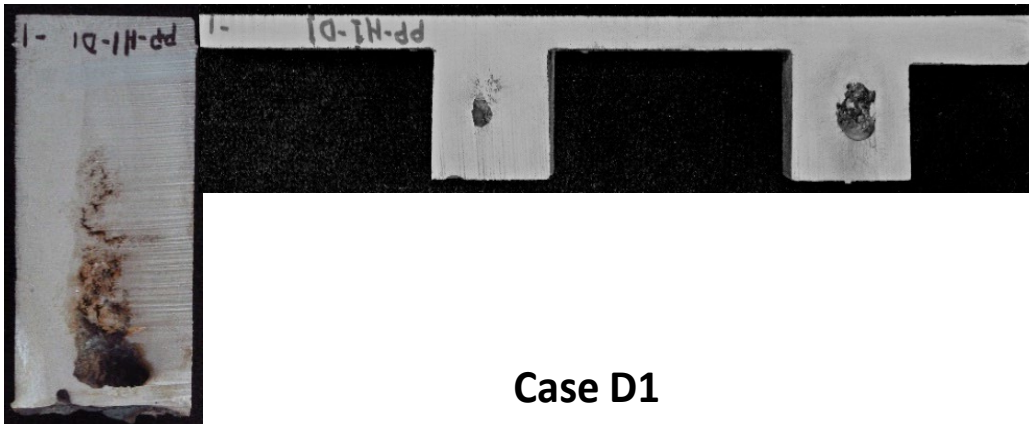
Section 1 Centerline

Section 1: 0.250 from Centerline

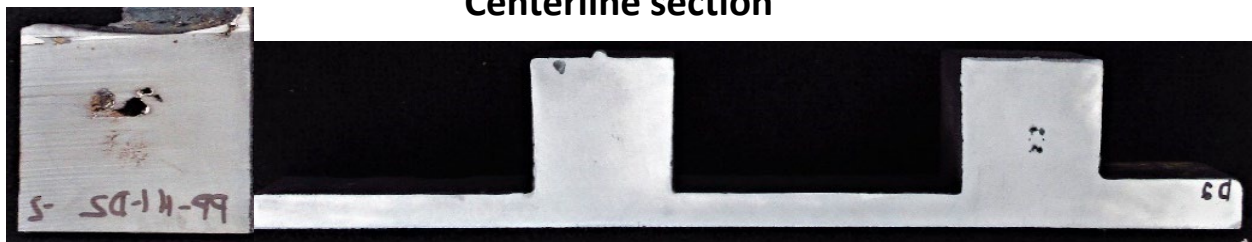**Section 2: 0.331" from centerline**

Section 2: 0.080" from centerline

Case D1

Figure 31. Porosity observed on the cross sections of the hot spot block casting D1 from the heat 1 porosity experiments. Several sections were made on each side of the mid-width plane.

Centerline section

Case D2

Figure 32. Porosity observed on the cross sections of the hot spot block casting D2 from the heat 1 porosity experiments. Casting was poured short due to an empty ladle.

Results for the Second Heat of Porosity Experiments

The six castings poured in the second heat of casting experiments are shown in Figure 33 with their pouring data. The pouring data are the casting volume and weight, pouring time, pouring stream angle, and pouring stream diameter. The simulations were performed using filling with this pouring data to model the experiments as accurately as possible. The pouring data were determined from videos taken by two cameras from different views.

The porosity observed on the cross sections of the castings are shown in Figure 34 for case A1, Figure 35 for case A2, Figure 36 through Figure 39 for case B, Figure 40 for case C1, Figure 41 for case C2, and Figure 42 for case D. The figures also indicate the inlet stream location entering the top of the castings relative to the ladle position and the overflow.

In Figure 34 and Figure 35 the porosity in four section views are shown for cases A1 and A2, respectively. These cases have a large central sprue/feeder and four spherical castings with two connected to branches off each side of the sprue. Note the thermocouple placement location in casting A2 as indicated in Figure 35. The spherical castings are connected at the mid-height of the sprue and the castings. The top of the sprue forms a shell as observed in the heat 1 experiments. There is surface sink at the top of the sprue as observed in the heat 1 experiments. The shrinkage pipe in the sprue extends past the connecting to the castings. In case A1 the shrinkage pipe is a little longer than case A2. Internal porosity forms in the spherical castings, and it is not centered in the spheres. The centroid location of the porosity is biased above the mid-height of the spheres. The shapes of the porosity regions are more ellipsoidal than spherical. The porosity regions do not have a riser pipe appearance. Upon close inspection of the porosity in the spheres, it is relatively smooth around its upper perimeter, and relatively dendritic around its lower surface. The upper part of the porosity region forms much earlier during solidification than the lower part.

Vertical sections of the porosity distribution for case B (the inverted V-shape) are shown on vertical sections A and B in Figure 36 and Figure 37, respectively. This case was designed to create a hot region at the mold-metal interface at the apex of the mold's inverted V-shape. This region was predicted to form surface sink, and surface sink in found as indicated in the figures. As found in all experiments, a solid shell with surface sink forms to the top of the casting. The porosity region below the shell is smooth around its upper surface so it formed early in solidification. Below the porosity region at the top of the casting, the steel is sound as this region was "fed" by the surface sink. Below this sound region with surface sink, internal porosity forms that has a dendritic appearance and the metal surface in that region has little or no surface sink. In Figure 38 and Figure 39 the regions of surface sink are filled in with modeling clay and shown with a scale in Figure 38 to document the surface sink dimensions. The largest depth of surface sink is about 4 mm (0.16"). In views C and D in Figure 38 and Figure 39 the regions of surface sink extend over nearly the entire front to back of the casting although the sink is progressively less deep toward the front and back faces. This case demonstrates how surface sink feeds the internal shrinkage of castings early in solidification.

In Figure 40 and Figure 41 porosity distributions on sections of the heat 2 experiment cases C2 and C1 are shown, respectively. These cases are cylindrical castings fed by blind risers connected at the castings' mid-height. Similarly, in Figure 42 the porosity distribution on cut sections for case D from the heat 2 experiments is shown. This case is a cylindrical casting fed by
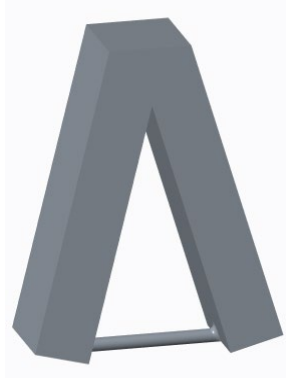
Cases A2:
4 spheres,
with thermocouple

TC
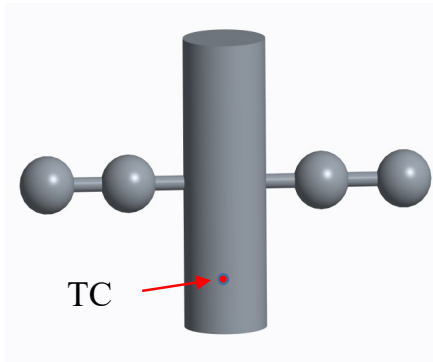
Pour Order: 1/6

Case A2:
Total volume: 88.2 in^3
Est. weight: 25 lbs.
Pour Time: 6.5 seconds
Pour angle: 60°
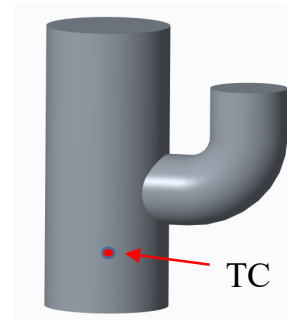Stream diameter: 0.7"

Case B:
Inverted V

2/6

Case B:
Total volume: 186.6 in^3
Est. Weight: 53 lbs.
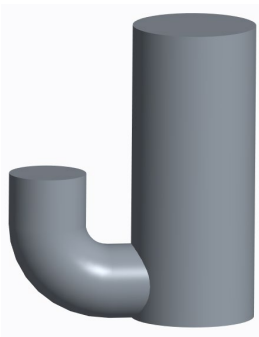Pour Time: 14 seconds
Pour angle: 52°
Stream diameter: 0.8"

Cases C2:
Blind riser, mid-height
with thermocouple

TC

3/6

Case C2:
Total volume: 153.5 in^3
Est. weight: 43.6 lbs.
Pour Time: 7.0 seconds
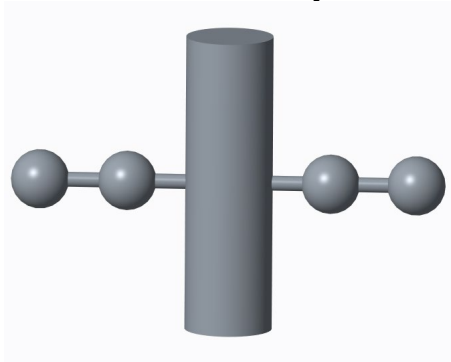Pour angle: 65°
Stream diameter: 0.75"

Case D:
Blind riser, bottom

Pour Order: 4/6

Case D:
Total volume: 153.5 in^3
Est. weight: 43.6 lbs.
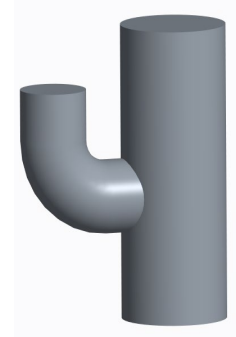Pour Time: 7.0 seconds
Pour angle: 60°
Stream diameter: 1.0"

Cases A1:
4 spheres,
no thermocouple

5/6

Case A1:
Total volume: 88.2 in^3
Est. weight: 25 lbs.
Pour Time: 5.0 seconds
Pour angle: 63°
Stream diameter: 1.0

Cases C1:
Blind Riser, mid-height
no thermocouple

6/6

Case C1:
Total volume: 153.5 in^3
Est. weight: 43.6 lbs.
Pour Time: 8.0 seconds
Pour angle: 69°
Stream diameter: 1.0"

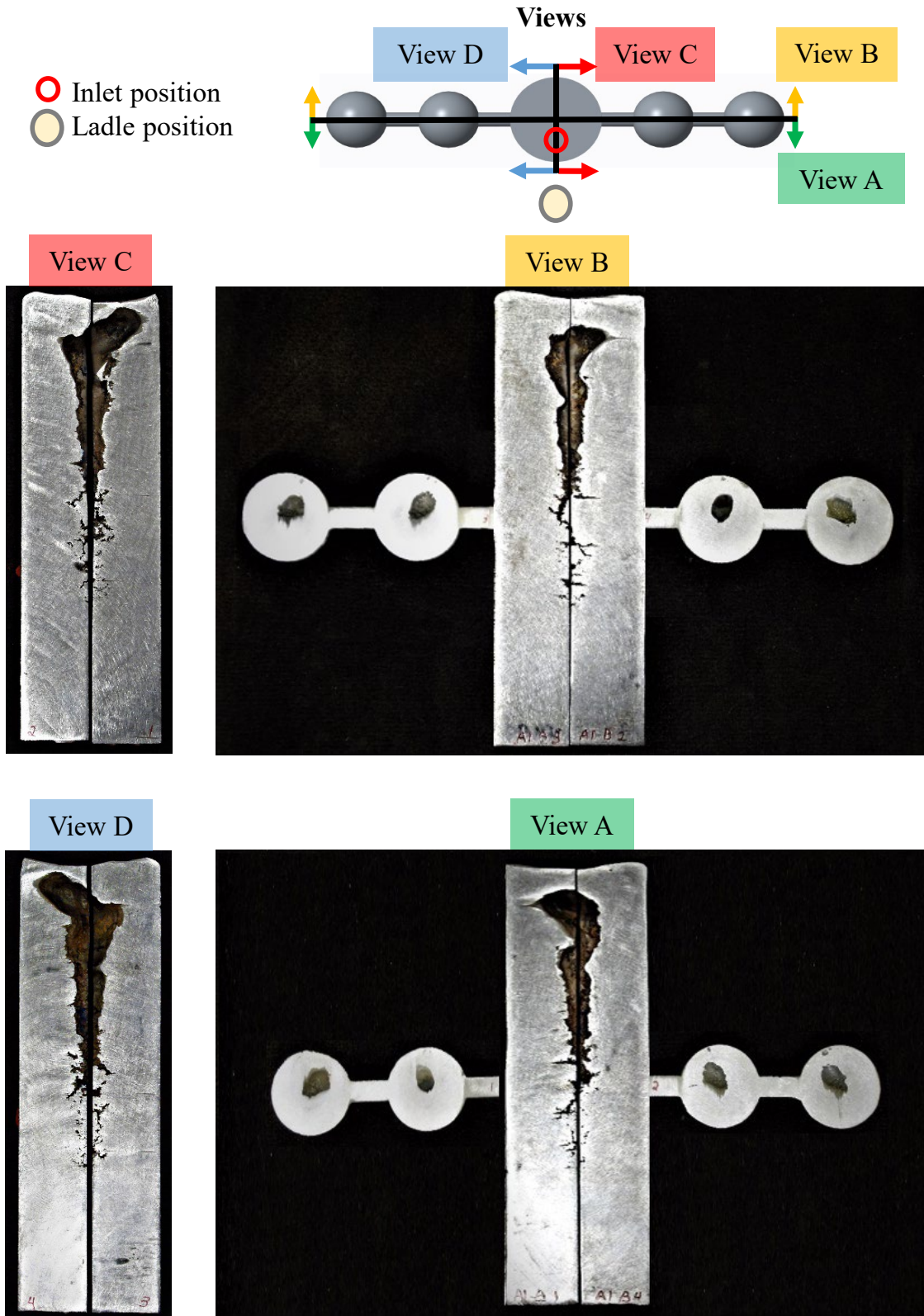Figure 33. Pouring data for the castings from heat 2 experiments.

Figure 34. Porosity observed on the cross sections of the spherical hot spot case A1 from the heat 2 porosity experiments. Location of the inlet stream into the top of the casting and ladle position is shown. The four section views A through D are defined in the top image.

Views

View D View C View B

○ Inlet position
○ Ladle position

View A
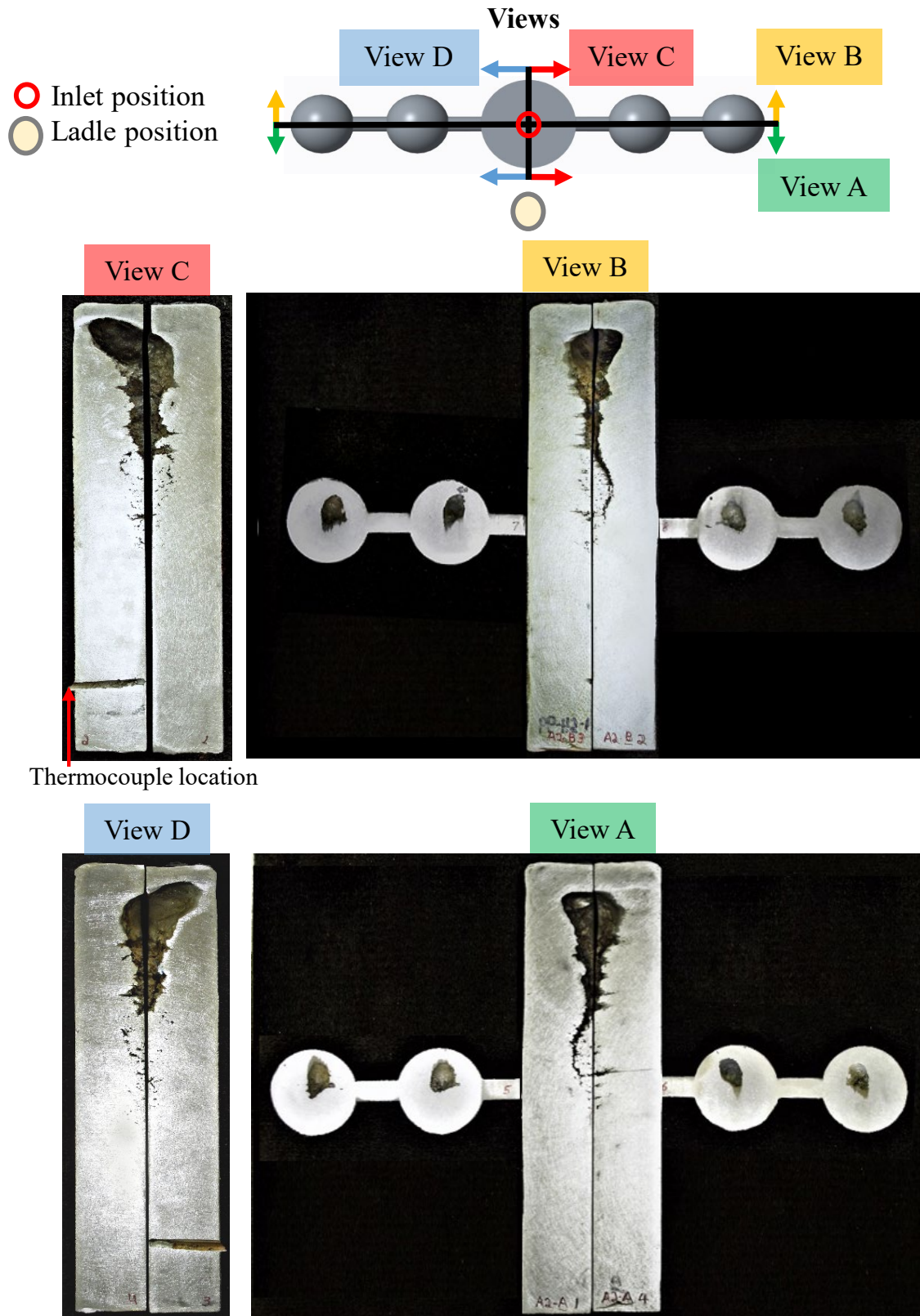
View C

View B

Thermocouple location

View D

View A

Figure 35. Porosity observed on the cross sections of the spherical hot spot case A2 from the heat 2 porosity experiments. Location of the inlet stream into the top of the casting and ladle position is shown. The four section views A through D are defined in the top image.
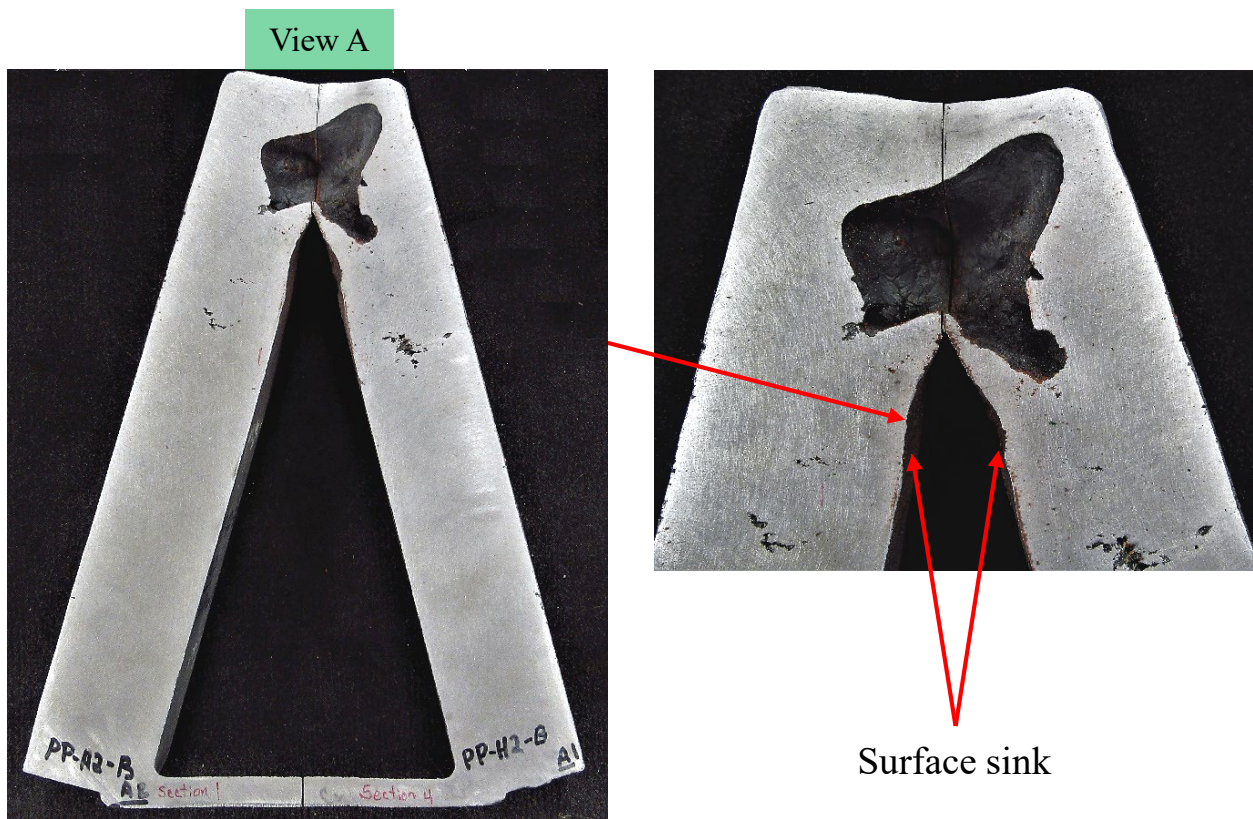
Figure 36. Porosity observed on cross section A of the inverted V-shaped casting case B from the heat 2 porosity experiments. Location of the inlet stream into the top of the casting and ladle position is shown. The four section views A through D are defined in the top image.
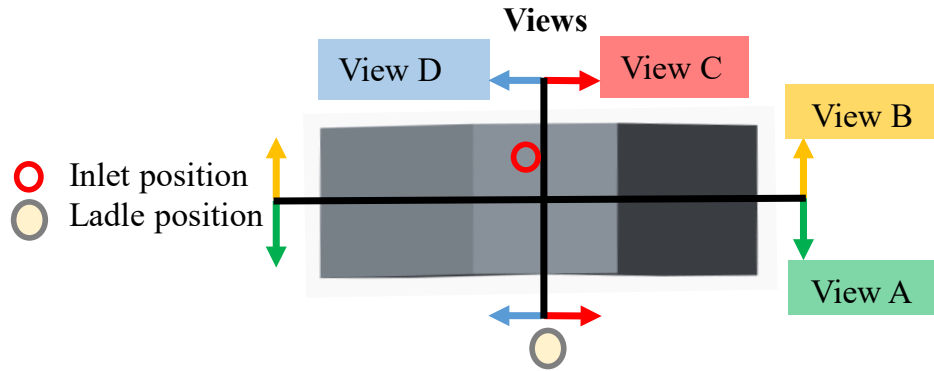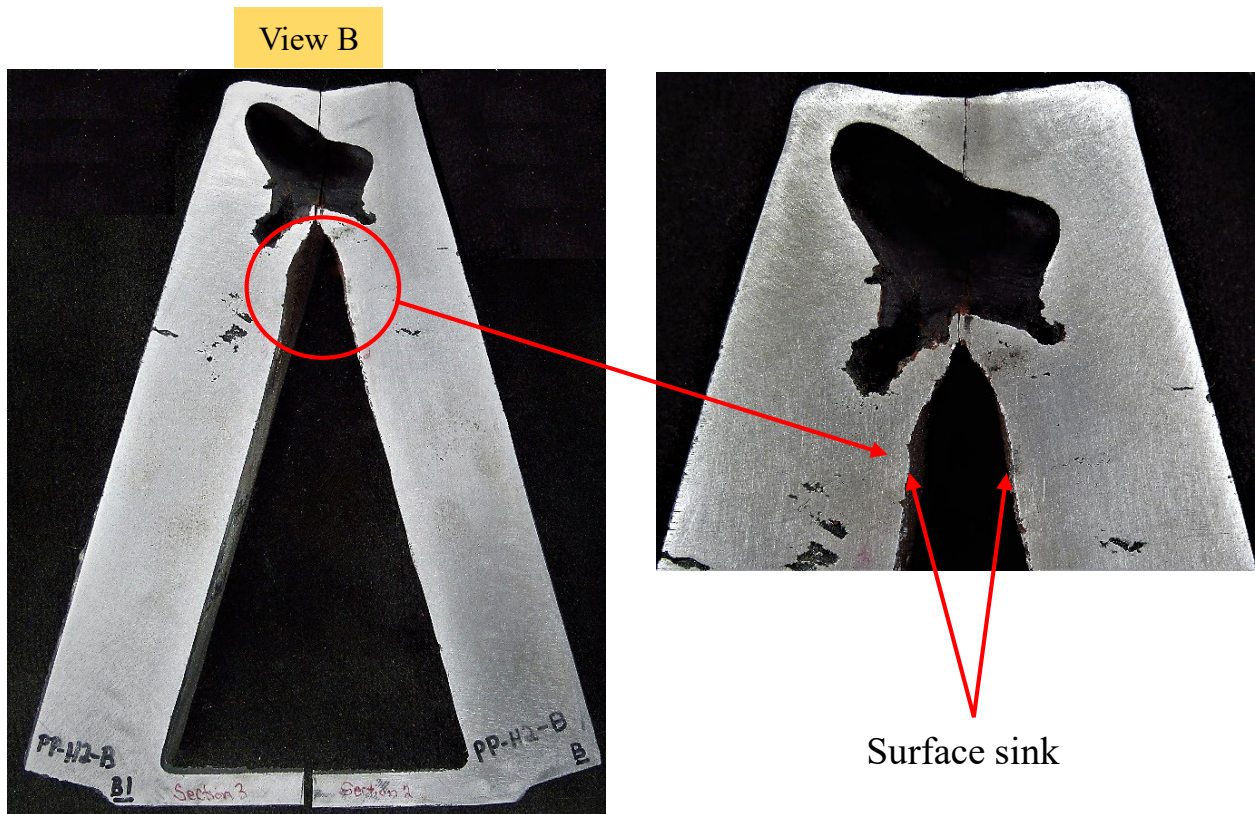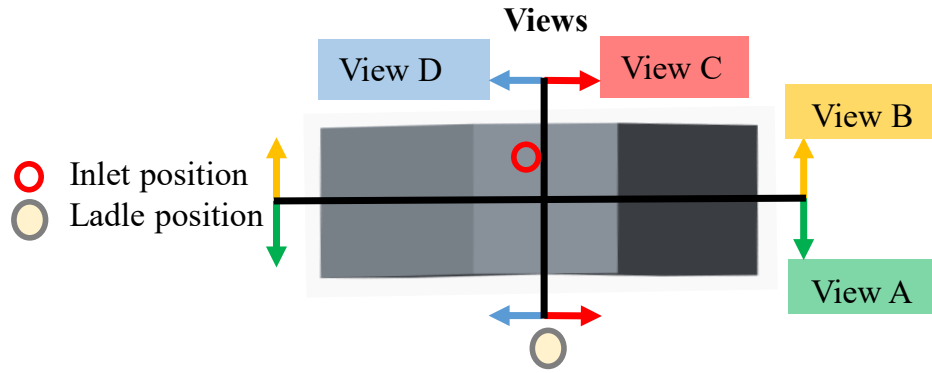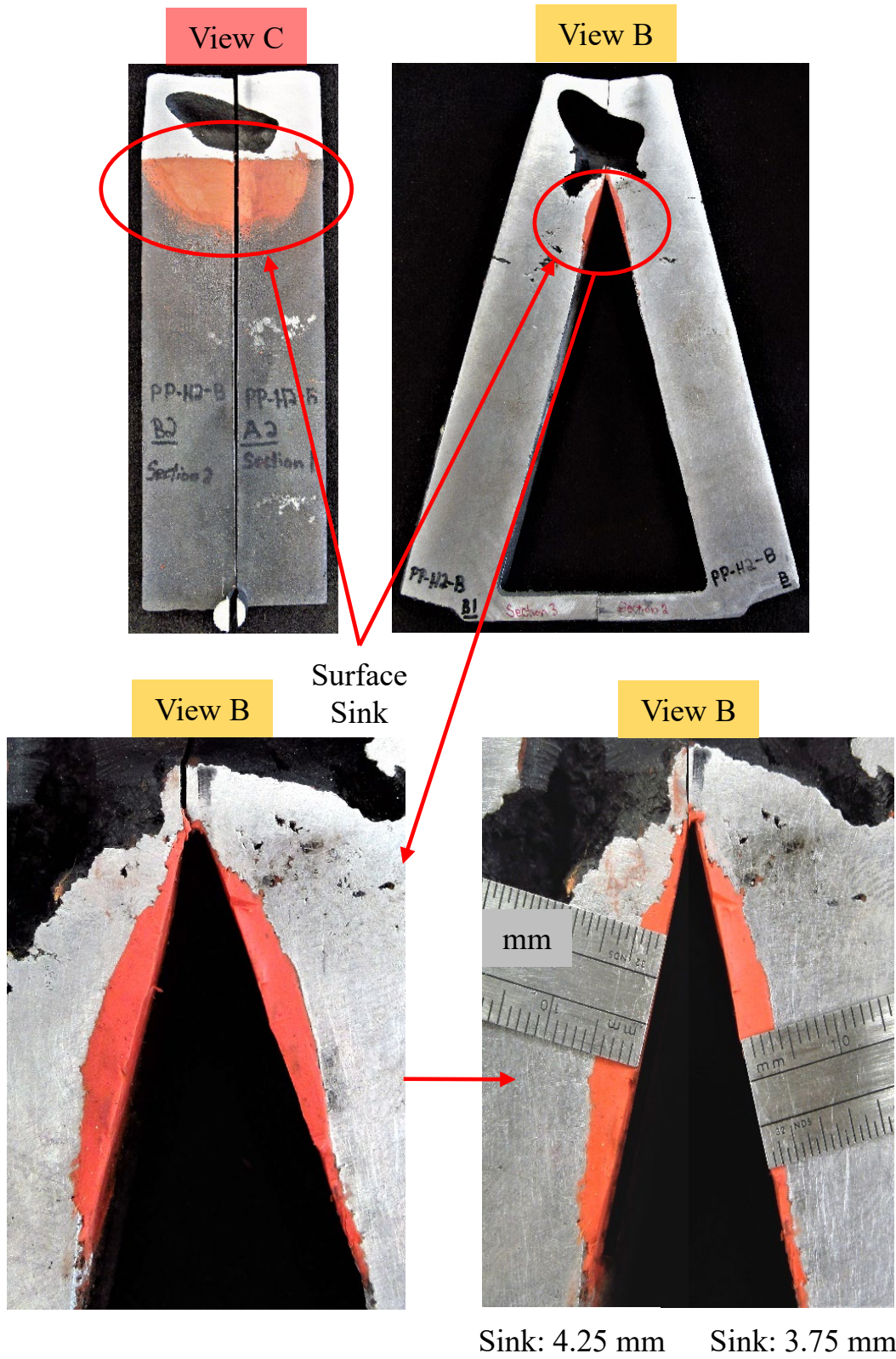
Figure 37. Porosity observed on cross section B of the inverted V-shaped casting case B from the heat 2 porosity experiments. Location of the inlet stream into the top of the casting and ladle position is shown. The four section views A through D are defined in the top image.

Figure 38. Porosity observed on cross sections B and C of the inverted V-shaped casting case B from the heat 2 porosity experiments. Dimensions of the casting surface sink at the mold-metal interface are indicated by the ruler for the clay filled surface.

View D

View A

Surface
Sink

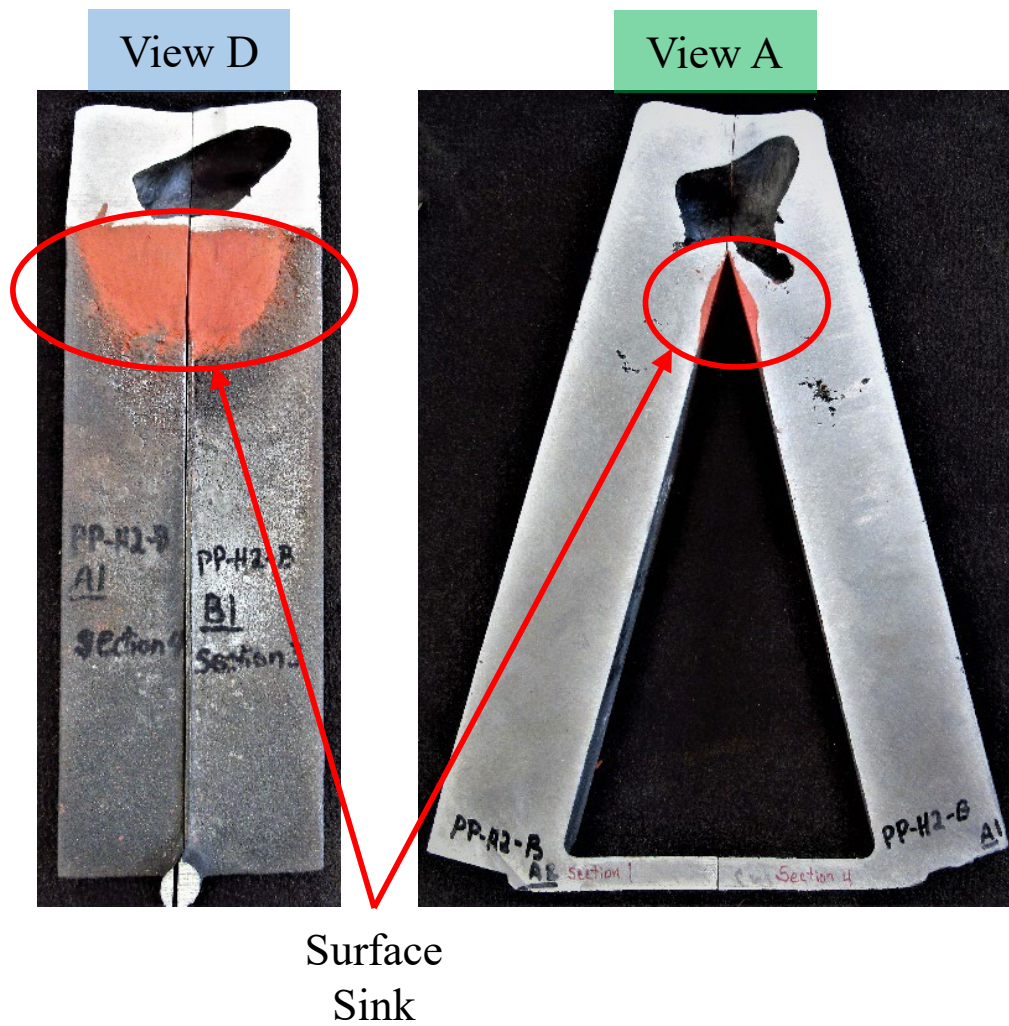Figure 39. Porosity observed on cross sections A and D of the inverted V-shaped casting case B from the heat 2 porosity experiments.

Figure 40. Porosity observed on the cross sections of the mid-height contact blind riser case C1 from the heat 2 porosity experiments. Location of the inlet stream into the top of the casting and ladle position is shown. The four section views A through D are defined in the top image.
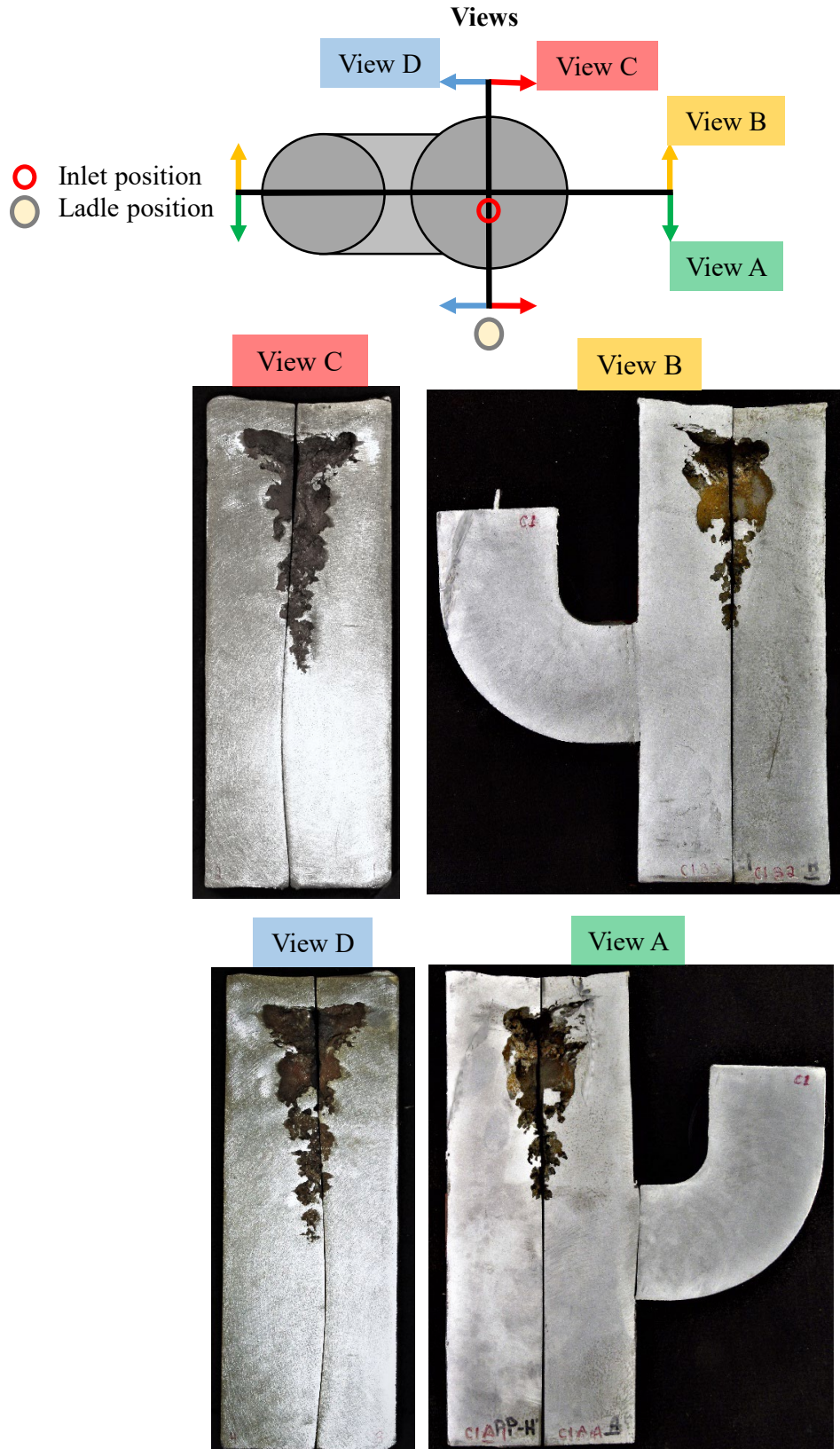
7

Figure 41. Porosity observed on the cross sections of the mid-height contact blind riser case C2 from the heat 2 porosity experiments. Location of the inlet stream into the top of the casting and ladle position is shown. The four section views A through D are defined in the top image.   50

Figure 42. Porosity observed on the cross sections of the bottom contact blind riser case D from the heat 2 porosity experiments. Location of the inlet stream into the top of the casting and ladle position is shown. The four section views A through D are defined in the top image.
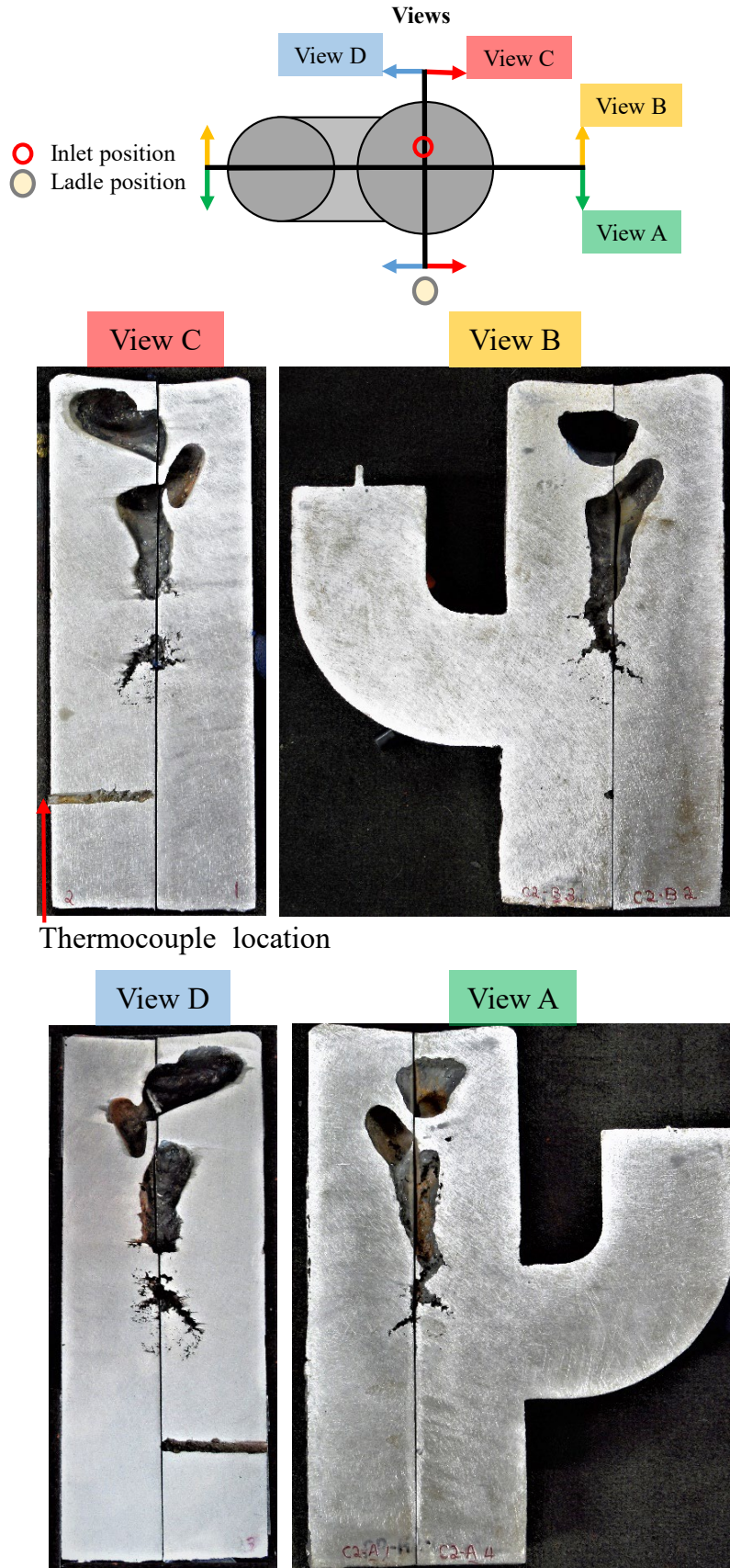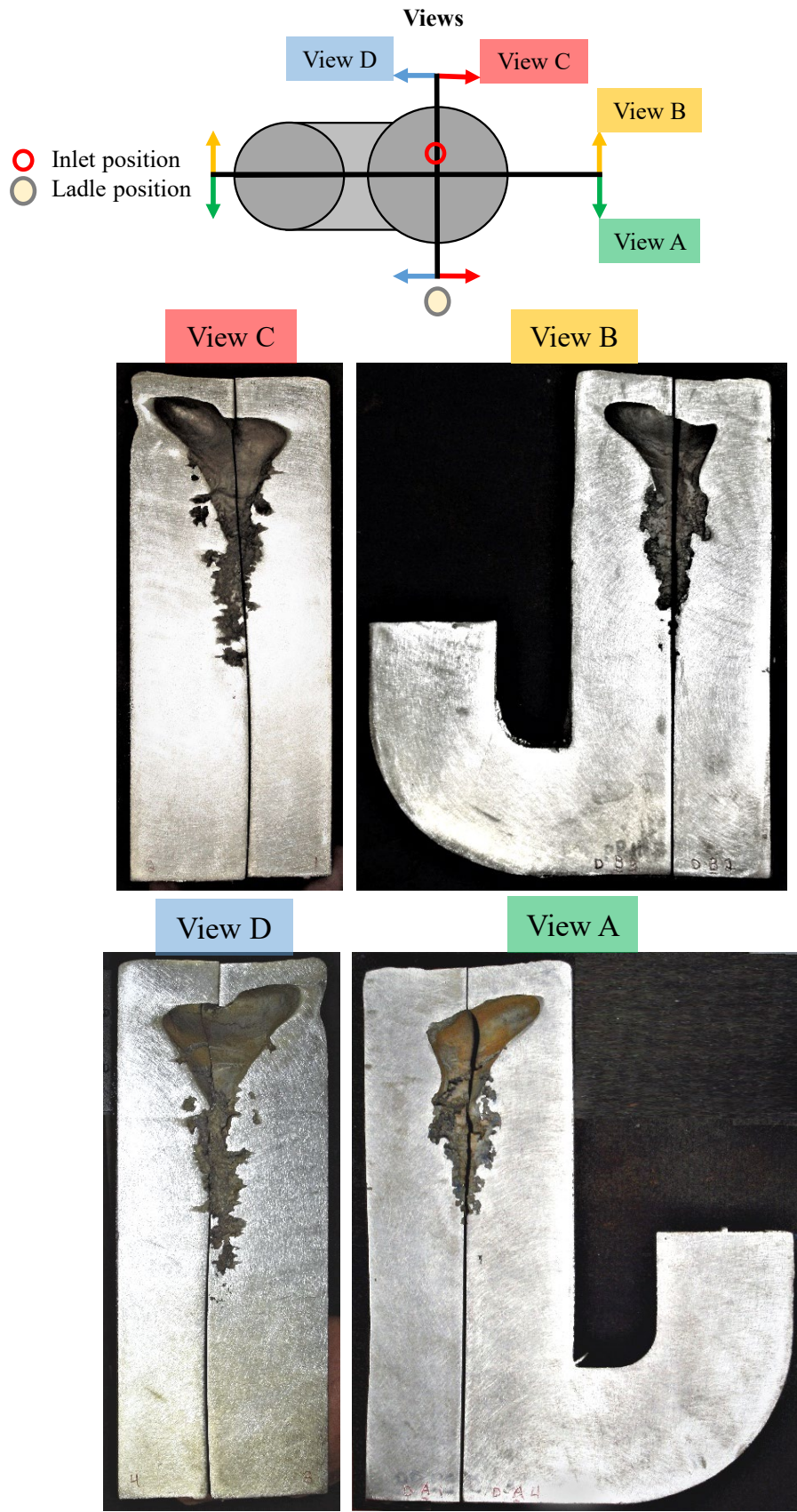
a blind riser connected at the casting's base. In all cases the porosity images show some surface sink and a shell forming at the top of the castings. In all these castings the blind riser features were sound, and the shrinkage porosity distributions in the castings all appear very similar. The depth of the porosity is about the same, and no difference was observed in the distributions. Casting C1 was poured last, and probably coldest. Castings C2 and D have a smooth upper surface to the shrinkage porosity distributions in the castings, and the casting C1 has a more dendritic appearance to the porosity on its upper surface.

3.3 Porosity Simulation Results

Results from the lengthy parametric study performed to determine the best advanced porosity model parameters will not be presented here. The parametric study involved varying model parameters until the best agreement between the experimental porosity distribution and the simulated one was obtained using the same parameters. The modeling parameters varied in the study were K_0, $g_{s,sur}$, $g_{s,coh}$, ε_{layer}, ε_{nuc}, and P_{mold}. The porosity distribution prediction results using these recommended modeling parameters will be presented here. The recommended modeling parameters determined from this study are given in Table 1. The results for the cases presented here use a pouring temperature of 1514 °C. The other pouring simulation conditions were given in the "Porosity Experiment Results" section of this paper. Porosity distribution results from the simulations using the advanced shrinkage porosity model will be compared to results from a commercial software's "standard" shrinkage porosity model using the same modeling conditions. The simulation software used for all cases is *MAGMAsoft* [7]. The simulations used a feature of the software to remove the influence of the inlet at the end of filling by moving the inlet approximately 1" above the top of the casting. Then the casting height was also increased by the same height increase as the inlet, and the casting was only filled to the actual casting height using the software's "stop condition" feature. Without doing this, the inlet was found to create a hot zone on the top surface of the casting where porosity always nucleates, making the formation of the observed shell at the top of the casting. Currently the software does not have the capability to model convection during solidification using the advanced porosity model. If convection were to be modeled using the advanced porosity model, the raising of the inlet height and use of the "stop condition" would probably not be needed. That is a topic for future work.

Simulation Results for the First Heat of Porosity Experiments

The porosity distributions for the five cylindrically shaped casting experiments performed in heat 1 are compared to the porosity simulation results in Figure 43 to Figure 45. Simulation porosity results at the casting midsections are being compared to observed porosity on the casting sections for the straight, tapered, and inverse tapered cylinder experiments.

In Figure 43(a) the three straight cylinder porosity experiments are shown that have been sectioned longitudinally at mid-point of the overflow. In Figure 43(b) the simulated porosity distributions using the advanced model (right side) and the standard software model currently used in the software are shown on the same section as the experiments. The advanced shrinkage porosity feeding predicts a shell is predicted over the top of casting, and the length and appearance of the shrinkage pipe is in good agreement. Surface sink at the top of the casting is predicted for the

advanced model. The advanced porosity model's distribution has shrinkage pipe extending over 3/4th of the cylinder height like the experiments. The standard model has the same length of shrinkage pipe, if not longer. The advanced model's shrinkage pipe is wider than the standard model in better agreement with the experiments. The standard model has poor agreement with the experiments at the top of the casting, and it has no shell or surface sink (only a shrinkage pipe). The advanced model is an improvement over the standard one.

In Figure 44(a) the inverse tapered cylinder porosity experiment is shown sectioned longitudinally at mid-point of the overflow. The experiment porosity distribution has some surface sink and a solid shell on top with shrinkage pipe extending over nearly 90% of the cylinder height. In Figure 44(b) simulated porosity distributions using the advanced model (right side) and the standard software model currently used in the software are shown on the same section as the inverse tapered experiment. The advanced feeding model results using the new software features predicts the observed shell at the top of the casting, and the length and appearance of the shrinkage pipe is in good agreement with the experiments. The standard model has poor agreement with the experiments with no shell and the predicted shrinkage piping is the about the same length as the experiment and the advanced model. The observed and predicted piping is continuous along the inverse tapered cylinder's length. The advanced porosity model shrinkage pipe is wider than the standard model's in better agreement with the experiment. No surface sink is predicted by the standard model, and only a small surface sink is predicted in the advanced model. The experiment has more surface sink than the advanced model prediction.

In Figure 45(a) the tapered cylinder porosity experiment is shown sectioned longitudinally at mid-point of the overflow. The experiment porosity distribution has some surface sink and a solid shell on top with shrinkage pipe extending more than the upper 25% of the cylinder height. In Figure 45(b) the simulated porosity distributions using the advanced model (right side) and the standard software model (left side) are shown on the same section as the tapered casting experiment. The advanced feeding model results predict the observed shell at the top of the casting. The appearance of the advanced model's shrinkage pipe is in good agreement with the experiments, but not as long as the experiment. The standard model porosity distribution has no solid shell, and its shrinkage pipe is shorter than the advanced model and the experiment.

In Figure 46(a) the hot spot block porosity experiment is shown sectioned longitudinally at mid-width of the casting. The experiment porosity distribution has surface sink and a solid shell on top of the feeder with a shrinkage pipe extending over two-thirds of the feeder height. In Figure 46 (b) the simulated porosity distributions using the advanced model (bottom image) and the standard software model (top image) are shown on the same section as the hot spot casting experiment. The advanced feeding model results predict the observed shell at the top of the feeder and the piping length is like the observation. The appearance of the advanced model's internal hot spot porosity is in good agreement with the experiments. This internal porosity has a spheroidal shape and is centered in the blocks with higher porosity predicted in the block near the casting/plate end. This appearance closely resembles the experiment observations. On the other hand, the standard porosity model predicts mini riser pipes in the blocks that extend nearly to their top surface, unlike the experimentally observed porosity. Even though the agreement using the

advanced model is good, to achieve these results the mold pressure was defined using a local mold pressure of 0.2 bar around the hot spot blocks to suppress the nucleation of porosity at the corners of the blocks. Investigating this need to modify the mold pressure to obtain more realistic model results is recommended for future work.

Table 1. Properties and model parameters used in advanced shrinkage porosity simulations.

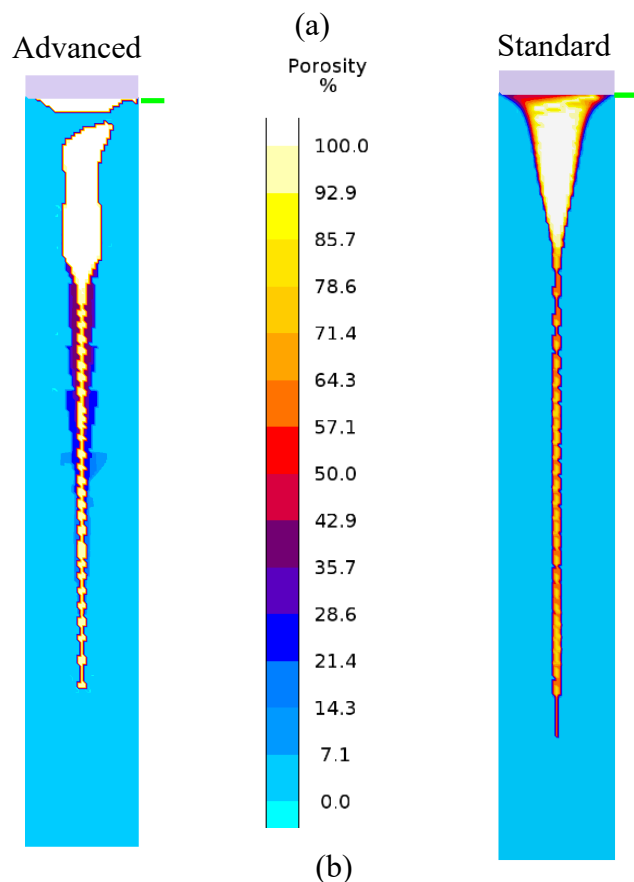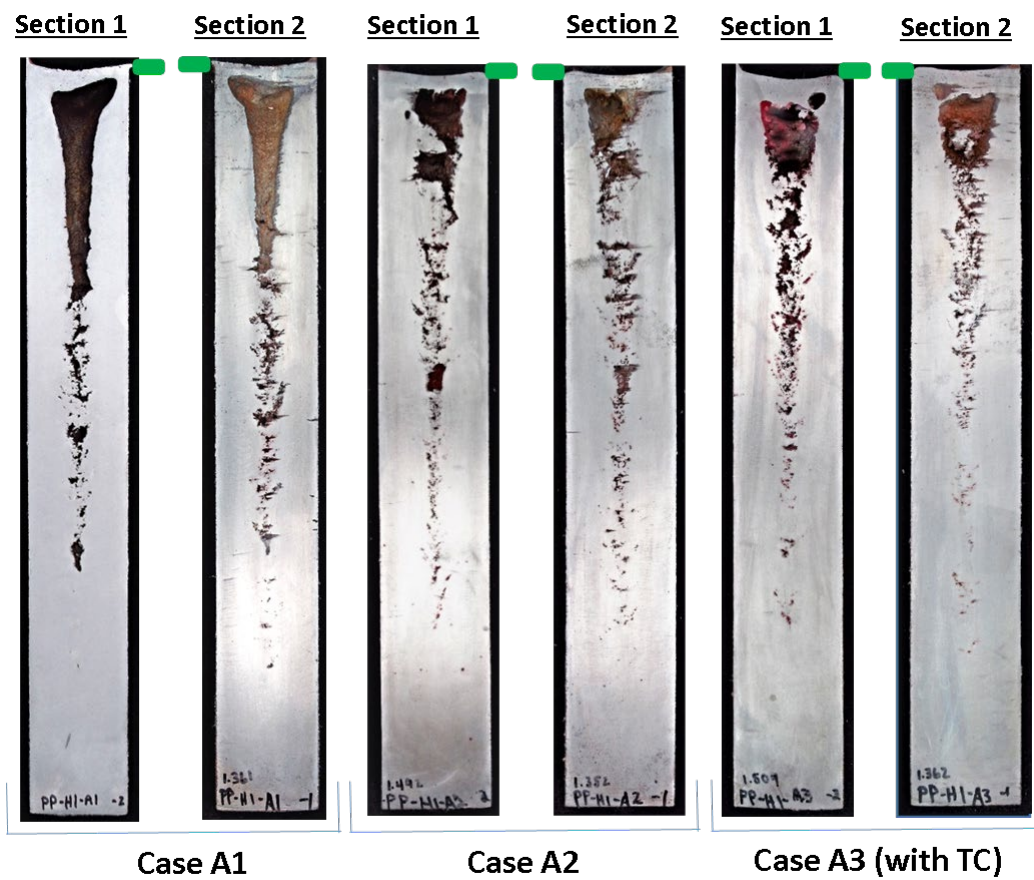| Parameter (units)	Value
$K_0 \, (\text{m}^2)$	1.7×10^{-9}
$K_{min} \, (\text{m}^2)$	1×10^{-16}
$K_{max} \, (\text{m}^2)$	1×10^{-6}
$g_{s,sur} \, (\text{-})$	0.55
$g_{s,coh} \, (\text{-})$	0.55
$\varepsilon_{layer} \, (\text{-})$	3.5×10^{-2}
$\varepsilon_{nuc} \, (\text{-})$	1×10^{-3}
$P_{atm} \, (\text{bar})$	1.01325
$P_{\sigma,0} \, (\text{bar})$	P_{atm}
$P_{mold} \, (\text{bar})$	P_{atm}
$\rho_{solid} \, (\text{kg/m}^3)$	7280.3
$\rho_{liquid} \, (\text{kg/m}^3)$	6993.0
$\mu_\ell \, (\text{Pa.s})$	5.63×10^{-3}

Figure 43. (a) Views of observed porosity on heat 1 experiment castings A1, A2 and A3, and (b) porosity results from simulations on a scale from 0 to 100%. Simulation results show the advanced feeding model and the standard porosity model.
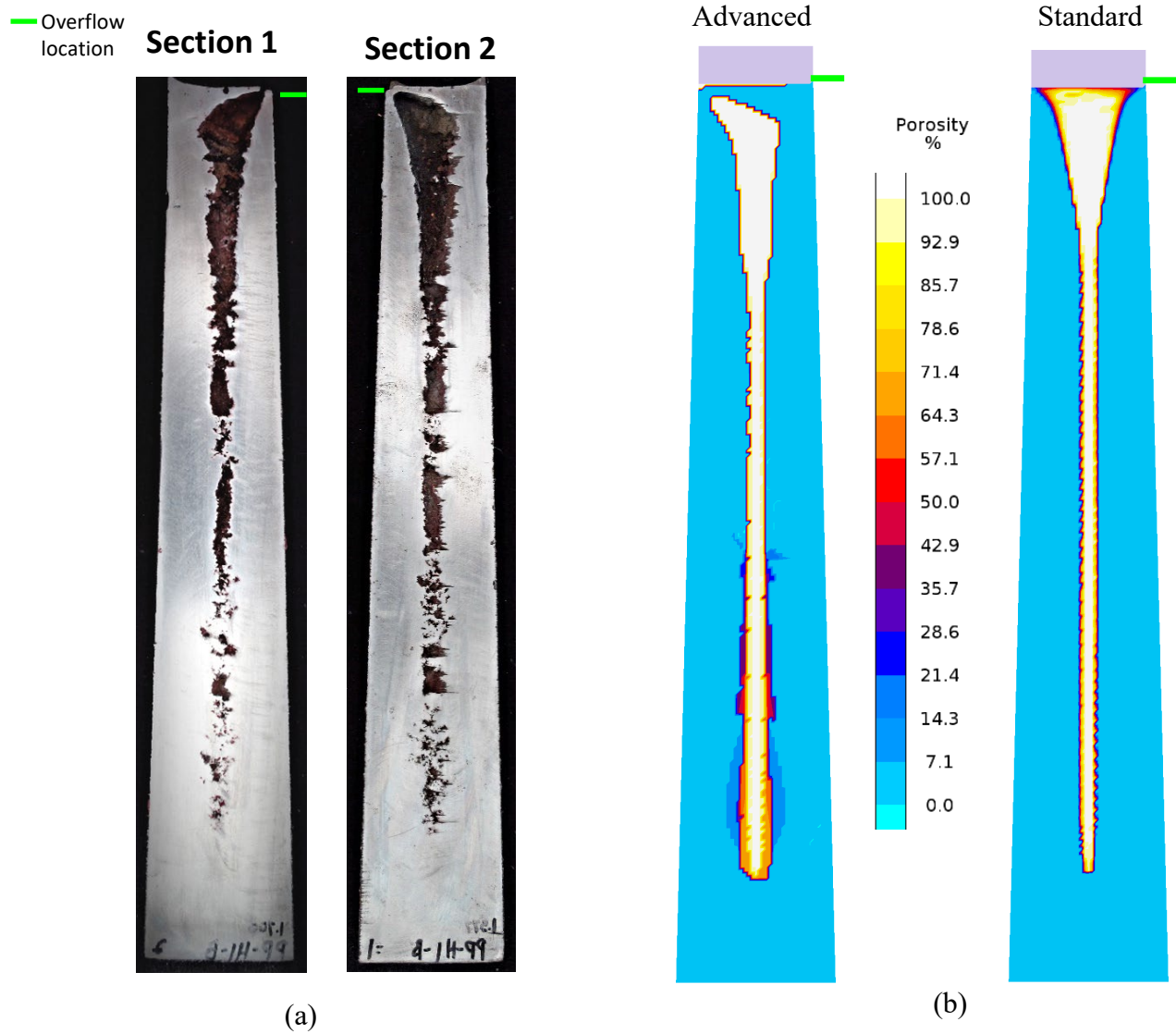
Figure 44 Simulation porosity results (a) and observed porosity (b) on sections of an inverse tapered cylinder casting. Simulation results show the new advanced feeding model developed in this research program and the standard porosity model currently available in the casting simulation software *MAGMAsoft*.
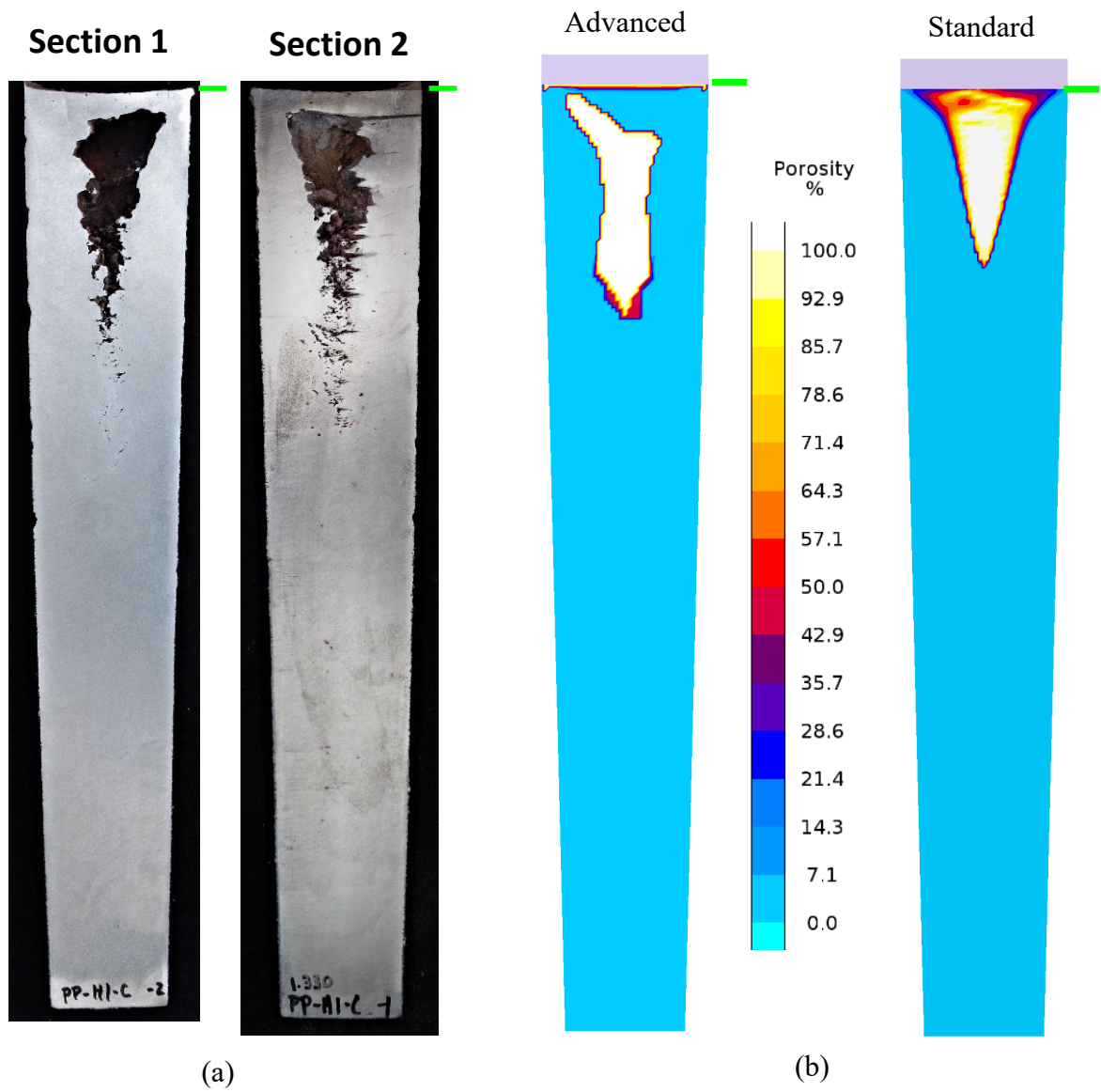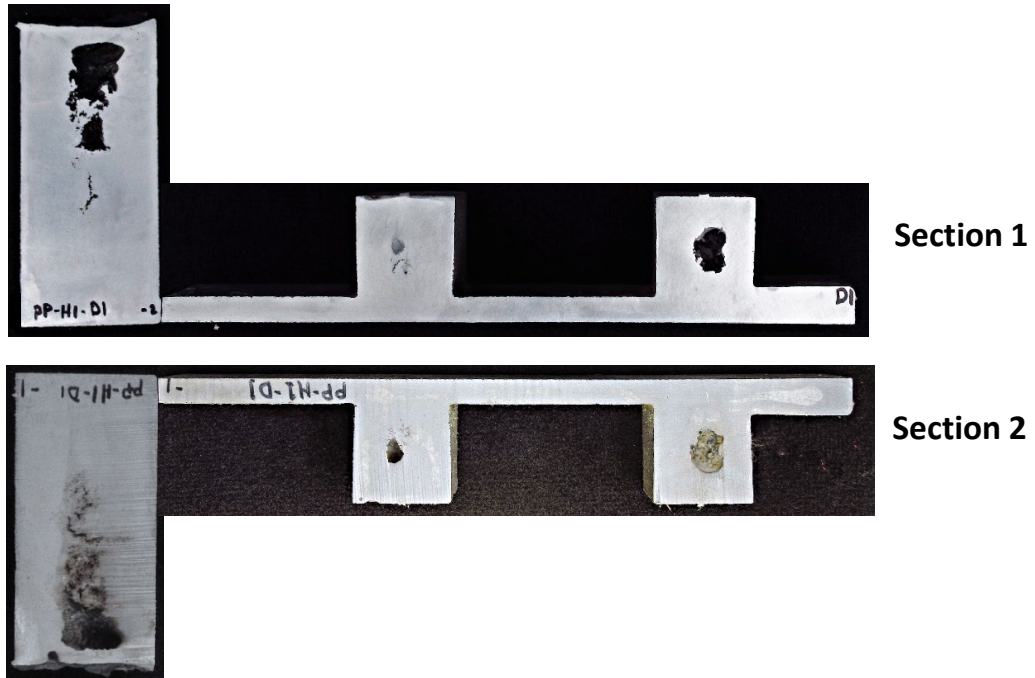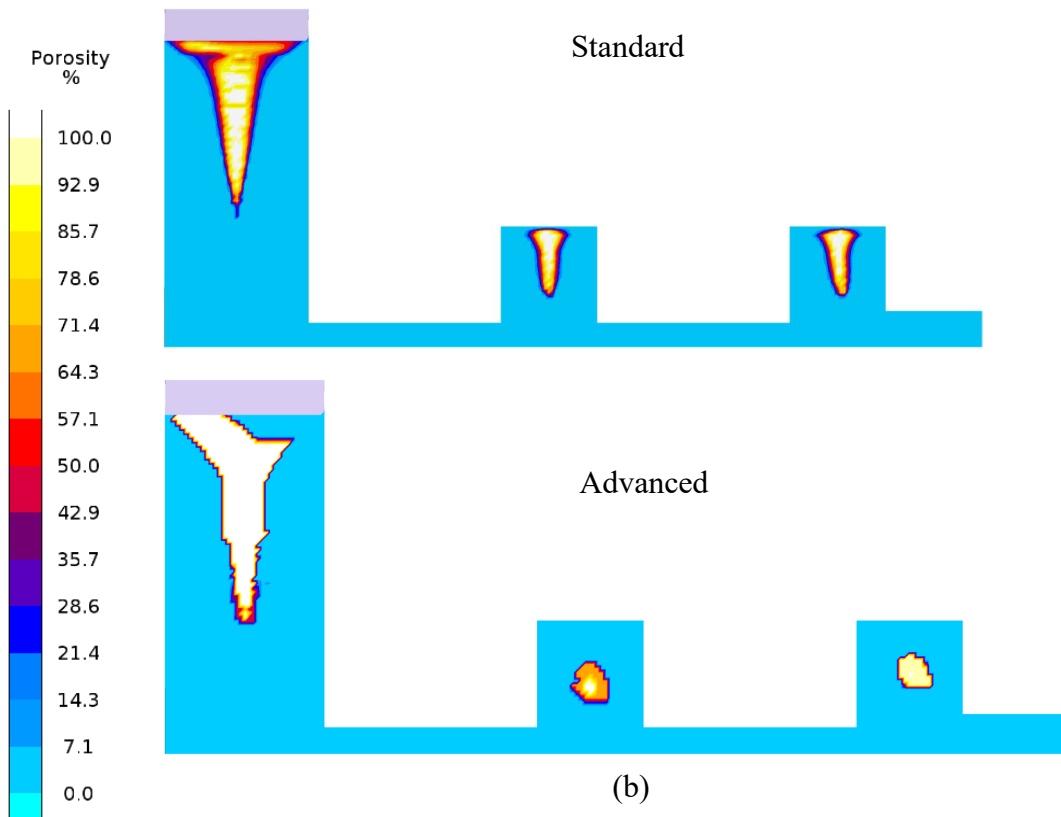
Figure 45 Observed porosity results (a) and simulated porosity (b) on sections of the tapered cylinder casting. Simulation results show the new advanced feeding model developed in this research program and the standard currently available porosity model.

(a)

(b)

Figure 46 Simulation porosity results (a) and observed porosity (b) on sections of the hot spot block casting. Simulation results show the new advanced feeding model developed in this research program and the standard currently available porosity model.

Simulation Results for the Second Heat of Porosity Experiments

The experimentally observed porosity distributions for the casting experiments performed in heat 2 are compared to the porosity simulation results in Figure 47 to Figure 50. These cases are the casting with four spheres filled through a central feeder, the inverted V-shaped casting, and the two blind riser castings, one with the riser contact at mid-height and the other with a contact at the base.

In Figure 47(a) the porosity experiment with the four spherical hot spot castings is shown sectioned vertically. The experiment porosity distribution has some surface sink and a solid shell on top with shrinkage pipe extending over two thirds of the feeder height. In Figure 47(b) the simulated porosity distributions using the standard software model (top image) and the advanced model (bottom image) are shown on the same section as the casting experiment. The advanced feeding model results predict the observed shell over most of the top of the feeder and the piping length is like the experiment. The appearance of the advanced model's internal hot spot porosity is in good agreement with the experiments. This internal porosity has a spheroidal shape and is internal in the spheres with their centers slightly above the spheres mid-height. This appearance closely resembles the experiment observations. Again, like the hot spot blocks, the standard porosity model predicts mini riser pipes in the spheres that extend nearly to their top surface and does not resemble the experiment. Neither simulation predicts the surface sink observed in the experiments.

In Figure 48(a) the porosity experiment with the inverted V-shaped casting is shown sectioned vertically with two views. The experiment porosity distribution has surface sink at the top and apex of the V, and a solid shell on top. The internal shrinkage in the experiment does not look like a riser pipe. In Figure 48(b) the simulated porosity distribution predicted using the advanced model is shown on the same section as the casting experiment. The advanced feeding model results predict the observed shell over the top of the casting. The internal porosity is like the experiment. The simulation does not predict any surface sink at the top of the casting as observed in the experiment, but some surface or near surface sink is predicted at the apex of the V as seen in the experiment.

In Figure 49 and Figure 50 the experimental and porosity distributions predicted using the advanced model for the blind riser cases C1, C2 and D are shown. These have agreement in that no porosity is forms in the blind risers. The shrinkage pipes appear similar in the experiments and the predictions. The solid shell at the top of the experiments is partly predicted, but no surface sink that appears at the top of the experiment castings is predicted. This is because of a hot zone at the top of the castings that nucleates porosity preventing surface sinks from forming.
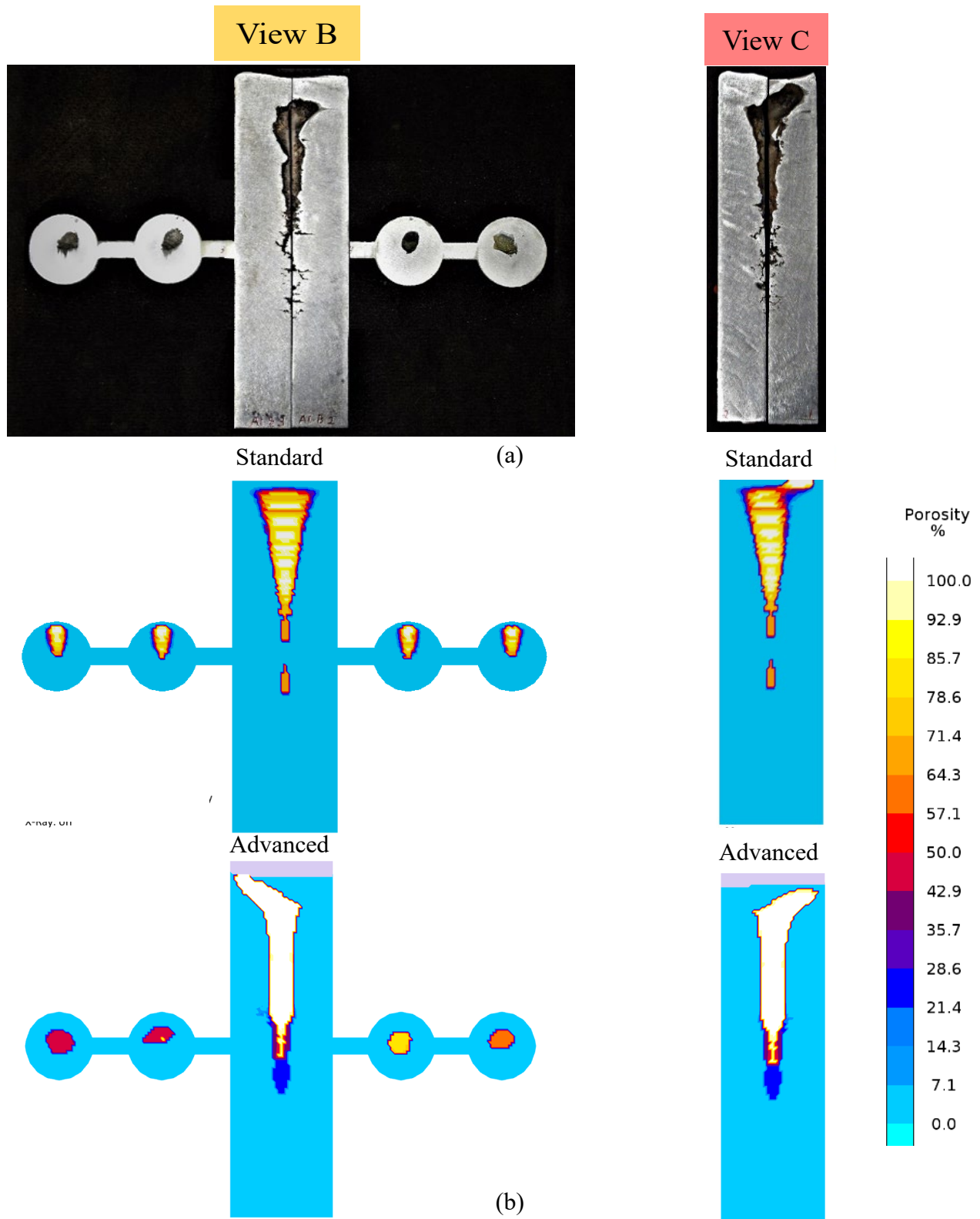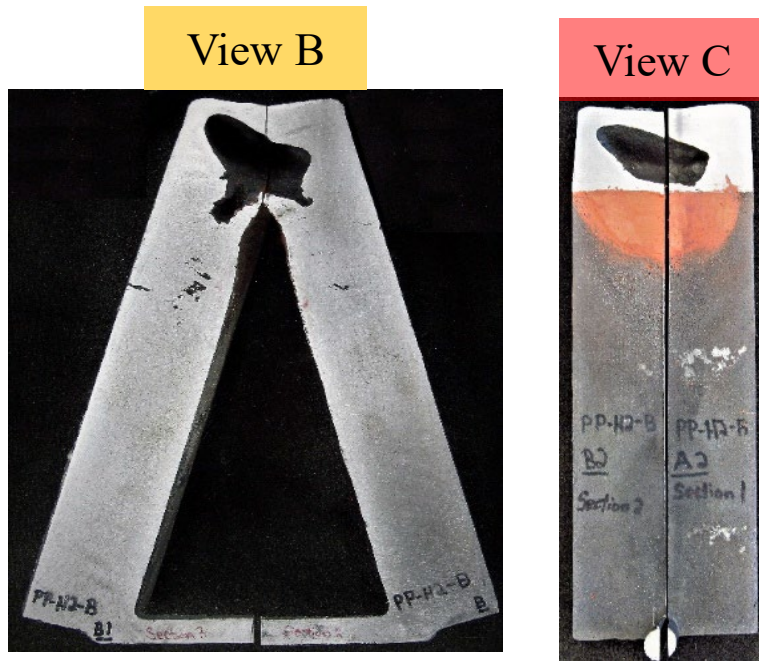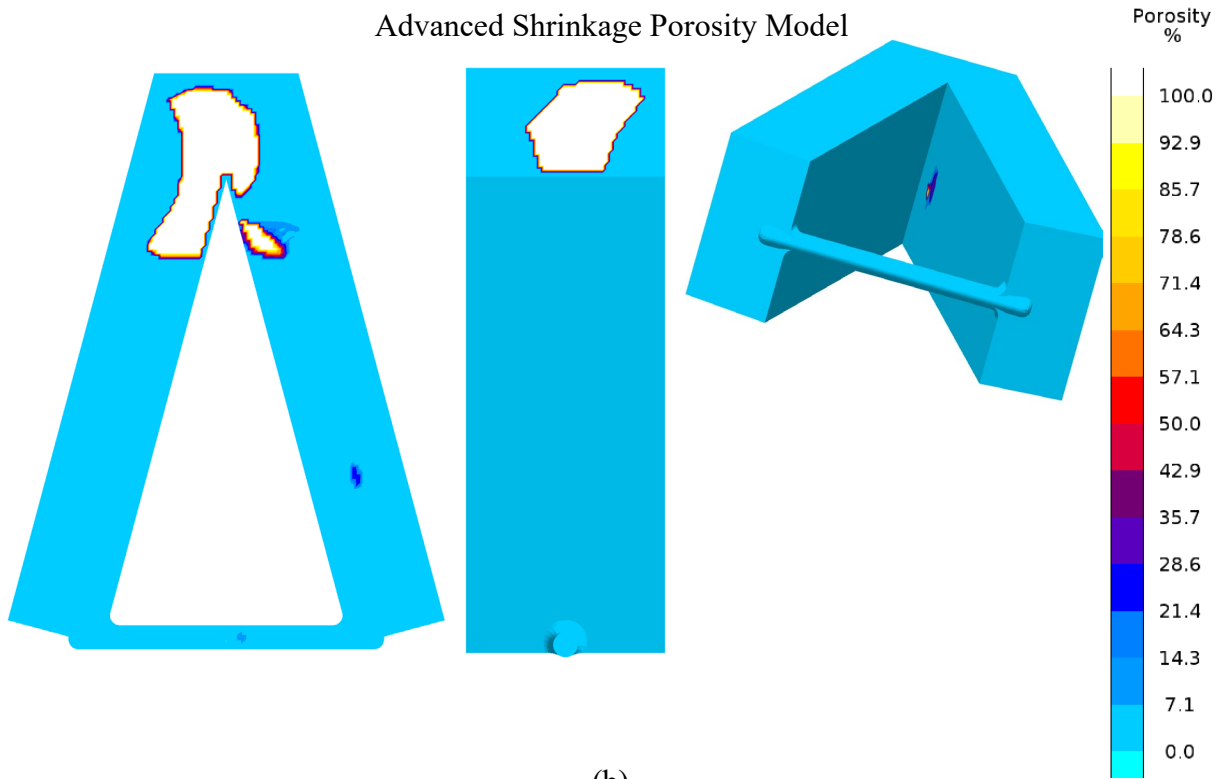
Figure 47 At the top of (a) is a diagram of the section views (B and C) for the casting experiment case with four spheres and in the lower part of (a) the observed porosity on the section veiws. Simulation porosity results are shown in (b) for the standard feeding and new advanced feeding model.

y

(a)

(b)

Figure 48 At the top of (a) is a diagram of the section views (B and C) for the inverted V-shaped casting from the second heat of porosity experiments. Simulation porosity results are shown in (b) for the advanced shrinkage porosity model.

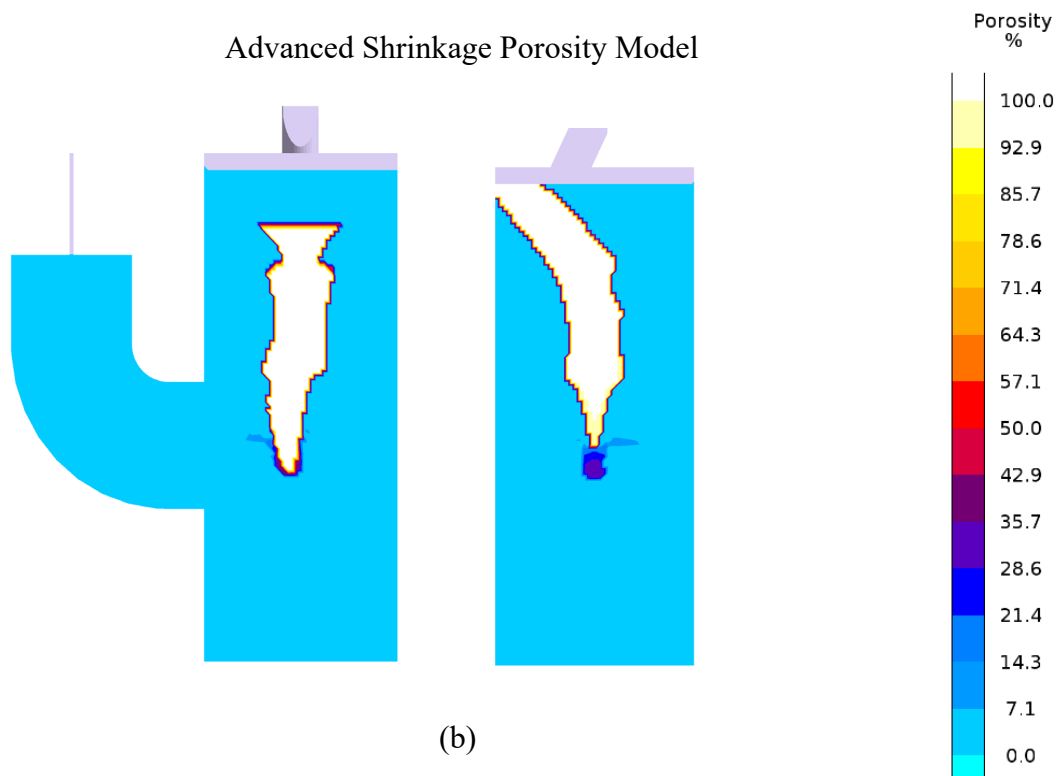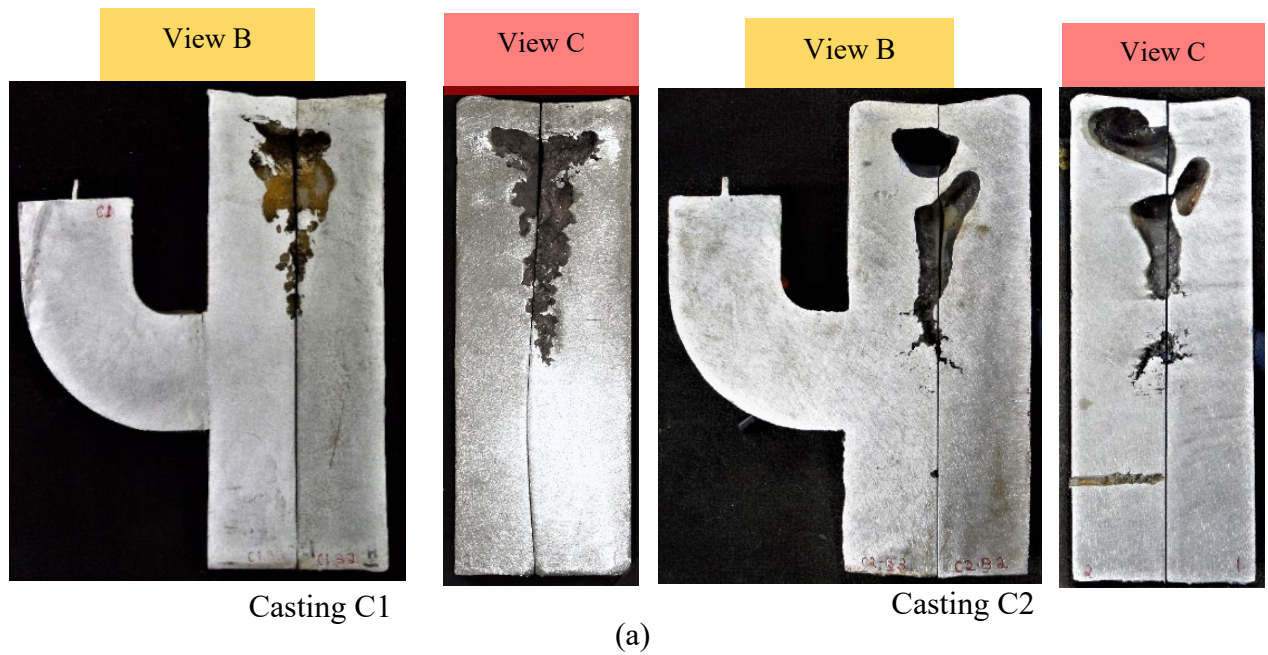Casting C1   Casting C2

(a)

(b)

Figure 49. (a) Cross sections of castings C1 and C2 with blind risers connected at the casting mid-height from the second heat of porosity experiments. (b) Advanced porosity model results on the same cross sections as the observed porosity in (a).
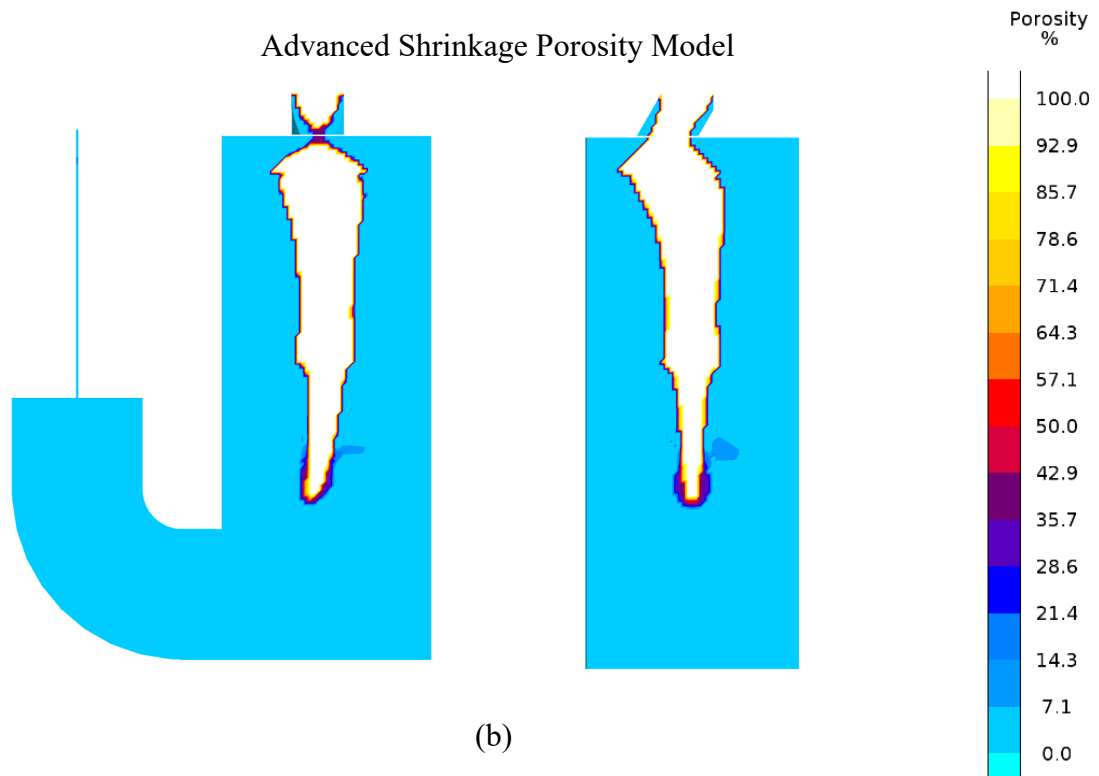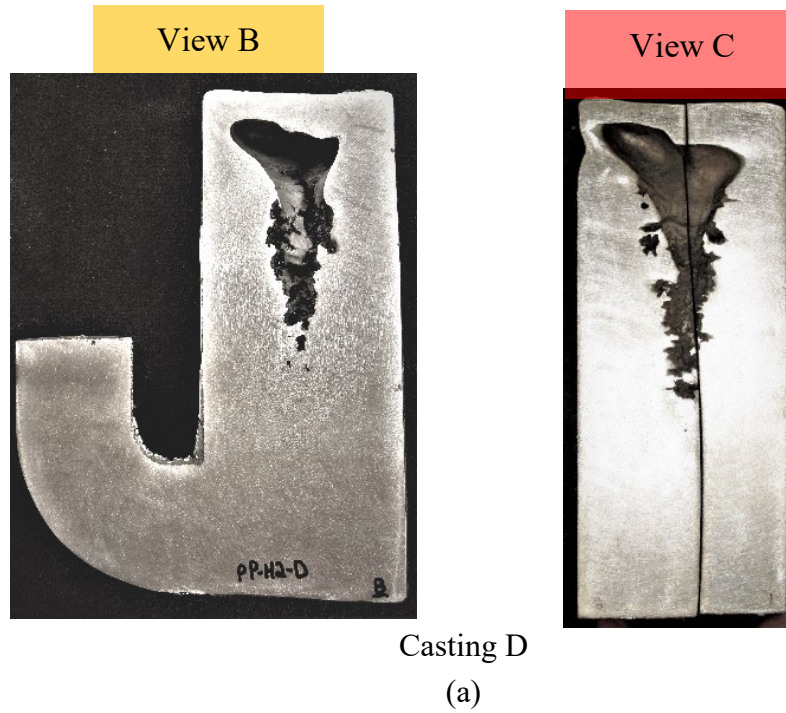
Casting D

(a)

(b)

Figure 50. (a) Cross sections of casting D with blind risers connected at the casting base from the second heat of porosity experiments. (b) Advanced porosity model results on the same cross sections as the observed porosity in (a).

4. Conclusions

An advanced simulation model for predicting shrinkage porosity in steel castings is presented and compared to two heats of casting experiments. Demonstrating the more realistic predictions from the advanced model and improvement over a standard model currently available in commercial software, the model has been validated. The advanced model calculates the pressure field and feeding flows associated with the formation of shrinkage porosity. The advanced model requires no feeding effectivity, which is used in the standard porosity model. Finally, the advanced model also accounts for the entire solidification shrinkage of the steel, which the current model using feeding effectivity does not.

Two sets of casting experiments were designed to produce varying levels of shrinkage piping and centerline, surface, and hot spot shrinkage porosity. The results from the experiments by themselves are novel and of interest to the steel casting community. It was impossible to find published work documenting in detail such experiments generating this spectrum of porosity formation mechanisms for use in validating the model. In the first set of experiments, straight cylinders, tapered cylinders, and rectangular hot spot blocks were cast. In the second set of experiments, a tree of spherical hot spot castings, an inverted V-shaped castings and two blind riser castings were poured with the riser feeding a cylinder at its mid-height in one case and at its base in the other.

Thermocouple data was recorded for each set of experiments. Inverse modeling was performed for each set of temperature data to determine the temperature-dependent thermophysical property data giving the best agreement between the temperature measurements and predictions. This temperature-dependent thermophysical property data is presented here in detail.

The observed porosity distributions in the experiments were compared to modeling predictions using a currently available commercial porosity model and the novel advanced porosity model. The recommended set of adjustable parameters in the advanced porosity model were determined that achieves the best agreement between observed and predicted porosity locations and distributions. This set of parameters is presented. The comparisons between observed and predicted porosity distributions using the advanced model agree well.

During the course of this work, it was found that there were short comings in predicting the solid shells that formed at the top surface of the castings and some of the observed surface sinks. It is not currently possible to compute natural convection during solidification using the advanced porosity model. In the future, computing natural convection during solidification and porosity formation in the advanced model should improve the prediction of surface sinks and the observed freezing over of the risers in the experiments. Also in future work, a more quantitative analysis of the porosity distributions from the experiments and predictions could and should be performed. Image analysis of the sections from the porosity experiments and from the simulation results would further support the accuracy of the predictions in the advanced porosity model. More experiments using blind risers are also recommended given that the model can predict their feeding behavior.

Acknowledgements

References

[1] Hardin, R.A., and Beckermann, C., "Effect of Porosity on the Stiffness of Cast Steel," Metall. Mater. Trans. A, Vol. 38A, 2007, pp. 2992-3006.

[2] Hardin, R.A., and Beckermann, C., "Prediction of the Fatigue Life of Cast Steel Containing Shrinkage Porosity," Metall. Mater. Trans. A, Vol. 40A, 2009, pp. 581-597.

[3] Khalajzadeh, V., and Beckermann, C., "Advanced Modeling of Shrinkage Porosity and Application to Mn-Steel Castings," in Proceedings of the 72nd SFSA Technical and Operating Conference, Paper No. 5.7, Steel Founders' Society of America, Chicago, IL, 2018.

[4] Khalajzadeh, V., and Beckermann, C., "Simulation of Shrinkage Porosity Formation During Alloy Solidification," Metall. Mater. Trans. A, Vol. 51A, 2020, pp. 2239-2254.

[5] C. Pequet, M. Gremaud, and M. Rappaz, Metall. Mater. Trans., 2002, vol. 33A, pp. 2095–2106.

[6] H. Samet, and M. Tamminen, IEEE Transactions on Pattern Analysis and Machine Intelligence, 1988, vol. 10(4), pp. 579-586.

[7] *MAGMAsoft*, MAGMA Gmbh, Kackerstrasse 11, 52072 Aachen, Germany.